Tracking Subduction Tremor in Cascadia Using Regional Network and Small-Aperture Seismic Array Data

Wendy A. McCausland

A dissertation
submitted in partial fulfillment of the
requirements for the degree of

Doctor of Philosophy

University of Washington

2006

Program Authorized to Offer Degree:
Department of Earth and Space Sciences

University of Washington
Graduate School

This is to certify that I have examined this copy of a doctoral dissertation by

Wendy A. McCausland

and have found that it is complete and satisfactory in all respects,
and that any and all revisions required by the final
examining committee have been made.

Chairs of the Supervisory Committee:

_____
Stephen Malone

_____
Christopher Newhall

Reading Committee:

_____
Stephen Malone

_____
Christopher Newhall

_____
Kenneth Creager

Date: _____

University of Washington

Abstract

Tracking Subduction Tremor in Cascadia Using Regional Network and Small-Aperture Seismic Array Data

Wendy A. McCausland

Chairs of the Supervisory Committee:
Professor Steve Malone
Department of Earth and Space Sciences
Professor Chris Newhall
Department of Earth and Space Sciences

Non-volcanic tremor has been recorded at many subduction zones, including the Nankai, Cascadia, and Alaskan subduction zones. Their coincidence with cyclic GPS-measured slow slip events was first noted in Cascadia and subsequently in Japan. Regional network data were used to characterize five areas of tremor along the U.S. section of the Cascadia subduction zone from January 2002 through June 2005. Tremor episodes occur during periods with and without measurable geodetic slip, the amplitude of the reduced displacement This dissertation uses regional network and small aperture seismic array analysis to track non-volcanic tremor in the Cascadia subduction zone with and without slip is comparable, tremor covers a wide range that does not coincide directly with the subducting slab, the tremor can migrate bi-directionally from the point of initiation, and more than one distinct tremor source can be active at a given time.

The July 2004 Episodic Tremor and Slip (ETS) episode was recorded on three geographically distributed seismic arrays. This experiment was the first to use array analyses techniques to study subduction tremor. Individual wave phases were tracked across the stations of the arrays, and the tremor was active during almost all (99%) minutes of the analyzed tremor episode for the

five-minute sample windows. Locations were determined by comparing slowness vectors calculated at the arrays to slownesses computed given a 1D velocity model, and are stable within a volume roughly 250 km^2 in epicenter and 20 km in depth for hours to days before moving to a new volume. The transition between volumes is not smooth, and the movement of the sources within the volume follows no specific pattern. Errors in the computed back-azimuth and slowness are at best 8 degrees and 0.033 s/km, respectively, for S-waves. Uncertainties in the locations are at best 5 km in epicenter and 10 km in depth.

I suggest that the tremor is related to the presence of fluids at depth, potentially causing fracturing in the surrounding rock, reducing normal stresses along pre-existing faults and causing low stress-drop earthquakes, or migrating through fracture systems.

TABLE OF CONTENTS

LIST OF FIGURES

LIST OF TABLES

ACKNOWLEDGEMENTS

I would to thank Christopher Newhall, Stephen Malone, Kenneth Creager, Robert Crosson, and Garry Rogers for their guidance, helpful discussions and thoughtful questions as members of my Ph.D. and dissertation reading committees. I would also like to thank the Pacific Northwest Seismograph Network staff, Tony Qamar and the rest of the staff of the U.S. Geologic Survey Seattle office for all their immeasurable support with field work and data acquisition. Finally I would like to thank my family and friends for all the great advice and support given to me throughout this process. I could not have finished without them.

DEDICATION

In Memory of

Margaret Jane Tripodi

and

Anthony Qamar

INTRODUCTION

Where and how the stresses created by subduction are released is important to the assessment of seismic hazards. It is well documented that the rate of convergence can be measured using long-term GPS measurements (Dragert et al., 2001; Miller et al., 2002). A new and interesting area of research is the study of periodic, local reversals to the steady convergent plate motion (Dragert et al., 2001; Miller et al., 2002). This newly discovered type of event, called slow slip events, is recorded on regional global positioning system (GPS) networks rather than seismic networks. In the northern Cascadia subduction zone, these slow slip events have occurred at a regular interval of 14 $\pm$ 2 months since at least 1992 (Miller et al, 2002).

Another newly discovered phenomenon occurring at warm, young subduction zones is deep non-volcanic tremor. Such tremor has now been observed in many different subduction zones including the Nankai (Obara, 2001), the Cascadia (Rogers and Dragert, 2002; Szeliga et al., 2005; McCausland et al., 2005), and the Alaskan (Peterson et al., 2005). Non-volcanic tremor has also been observed along the San Andreas Fault (Nadeau and Dolenc, 2005). What is unique about the tremor signals is that until their discovery in Japan in 1999 (Obara, 2001), tremor had only been identified in volcanic areas.

The tremor occurs both with (the largest and longest episodes) and without (shorter episodes) a detectable slow slip event (Figure 2) (Rogers and Dragert, 2002; Hirose and Obara, 2003; McCausland et al., 2005). Recent studies have shown that the hypocentral locations of the tremor do not directly coincide with the subducting plate interface, but rather have a wide depth distribution (12-60km) (Kao et al., 2005; McCausland et al., 2005; Kao et al., 2006). While the signals are dominated by SH wave phases, there is evidence of weak P-wave phases when the data are analyzed on small aperture seismic arrays (La Rocca, et al., 2005). In Japan low frequency earthquakes occur concurrently with tremor and locate along and just above the subducting slab

interface (Shelley et al., 2006). With all this information about the characteristics and occurrence of deep non-volcanic tremor, we still do not know what the source of these signals is. Knowing how the seismic energy is being produced can begin to help us understand if the tremor and slow slip events are increasing the potential for great earthquakes in the locked portion of the subduction zone.

Tremor signals are emergent, occur as bursts that last for minutes to hours (Figure 3), have a limited frequency content (1 – 6 Hz) (Figure 4), have largest amplitudes on horizontal components, and have apparent velocities of the tremor is around 4 km/s. Waveforms cannot be easily directly correlated between stations separated by more than a few kilometers. These characteristics make it difficult to use traditional network data and processing techniques to locate the source of the signals. Locations determined from the band-pass filtered rectified signals on network stations have epicentral errors on the order of kilometers and depth errors on the order of 10 kilometers (McCausland et al., 2005). Traditional network data are also not adequate to understand how deep non-volcanic tremor changes and progresses on timescales of seconds to minutes.

Previous studies have used regional seismic networks to locate and detect non-volcanic tremor (Obara, 2001; Kao et al., 2004; Kao et al., 2005; McCausland et al., 2005; Kao et al., 2006). Locations of the tremor have been determined using the following two methods: 1) using relative arrival times at network stations obtained from amplitude variations which can be tracked between network stations (by the cross-correlation of band-pass filtered, rectified signals (herein called envelopes)) (Obara, 2001; McCausland et al., 2005), and 2) using the source scanning algorithm (Kao et al., 2004; Kao et al., 2005; Kao et al., 2006). The tremor signals lack phases that can be tracked from regional station to regional station, making the depth of the events difficult to determine precisely on regional-scale networks using the cross-correlation of the envelopes. The source scanning method (SSA) (Kao

et al., 2004) searches all space for bright spots of energy (sources); however this method is computationally intense and also depends on amplitude variations in the signals that are common to many stations. Another approach to studying tremor location is to take advantage of array processing techniques whereby the tremor waveforms can be correlated on stations that are sufficiently close to each other, and array processing techniques can be used to determine the apparent slowness (speed), back-azimuth (direction) and polarization of the tremor wave-fronts.

Array methods have been used extensively in volcanic settings to determine wave-field properties, locations and source properties of volcanic tremor (e.g. Konstantinou and Schlindwein, 2002; Chouet, 2003; Julian, La Rocca). Because volcanic and non-volcanic tremor have similar characteristics, this study capitalizes on some of the methods developed for volcanic tremor. In particular this study uses the properties of the wave-field in the time domain (e.g. Frankel et al., 1991; De Pezzo et al., 1997; La Rocca et al, 2005), rather than frequency-wavenumber techniques (Capon, 1969; Goldstein and Archuleta, 1991, 1997) because of the potential for changes in non-volcanic tremor location over short time windows.

To improve locations and to understand the temporal and spatial progression of the tremor sources as the tremor episode progresses, we installed three temporary, dense seismic arrays in 2004 (La Rocca et al., 2005). Installation was timed to catch the next anticipated tremor and slip event in the northern section of the Cascadia subduction zone, which occurred in July 2004. We chose the spacing between the stations within the array in order to track individual phases across the array. We chose the locations of the arrays to surround the region where the previous tremor sequences have initiated. Using data from the three arrays, I determined the apparent slowness and back-azimuth of the tremor in five-minute and thirty-second windows throughout the sequence of tremor. I used the slowness vector from the three arrays to locate the tremor bursts given both a 1D (modified PNSN P3 model)

and a 3D (Crosson, 2004) S-wave velocity model. Combining this with polarization analysis (Jurkevics, 1988; La Rocca et al, 2005) we can better constrain how the locations of the bursts and the types of waves comprising the tremor signal change over the course of the tremor episode.

Chapter 1 presents previously published results (McCausland et al., 2005) regarding the characteristics of non-volcanic tremor using the Pacific Northwest Seismograph Network (PNSN). Chapters 2 through 4 present the results from the small aperture seismic array experiment in 2004. Chapter 2 describes the array configurations and what data were collected. Chapter 3 describes the analyses methods used. Chapter 4 describes the results of the array analyses. Possible explanations of source mechanism are in Chapter 5 given the results from the network and array data. Finally I will close with a discussion of remaining ambiguities/uncertainties and some suggestions on how these might be addressed.

Using the results of this study, I am able to propose a couple source models for the tremor that are consistent with the majority of observations of the tremor and their association with slow slip events. I also discuss several other source models that contradict some observations, but these contradictions are not entirely fatal. I do believe that the tremor and slip must be related to the presence of fluids at depth and whether the presence of fluids cause the tremor and slow slip or just facilitate their occurrence under the correct stress conditions is not yet clear. This experiment was the first to use small aperture arrays to track the tremor in consecutive time windows and provides results that help us begin to understand how tremor relates to the processes of subduction and therefore the regional seismic hazards.

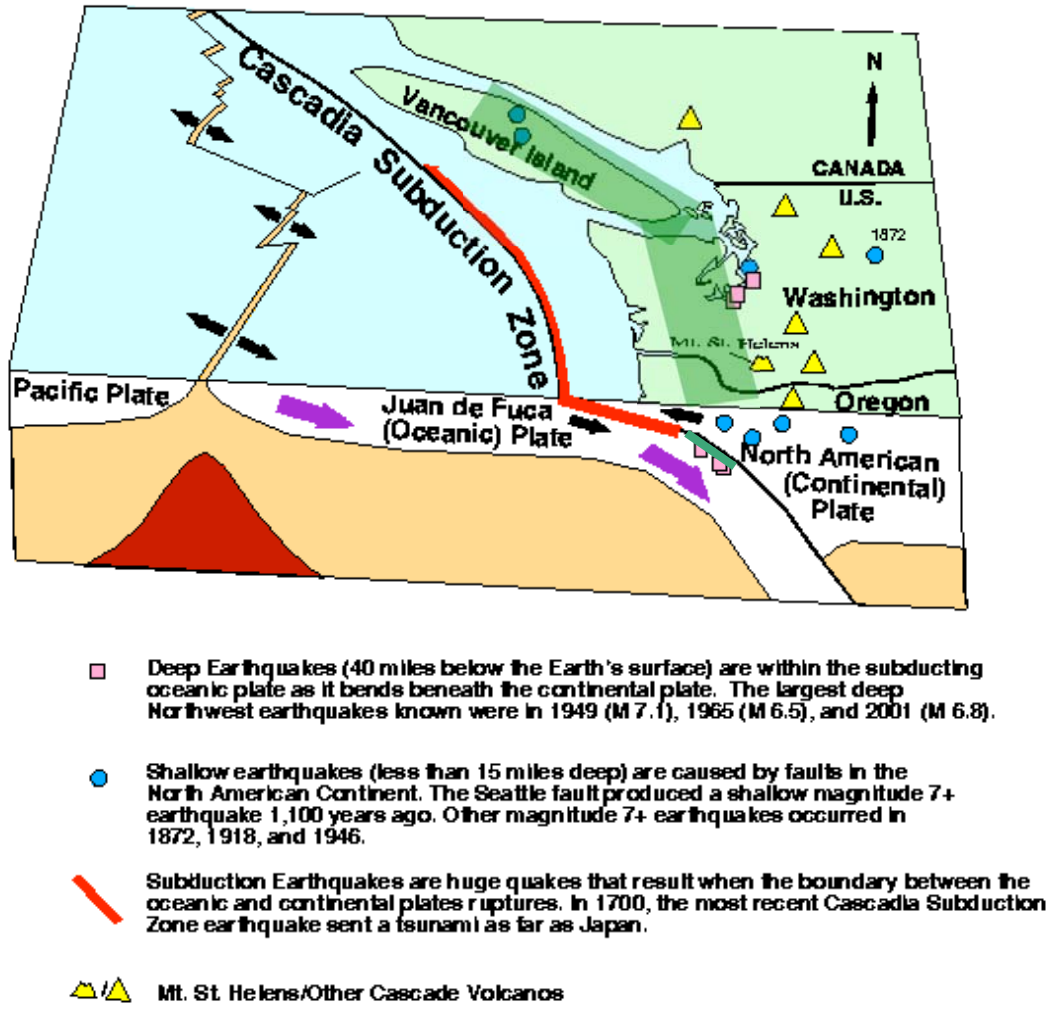

Figure 1 Tectonic Setting. Cartoon figure depicting the Cascadia subduction zone, where the Juan de Fuca plate is subducting beneath the North American plate. Volcanoes are indicated with yellow triangles, crustal earthquakes are indicated with blue circles, deep subduction plate earthquakes are indicated with pink squares, the region that generates great subduction zone earthquakes is highlighted in red, and the region where slow earthquakes are modeled to occur is highlighted in green. Epicentral locations of tremor lie within the green rectangles. (figure modified from http://www.pnsn.org)

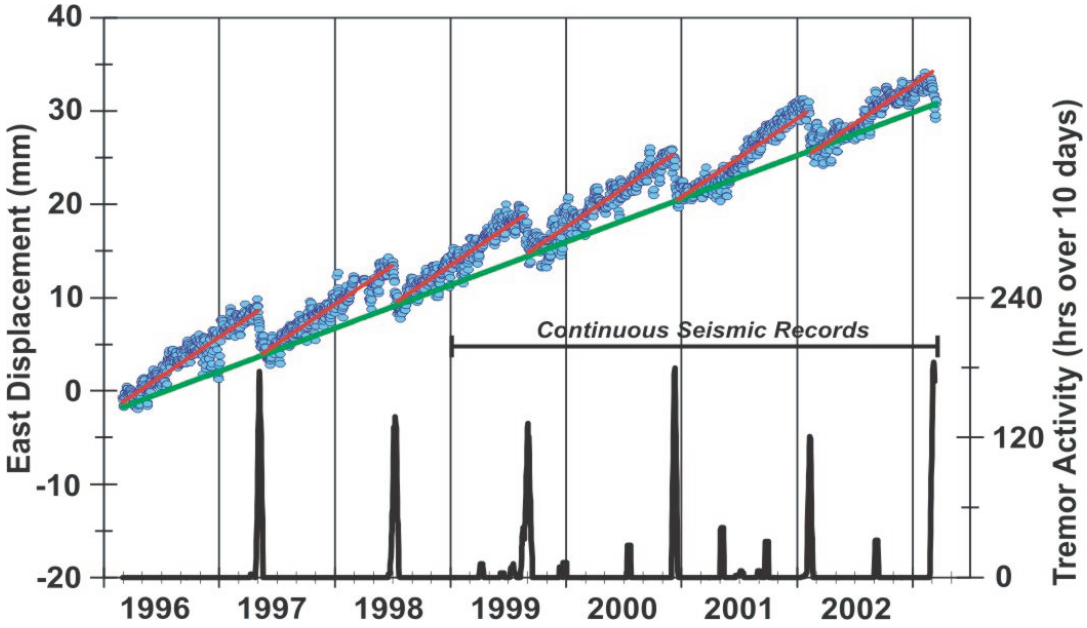

Figure 2 Tremor and Slow Slip Activity (figure from Rogers and Dragert, 2002). Figure showing the coincidence and recurrence of major tremor and slip episodes from Vancouver Island, BC. Daily changes (referenced to North America) in east component of GPS station ALBH (Victoria) data is indicated by the blue circles, linear trends are indicated by the red (mean convergence between slip events) and green lines (long-term inter-seismic convergence rate). Black lines show hours of tremor activity in successive 10 day windows.

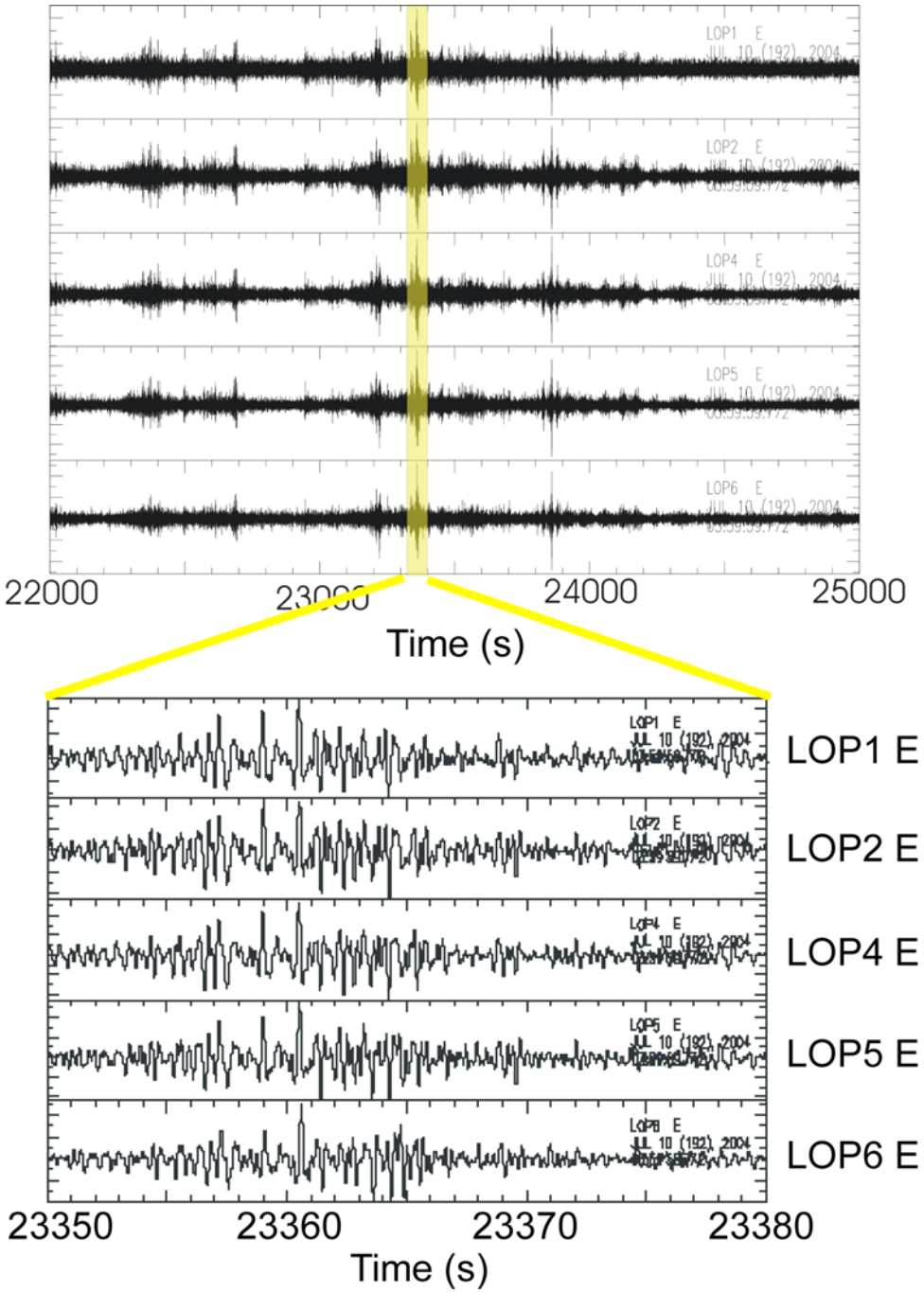

Figure 3 Example of Tremor Signal. Tremor Signal at Lopez Array July 10, 2004. East component of seismograms recorded at Lopez Array. Upper figure shows 50 minutes of data. Tremor occurs in bursts over many time scales. Lower figure is a blow up of the highlighted region in the upper figure (30 s). Emergent onsets and high level of correlation are evident from the lower figure.

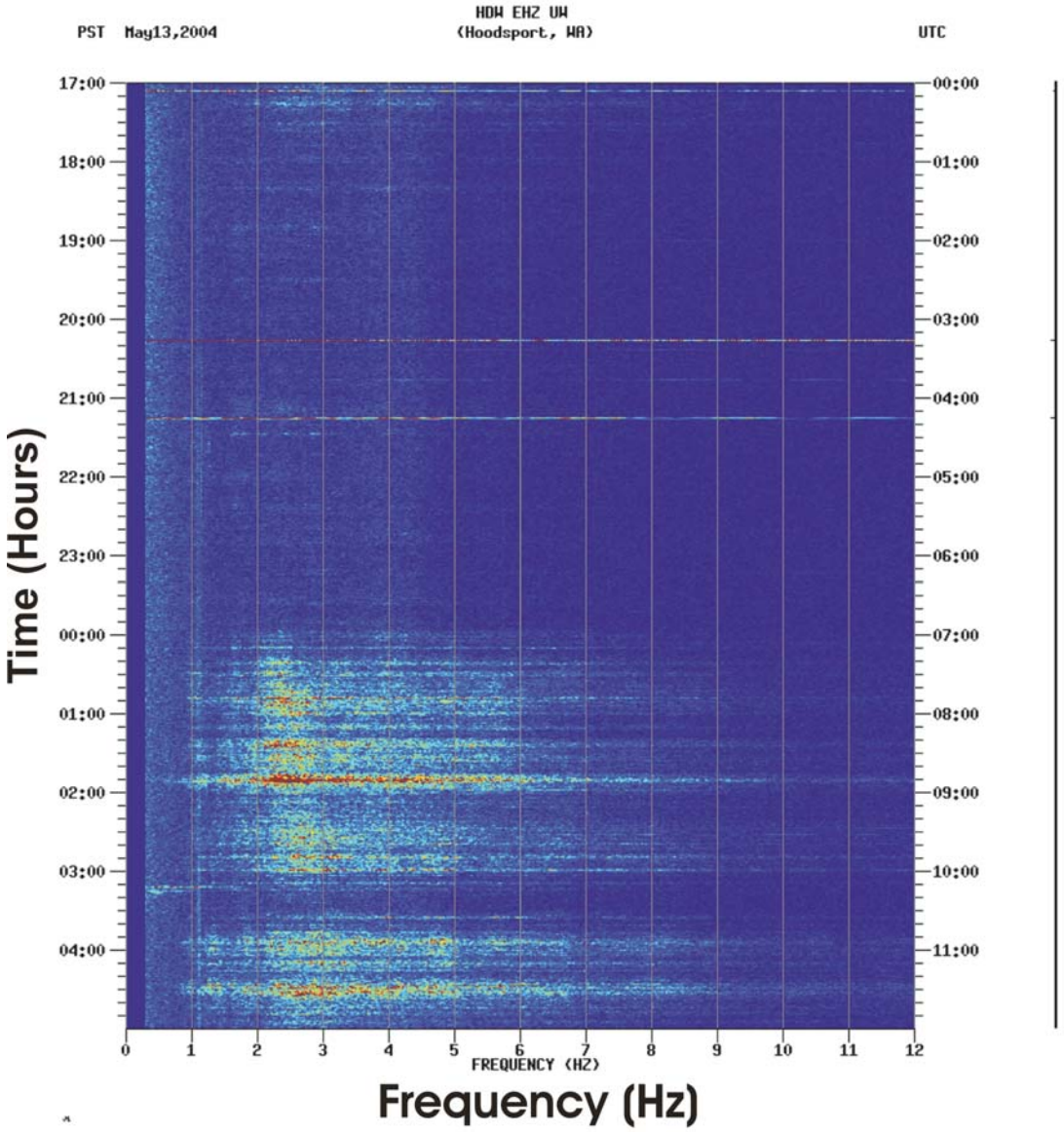

Figure 4 Tremor Spectrogram. Spectrogram of twelve hours of tremor on May 13, 2004. Signal was recorded on the PNSN station HDW, which is a vertical component only 2-Hz seismometer. The horizontal axis is frequency in hertz. Time is marked in Pacific Daylight Time on the left vertical axis and in Greenwich Mean Time on the right vertical axis. Strength of each frequency is indicated by color where blue is low and red is high.

CHAPTER 1:
Temporal and Spatial Occurrence of Deep Non-Volcanic Tremor: From Washington to Northern California

1.1 Introduction

A yet unanswered question regarding deep non-volcanic tremor is what is the relationship between the tremor and geodetically measured slow slip events. To date deep non-volcanic tremor has been reported in southwest Japan (Obara, 2002), along the Cascadia subduction zone (Rogers and Dragert, 2003; McCausland and Malone, 2004; Szeliga et al., 2004), the San Andreas Fault (Nadeau and Dolenc, 2005), and the Alaskan subduction zone (Peterson et al., 2005). Their coincidence with cyclic GPS-measured slow slip events (Miller et al., 2002) was first noted in Cascadia (Rogers and Dragert, 2003) and subsequently in Japan (Obara and Hirose, 2003). The hypocentral locations of the tremor do not directly coincide with the subducting plate interface, but rather have a wide depth distribution (McCausland and Malone, 2004; Kao et al., 2006). This paper uses regional seismic and geodetic network data to document the temporal and spatial occurrence of tremor in five distinct areas along the U.S. section of the Cascadia subduction zone, the occurrence of tremor both with and without geodetic slow slip events, and quantifies the size of the tremor signals. In this paper we use the term slow slip event to describe GPS-measured deformation transients that have been modeled as deep slow slip events.

1.2 Data and Methods

Data for this study came from the regional stations of the PNSN, PGC, and Northern California Seismic Network (NCSN) (Figure 5). The stations are three-component broadband or one-component short-period (1 Hz) instruments. Sampling rates for the different station types and networks are 40, 50 and 100Hz. The data for this study were collected continuously and analyzed in near-real time, starting in November 2002 for Washington and

northern Oregon, and in May 2004 for northern California. All data sets extend through June 2005.

The deep tremor signals rise gradually from the background noise, with maximum amplitudes two to four times the background noise. To identify tremor bursts, vertical component data for 10 high quality and geographically distributed stations (Figure 5) are band-pass filtered (1 – 6 Hz), rectified, down-sampled and smoothed. These 'envelopes' are plotted together hour by hour in a roughly north-to-south order for review (Figure 6). A full suite of regional station waveforms is saved when a tremor burst is identified.

There are no obvious P, S or other seismic phases in the tremor signal., so tremor locations are determined by calculating 'envelopes' for all saved seismograms and picking the relative arrival times of a particular burst. Cross-correlation is used to eliminate envelopes that are not well correlated (>0.85), and to refine the picks (Figure 6). Hypocenters are determined in a one-dimensional regional S-wave velocity model using the relative arrival times (mean uncertainties: 1-2 s). Because network inter-station distances are large (~50 km) and more than one tremor source can be active at a given time, the depths of the bursts are not as well constrained as the epicenters. Errors due to pick uncertainty (2 s) and the location process as well as determined through jack-knife tests typically translate to 5 km in epicenter and 10 km in depth.

We calculate the displacement amplitude of the tremor at the source location for well-located bursts using the formula for reduced displacement, R_d, for body-waves defined by Aki and Koyanagi, (1981). The R_d for each burst is the average over picked stations. We calculated the average and standard deviation of the well-located bursts for each episode and eliminated stations with values consistently greater than two standard deviations from the mean.

1.3 Results

Observed tremor signal characteristics are the same as in previously published work (e.g. Obara, 2002; Rogers and Dragert, 2003; Kao et al., 2005). Signals are strongest on the horizontal components, and travel across PNSN stations with an apparent velocity (3.8 – 4.2 km/s) consistent with deep shear waves. Maximum tremor amplitudes are 2 to 4 times the background noise on medium quiet stations. R_d's for well-located bursts range from 0.06 to 0.59 cm^2. The average values over notable episodes with and without geodetic deformation are listed in Table 1. Note the size of the average is independent of the occurrence of an inferred slow slip event.

Tremor epicenters lie between the surface projections of the 20 to 40 km depth contours of the subducting slab (Preston and Creager, 2004). Tremor depths are distributed over a wide range, between 12 and 60 km, a range greater than the errors on the depths (10-20 km). Depths of events do not increase eastward as one might expect if they were occurring at or in relationship to the subducting slab interface. This result confirms work recently published on the Canadian section of the Cascadia subduction zone (Kao et al., 2006).

More than one source can be active at a given time. We see this in plots sorted with respect to distance from one epicenter (Figure 6). Note the move-outs of the various tremor bursts are not all parallel. Peaks of the bursts run together at some stations, making locations difficult. The epicenters sometimes migrate trench parallel over periods of days. For two areas, the tremors at first migrate bi-directionally from the point of initiation. On shorter time scales, epicenters are more random over a region as large as 100 km on a side.

Tremor bursts have been observed along most of the Cascadia subduction zone, excluding central Oregon where network station coverage and quality makes detection difficult. We have observed five relatively independent areas of tremor along the U.S. section of the Cascadia

subduction zone (Figure 5, Table 1). Area 1 is from the central Puget Sound north and is the main 14-month repeating ETS area described by Rogers and Dragert (2003). Area 2 is the Puget Sound region and it overlaps with areas 1 and 3 but is limited in extent and has tremor episodes independent of GPS detected deformation. Area 3 extends from central Puget Sound to Northern Oregon and was quite active during an ETS in Apr.-May, 2004 with some activity during the main ETS episode of Feb.-Mar. 2003. Area 4 is in southern Oregon and area 5 is in northern California. Between Jan. 2003 and Jun. 2005, the observed total hours of tremor were 373.8 in area 1, 164.6 in the area 2, and 297.6 in area 3. Between May 2004 and Jun. 2005, there were 179.8 hours of observed tremor in northern California (area 5) (Figure 6).

In northern Washington and beneath Vancouver Island, the largest and longest episodes of tremor coincide with the 14-month cyclic GPS-measured slow slip events (Figure 7) (Rogers and Dragert, 2003; McCausland and Malone, 2004). The 2003 event lasted from Feb. 23 through Mar. 20 and was associated with up to 6mm of GPS measured slip (Melbourne et al., 2005). This episode involved tremor and slip from southern Vancouver Island to southern Washington (areas 1 and 3). The next 14-month cyclic episode that occurred from Jul. 8 - 24, 2004 only involved area 1. For both of these ETS events, the tremor initiated in the Strait of Juan de Fuca and migrated northwestward along Vancouver Island (area 1) with some events migrating southward, including area 3 for the Mar. 2003 event. The average R_d's for well-recorded tremor bursts during these ETS events were 0.38 and 0.40 cm^2, respectively (Table 1).

Area 3 extends from the central Puget Sound to Northern Oregon. Strong tremor and slow slip occurred in this region from Apr. 23 to May 25, 2004. The events initiated near 46.6 N and 122.8 W and subsequently migrated to the north and south. This tremor was associated with 5 mm of GPS movement, and the average R_d was 0.42 cm^2. This ETS event was clearly different and independent from the 14-month ETS events of northern

Washington-southern Vancouver Island. Another episode of tremor occurred in this region from Apr. 10 – 26, 2005, but no GPS deformation is reported for this time yet. Strong tremor has occurred in this area three times, thus there may be a repeating sequence in area 3 of about 12.5 months.

Between areas 1 and 3, there have been periods of tremor with no GPS-measurable deformation. Tremor bursts during these non-slip episodes outline area 2 (Figure 5). Both the depth range of and R_d's of tremor in area 2 are comparable to tremor accompanied by a slow slip event (Table 1). The tremor in area 2 lasts only hours to days with the largest and longest episode lasting for 11 days (Figure 7). These slip-less episodes account for 23% (162.4 hours) of the total number of hours of observed tremor in this region between Jan. 2003 and Jun. 2005 (Figure 7). Epicenters during these episodes do not show any discernable migration.

Data for Oregon (area 4) have only been examined in detail since April 1, 2005. The first episode of tremor was detected between May 30 and Jun. 3, 2005 with 21.5 total hours of tremor (Figure 7). The average R_d for located bursts during this episode is 0.16 ± 0.05 cm^2. No slip has been reported for this time period.

Data for northern California (area 5) have been examined since May 23, 2004, when Seth Moran (pers. commun., 2004) reported seeing tremor in the 2 – 6 Hz band. This episode lasted from May 23 to Jun. 10, 2004, contained 79.5 hours of tremor, and the average R_d was 0.45 ± 0.07 cm^2. The Northern California Geodetic Array (J. Murray, pers. Commun., 2004) has reported no GPS slip during this time. Seismic and geodetic observations in this region by Szeliga et al. (2004) from 1998 through the early 2004 indicate periodic ETS events at intervals of 10.9 ± 1.2 months. These observations may be the same as our area 4 or area 5. Since June 2004, there have been a total of 176.0 hours of tremor observed in this region (Figure 7). The longest episode lasted 19 days.

1.4 Discussion

The association of geodetic slow slip events with major tremor episodes is undeniable. However there is significant tremor activity during periods with no discernable GPS deformation. These episodes fall outside the 14 $\pm$ 2 month cyclic ETS periods and last from hours to almost two weeks. Similar observations of tremor with no deformation have been made in the Nankai subduction zone where the geodetic signal is measured by borehole tiltmeters (Obara and Hirose, 2003). Average R_d's for tremor with and without a slow slip event are similar indicating that the size of the seismic signal is independent of whether a slip event occurs (Table 1). On the time scale of days, the tremor epicenters migrate along with the slip front, but on shorter times scales (minutes to hours), the source locations are more chaotic (Figure 6). In the first days of the episode, tremor in area 1 and 3 migrate bi-directionally from the point of initiation. It is possible there is geodetic slip during the shorter tremor episodes but is below the current resolution of GPS data.

A convenient model to explain both tremor and slip is that tremor is a series of small earthquakes along the subduction interface in the transition zone (between stick slip and stable sliding behavior), whose signals interfere in such a way as to produce the relatively continuous tremor signals (Rogers and Dragert, 2003). In this case the tremor should have locations along the interface and frequency content similar to tectonic earthquakes. Tremor locations and their limited frequency content are inconsistent with this model. We also might expect both P- and S-wave phases in the signals, particularly on the vertical component seismograms. While the widely spaced network stations do not allow the unambiguous resolution of individual wave types, there are no cases where the move-out of energy bursts travel with P-wave velocities. All of these observations suggest that while geodetic slip and seismic tremor can occur simultaneously, they are not different manifestations of the same source process on different time scales.

Another model for tremor is that it results from the presence or movement at depth of fluids generated by the dehydration of the subducting

slab (Peacock, 1993). The presence of fluids could generate seismic signals in several different ways. A temporary increase in pore pressure (reduction in effective normal stresses) could allow for strain energy release at low shear stresses. This energy release could be a series of small low stress-drop earthquakes distributed over a volume rather than along a fault. Or anomalous earthquake-producing stresses could be generated in a volume by rock expansion. The addition of fluids to the mantle wedge results in the formation of serpentine, a transition accompanied by a significant volume increase (20 to 40%) (Hacker et al., 2003; Fryer and Mottl, 1997). These models for tremor generation might explain the distributed hypocenters of tremor bursts, but they still would have earthquake-like spectra.

We require a model that produces tremor sources above the subducting slab, and temporal association with slow slip events, but not always. The character of the tremor (frequency content, emergent, long-lasting, small amplitude) is similar to volcanic tremor generated by the movement of fluids (Julian, 1994; Chouet, 1996). Fluids from the dehydration of the subducting slab migrate buoyantly through the mantle wedge and lower crust (Peacock, 1993). Minor stress changes above the slab due to slow slip events could accelerate fluid movement, producing more and longer tremor during slip episodes than in the interim. This type of source process would account for the limited frequency content, emergent nature, and small size of the tremor signals.

Another model related to fluids, but not invoking fluids as the seismic source involves serpentinization of the mantle wedge in Cascadia and other warm subduction zones (Brocher et al., 2003). Localized, inhomogeneous volume changes resulting from the transition of mantle peridotite to serpentine (Fryer and Mottl, 1997) could cause stress concentrations leading to micro-fracturing throughout a volume. Again, slow slip events could modulate the stresses in this volume to trigger tremor sequences. This source requires the presence of water and can account for the variable

depth ranges and epicentral locations of the tremor, as well as occasionally concurrent slow slip events.

1.5 Conclusions

Observations of non-volcanic deep tremor in Cascadia using regional seismic networks provide some constraints on possible sources. Key observations are: it sometimes but not always occurs with slow slip events; it occurs in many places in Cascadia, but not simultaneously everywhere; each tremor area may repeat with a cyclic period of at least several months; it occurs over a large range of depths, not just near the subducting slab interface; more than one spatially isolated burst of tremor can be active at the same time; and it has a limited, low-frequency range and emergent low-level signal character.

Given these observations, we think the tremor and slow slip events are only indirectly related. Tremor is likely related to fluid migration from the slab interface into the mantle wedge. Fluid pressures may be modulated by slow slip on the interface producing the strong, long-lasting episodes, but such slip is not necessary to produce some periods of tremor. The tremor may be generated directly by fluid flow, as in volcanic tremor or be related to micro-fracturing around stress inhomogeneities generated by expansion due to the serpentinization of the mantle by migrating fluids. Differentiating these two source models will require a combination of better seismic data and specific source modeling of these two processes.

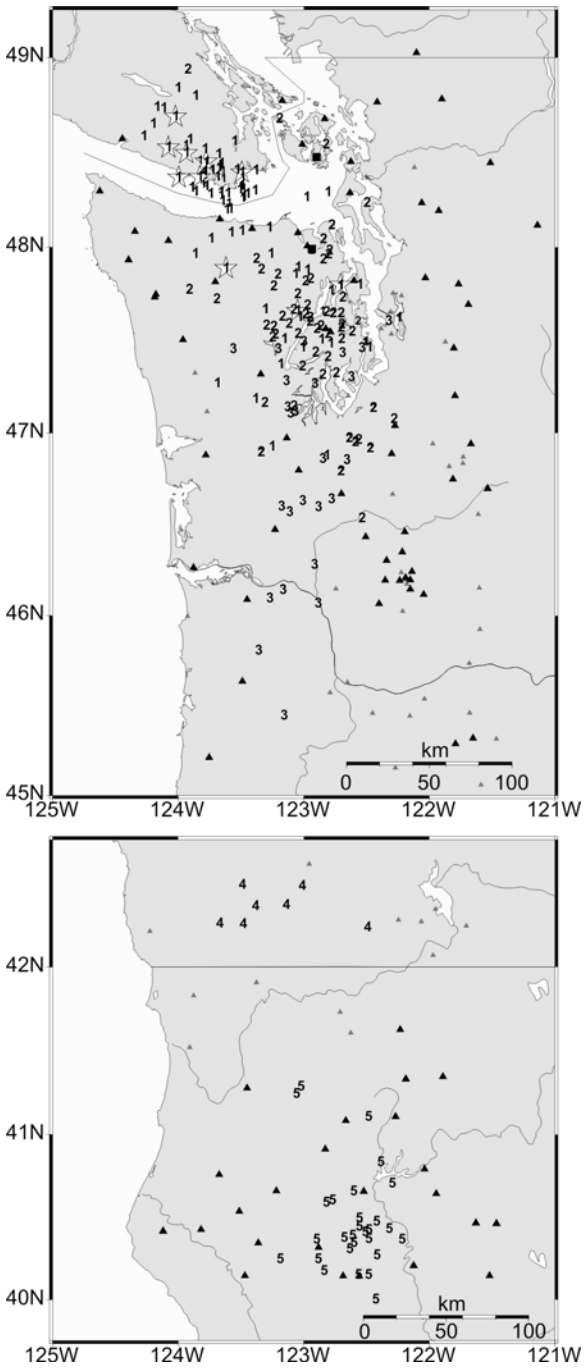

Figure 5: Tremor Epicentral Locations. Epicentral locations determined from network stations indicated by the number of the area in which they occurred: area 1-southern Vancouver Island to central Puget Sound; area 2 –Puget Sound region; area 3 – southern Puget Sound to northern Oregon; area 4 – southern Oregon; area 5 – northern California. White stars indicate the locations of bursts marked in Figure 6. Black triangles indicate stations used to obtain burst locations, grey triangles indicate the remaining network stations.

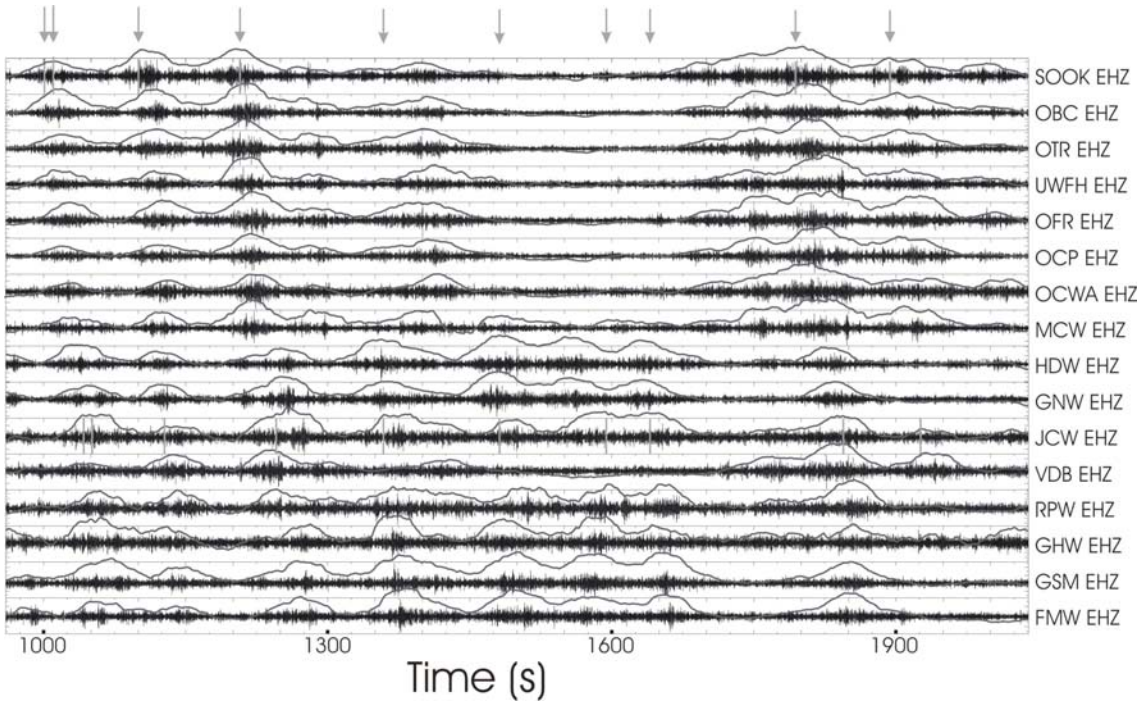

Figure 6 Filtered Tremor Signals. Band-passed (2-6Hz) seismograms and envelopes of vertical component PNSN data for 18 minutes on July 15, 2004. Gray arrows indicate pick times for 10 tremor bursts on stations SOOK (top) and JCW (bottom). White stars on Figure 5 indicate the corresponding epicentral locations. Stations are sorted by epicentral distance from the first location. At least two active source regions are evident, one to the north of the Strait of Juan de Fuca and the other to the south.

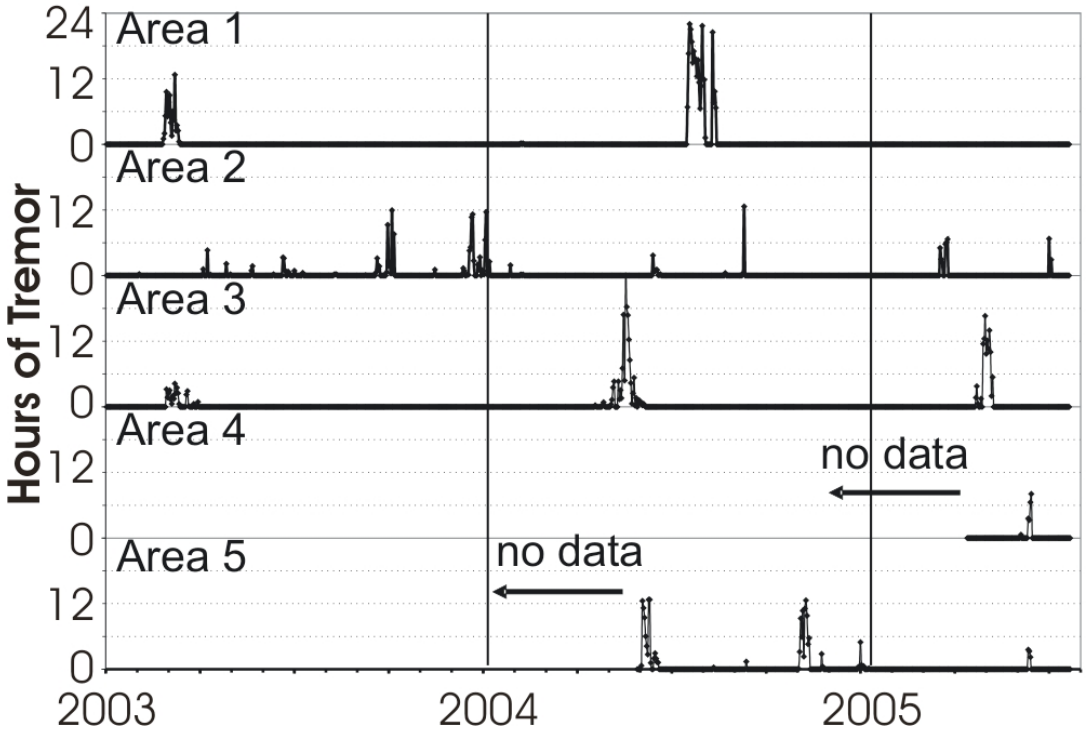

Figure 7 Daily Tremor Count. Graph showing the number of hours of tremor per day for the five areas. Washington data begins January 2003; California data, May 2004; and southern Oregon, April 2005.

Table 1 Tremor Episode Characteristics. Table summarizes the characteristics of major tremor episodes through June 2005**.**

Dates of Episode	Hours of Tremor	Area	Slow Slip	Migration	Mean Rd
2/23 – 3/20/03	111.8	1,3	6 mm	to NW & S	0.38 $\pm$ 0.10 cm^2
9/15 - 9/18/03	6.65	2	No	No	0.17 $\pm$ 0.07 cm^2
9/25 - 9/30/03	42.8	2	No	No	0.12 $\pm$ 0.03 cm^2
12/12 - 12/17/03	37.0	2	No	No	0.07 $\pm$ 0.03 cm^2
12/21/03 -1/1/04	29.5	2	No	No	0.38 $\pm$ 0.07 cm^2
4/23 – 5/25/04	164.6	3	5 mm	to N & S	0.42 $\pm$ 0.05 cm^2
5/23 – 6/10/04	79.5	5	No	No	0.45 $\pm$ 0.07 cm^2
7/8/04 – 7/24/04	251.5	1	Yes	to NW	0.40 $\pm$ 0.10 cm^2
4/10-4/26/05	111.9	2	Possible	No	0.43 $\pm$ 0.13 cm^2
5/30-6/03/05	21.5	4	No	No	0.16 $\pm$ 0.05 cm^2

CHAPTER 2:
Array Experiment Data

We deployed three geographically distributed seismic arrays in March and April 2004 to record the next anticipated tremor and slip event: one near Sequim, WA, one on Lopez Island, WA, and one near Sooke, BC (Figure 8). Array locations were chosen to surround the area where the previous repeating Cascadia tremor and slip events had initiated (Figure 8) (Rogers and Dragert, 2002; McCausland et al., 2005).

The configuration, extent and inter-station spacings of the arrays were based on several considerations. An ideal configuration has no more than two stations along a line, has a consistent geology and a stable site response across its extent, and the inter-station spacing samples at least ¼ of the wavelength that corresponds to the dominant frequencies of the tremor signals. This helps ensure that the seismic phases observed on each seismogram are representative of the same, minimally deformed wave-front. This high correlation between waveforms comes at the cost of the resolution of the computed slowness and back-azimuth. Simply put, a larger aperture results in better resolution of the computed slowness and back-azimuth, but a smaller aperture results in better coherence between the waveforms.

For this experiment, the planned aperture of the arrays and inter-station spacing of the stations were chosen based on the dominant frequencies (1.5 - 4 Hz) (Figure 4) and apparent velocities of the tremor (about 4 km/s) (Figure 9). For each array, the inter-station spacings were between 150 and 300 m with a total array aperture of approximately 600 m (Figure 8). Topography, location of rock outcrops, sky-view for GPS signal, and, in the case of Lopez, cable length all affected the resulting configuration of the three arrays.

The array near Sooke, BC consisted of 6 seismic stations. Four of the six stations consisted of a 2-Hz L22 seismometer, a Quanterra Q330 data logger, a Quanterra baler, and a GPS receiver (SOOK1, SOOK2, SOOK3, and

SOOK4). These four stations were stand-alone and were powered by two 12-V marine deep-cycle battery connected in parallel that were connected to solar panels for recharging. The data at these stations were recorded at 100 Hz and saved as day-long files. The remaining two stations (SOOK5 and SOOK6) consisted of a 2-Hz L22 seismometer, Q330, bailer and a GPS receiver. They were powered by a 12V battery with standard household AC power and a battery charger and transmitted the data by DSL connections provided by local land owners to the Pacific Geosciences Centre via the internet. The data for these two stations were also sampled at 100 Hz and saved locally as day-long files. The stations were installed on or within a few meters of rock outcrops.

The array near Sequim, WA consisted of 7 stations. A Lennartz LE-3Dlite seismometers (1-Hz), a Lennartz Marslite data logger and a GPS receiver comprised each station. The stations were stand-alone, powered by two 12V batteries, and the batteries were recharged by solar panels. The data were sampled at 125 Hz and saved as hour-long data files. These stations were buried in soil when rock outcrops were not available. Most stations were within a few meters of rock outcrops but for two sites (SEQ1 and SEQ5) no obvious outcrops were within a few 10s of meters.

Six stations comprised the Lopez Island array. The seismometers were the same as those used at the Sequim array, Lennartz LE-3Dlite seismometers (1-Hz). The data were recorded on Lennartz M24 data loggers, where two seismometers are connected to one data logger, one of which was connected by a 200m cable. A GPS receiver was connected to each data logger. Two of the Lopez data loggers (LOP1/ LOP2, and LOP3/ LOP4) were stand-alone, powered by 12V batteries, and recharged by solar panels. One data logger (LOP5/LOP6) was powered by a 12 V battery recharged by standard household AC current. One station pair (LOP3/LOP4) was transmitted by a Wy-lan radio transmitter to a receiver such that selections of the data could be accessed via the internet. All data were recorded at 125 Hz

and saved locally as hour-long files. The stations were installed on or within a few meters of rock outcrops.

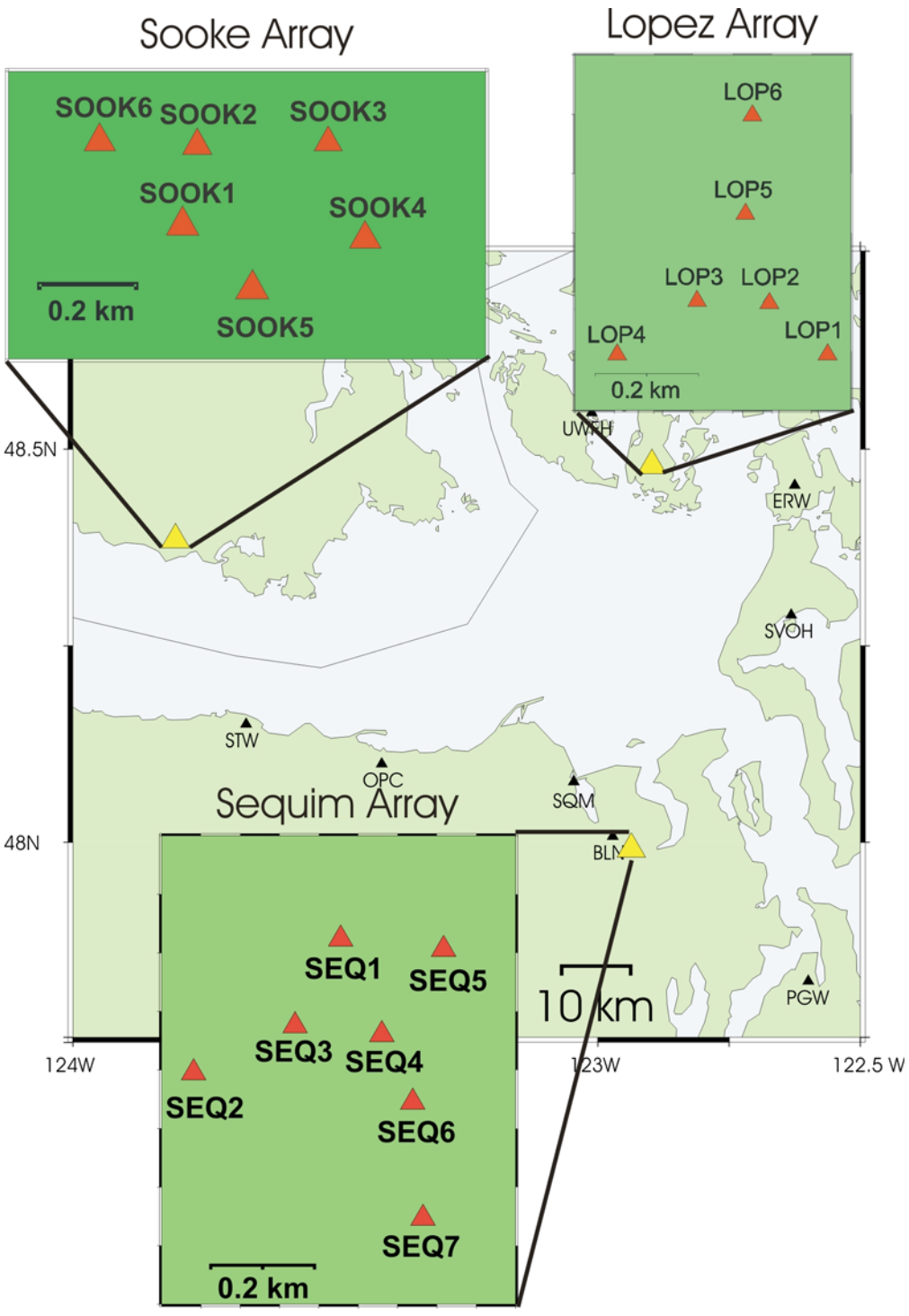

Figure 8 Array Locations and Configurations. Main map shows location of the centroid of each array with yellow triangles. Neighboring network stations are labeled and shown with black triangles. Insets show the configuration of each array using red triangles.

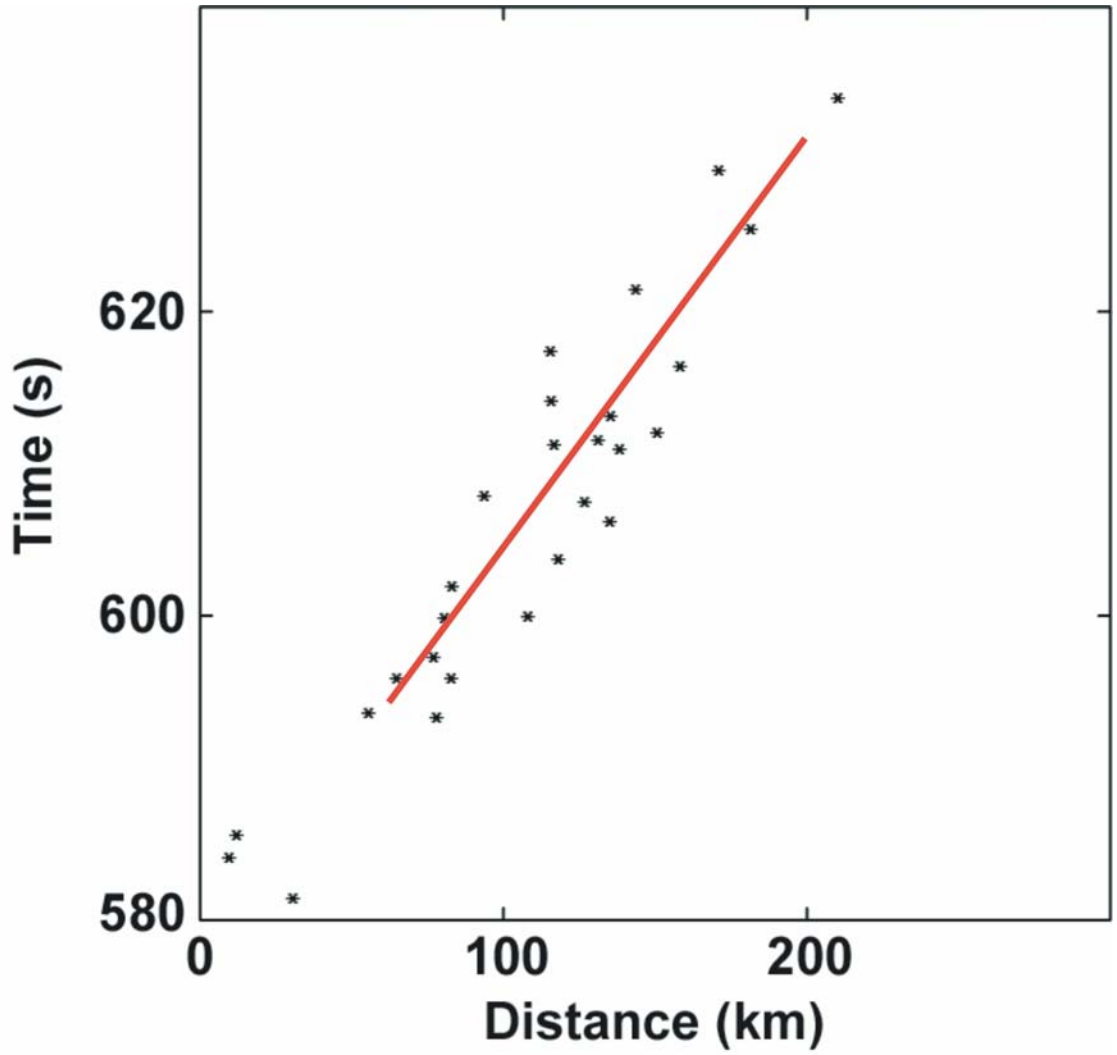

Figure 9. Travel Time Curve. Travel time curve for tremor burst picked on PNSN stations. Horizontal axis is epicentral distance in kilometers; vertical axis is relative arrival time in seconds. Stars are observed relative arrival times and distances at network stations. Line represents linear fit to data, with a slope of 3.8 km/s; this is the apparent velocity a tremor burst across the network.

Table 2 Array Station Locations. Table of station locations and relative locations with respect to the centroid of the array.

Station	Latitude (degrees)	Longitude (degrees)	Elevation (m asl)	Y-position (km)	X-position (km)	Relative elevation (m)
SEQ1	47.993267	122.937483	334	0.2138	-0.0300	- 11.7
SEQ2	47.990900	122.941200	372	-0.0495	-0.3077	26.3
SEQ3	47.991783	122.938567	350	0.0487	-0.1110	4.3
SEQ4	47.991550	122.936417	341	0.0228	0.0496	-4.7
SEQ5	47.993000	122.934967	331	0.1841	0.1579	-14.7
SEQ6	47.990483	122.935600	343	-0.0959	0.1106	-2.7
SEQ7	47.988433	122.935333	349	-0.3240	0.1306	3.3
SOOK1	48.3833	-123.8051	169	-0.0597	-0.1090	34.5
SOOK2	48.3847	-123.8047	148	0.1006	-0.0833	13.5
SOOK3	48.3847	-123.8012	149	0.1024	0.1799	14.5
SOOK4	48.3830	-123.8001	132	-0.0849	0.2589	-2.5
SOOK5	48.3824	-123.8032	112	-0.1609	0.0304	-22.5
SOOK6	48.3847	-123.8073	127	0.1024	-0.2772	-7.5
LOP1	48.478983	-122.89158	78	-0.1512	0.1755	5.7
LOP2	48.479867	-122.8931	85	-0.0528	0.0633	12.7
LOP3	48.479833	-122.89495	83	-0.0566	-0.0736	10.7
LOP4	48.478983	-122.89697	65	-0.1512	-0.2228	-7.3
LOP5	48.481367	-122.89368	63	0.1141	0.0201	-9.3
LOP6	48.483017	-122.89345	60	0.2977	0.0374	-12.3

CHAPTER 3:
Methodology and Procedures

3.1 Pre-processing of data

The data underwent some preprocessing before they were analyzed. The data were first converted to SAC (Seismic Analysis Code) format, then merged into day-long files. Next, we removed the mean and down-sampled the data to 25 samples per second.

In conjunction with the above pre-processing some further processing was required at the Sequim and Lopez arrays. Spikes in the frequency spectra of the data at Sequim and Lopez were noticed (Figure 10), and based on the frequencies of the spikes, they were determined to be due to electronic noise rather than from ground motion signals The noise spikes at each station were independent from those at other stations. These spikes were removed from the data using notch filters of width 0.003Hz. At Lopez the frequencies removed were between 0.6103 and 11.5966 at intervals of 1.2207 Hz. At Sequim, the frequencies removed were from 0.25 to 15 Hz at intervals of 0.25 Hz, and between 2.90625 and 11.625Hz at intervals of 2.90625 Hz. Because of the narrow width of the spikes and because of the broad frequency range (1 to 6 Hz) of the tremor, we do not believe that the removal of the spikes will affect the subsequent analyses of our data. The noise at Sequim likely resulted from electromagnetic interference of external signals with the electronics of the data loggers, and at Lopez they likely resulted from the 200 m long cables used to connect the seismometers to the data loggers picking up an external electronic signal.

For the Lopez and Sequim arrays I tapered the ends (0.1% of the file length: 86.4 s for a day long file) of the data files with a cosine taper. Finally, the instrument response was removed and because the dominant frequency band of the tremor is between 1 and 6 Hz, the data were band-pass filtered

between 1 - 6 Hz. Then the files were synchronized by cutting the data files so that they started and ended at the same time to within 0.01s.

For the Sooke array, no spikes were observed in the frequency spectra. However station SOOK2 had a reversed polarity on all components, therefore the data files for this station were reversed. It was noted that the phase response changed rapidly close to the corner frequency of the L22 instrument (2 Hz), and small errors in the phase response near the corner translate to significant timing errors. Thus the Sooke data were band-pass filtered over a smaller frequency band with its lower corner defined by a cosine from 2 - 4 Hz and its upper corner over 6 – 8 Hz. Errors in the calculated slowness at Sooke are typically twice the size of those calculated for Lopez and Sequim primarily because of the loss of low frequency information (Figure 11).

Then the Sooke files were synchronized by windowing the data files such that they started and ended at the same time. We tapered the ends of the data files with the same cosine taper as with the Sequim and Lopez data. The stations of this array were located on a significant slope and therefore had a systematic bias to their vertical locations, which can translate to systematic errors in the calculated slowness when the calculation assumes the stations are on a horizontal plane. Therefore the relative arrival times were corrected (on the order of 0.2 to 9 milliseconds) for the time associated with the vertical path difference between the true station elevation and the elevation of the centroid of the array. A surface velocity of 3.06 km/s was assumed for this calculation.

Subsequent array analyses were performed on these pre-processed day-long data files. Each component of each array station was processed separately for the determination the apparent slowness vector. The vertical components were not used because the signal strength was much lower as expected for S-waves and is therefore close to the background noise. Several different size analysis windows were used to process the data, ranging from five-minutes to thirty seconds. The longer windows were used to analyze the

first 16 days of the sequence and the thirty-second windows were used to examine finer scale changes in the tremor during shorter but representative time periods.

3.2 Determination of relative arrival times and the apparent slowness

3.2.1 Cross-correlation analysis

The relative arrival times of the tremor at the different stations within an array were determined by cross-correlating the waveforms for a given orientation at all station pairs. Sub-sample time delays were obtained by searching for local maxima in the cross-correlation function, fitting a parabola to the values nearest that maxima, and then calculating the lag time corresponding to the peak of the parabola. Time delays greater than 0.25 s were thrown out because they are not realistic for a sub-surface seismic source given the maximum inter-station spacing of 568 m (Table 2). Each remaining time delay was then used in a weighted least squares linear regression to solve for relative arrival times that best fit a plane wave crossing the array. The weights were determined based on the relative size of the first two cross-correlation peaks, which is discussed later in Section 3.2.2.

Following Aster et al. (2004) this process can be described using matrices:

$$\mathbf{A} * \underline{s} = \underline{\delta t}, \tag{1}$$

where **A** is the product of a matrix describing the reciprocal of the inter-station spacing in x and y coordinates between station pairs, $\underline{\delta t}$ is a column vector containing the pair-wise relative time differences, and $\underline{s}$ is a two element vector containing the East and North components of the slowness of an assumed plane wave. Weights are applied to **A** and to $\underline{\delta t}$ in the following manner:

$$\mathbf{A_w} = \mathbf{C}^{-1/2} * \mathbf{A}, \tag{2}$$

and

$$\underline{\delta t}_w = \mathbf{C}^{-1/2} * \underline{\delta t}, \tag{3}$$

where $\mathbf{C}^{-1/2}$ is a diagonal matrix whose values are the reciprocals of the estimated errors in the observed travel-time differences. Now the equation to be solved has the form

$$\mathbf{A_w} * \underline{s} = \underline{\delta t}_w. \quad (4)$$

Multiplying both sides by the transpose of the matrix $\mathbf{A_w}$ and dividing each side by $\mathbf{A_w}^T * \mathbf{A_w}$, the solution is

$$\underline{s} = (\mathbf{A_w}^T * \mathbf{A_w})^{-1} * \mathbf{A_w}^T * \underline{\delta t}_w. \quad (5)$$

The error in the estimate of slowness can be calculated from the estimated errors in the data.. The covariance of a product between a matrix and a vector of random variables can be rewritten as

$$\mathrm{cov}(s) = \mathrm{cov}(\mathbf{G}*\underline{\delta t}_w) = \mathbf{G} * \mathrm{cov}(\underline{\delta t}_w) * \mathbf{G}^T, \quad (6)$$

where

$$\mathbf{G} = (\mathbf{A_w}^T * \mathbf{A_w})^{-1} * \mathbf{A_w}^T, \quad (7)$$

and the weighted data have a covariance equal to the identity matrix. Thus the covariance in the model simplifies to

$$\begin{aligned}\mathrm{cov}(\underline{s}) &= (\mathbf{A_w}^T * \mathbf{A_w})^{-1} * \mathbf{A_w}^T * \mathbf{I} * \mathbf{A_w} * (\mathbf{A_w}^T * \mathbf{A_w})^{-1} \\ &= (\mathbf{A_w}^T * \mathbf{A_w})^{-1}. \quad (8)\end{aligned}$$

The residual can be determined from the difference between the observed relative arrival times and those predicted by the estimated slowness,

$$\underline{err} = \underline{\delta t}_{observed} - \underline{\delta t}_{modeled} = \underline{\delta t} - \mathbf{A} * \underline{s}. \quad (9)$$

If the errors follow a normal distribution and are statistically independent then the weighted misfit,

$$M = \underline{err}\ \mathbf{C}^{-1}\ \underline{err}$$

should have a chi-squared distribution with an expected value of N-2, where

$$N = Nsta * (Nsta - 1) / 2$$

is the number of pairs of seismograms.

3.2.2 Determination of the errors on the relative arrival times

An important part of this analysis is quantifying the errors in the data. Our estimate of the error comes from the inter-station cross-correlation functions. The relative size of the two largest local largest local maxima of the cross-correlation is used as a measure of the uncertainty of the relative arrival time for a station pair. If the data from two stations are well-correlated, then the correlation function has a large peak for the first maxima with respect to all other maxima. If the data from two stations is poorly correlated, the height of the first correlation peak is smaller and may be a similar value to the next maxima, making it impossible to determine which peak is the true relative phase (Figure 12). In order to quantify the relative errors in the data, the ratio between the first and second correlation maxima is plotted with respect to the residual of that model pair (Figure 13). The rationale being, if the ratio of the amplitude of the two peaks is one, the maxima are indistinguishable and the error should be comparable to the time difference between adjacent peaks in the cross-correlogram. We set this to 0.25s. If instead the ratio is greater than 2.2, then the error should be small (0.005 s), as the residual in the data flattens. This curve is fit with a parametric equation that allows for a mapping between the ratio of the correlation peaks and the error in the relative arrival time. In this case that equation was chosen to be

$$\sigma = (250^{-1/8}+0.3*(R-1))^{-8}/1000, \quad (10)$$

where R is the ratio of the amplitude of the first maximum correlation peak to the amplitude of the second peak. If the value of σ is less than 0.005 s, it is set to be 0.005 s.

3.2.3 Testing array analysis techniques on local and regional earthquakes for determination of the error in apparent slowness.

(Note: This section is a summary of La Rocca et al. (BSSA, submitted 2006) as it relates to this study. Unless otherwise noted the ideas in this section are from that paper.)

An independent way of measuring the uncertainty in the computed apparent slowness was undertaken by La Rocca et al. (BSSA, submitted 2006), where regional and local earthquakes were analyzed using the three arrays. In our study, the array-computed apparent slowness and back-azimuth was compared to the values predicted by the hypocentral locations determined by the Pacific Northwest Seismograph Network (PNSN). The difference between the array-computed slowness and back-azimuth were also compared to the values predicted by theory (Saccorotti and Del Pezzo, 2000; La Rocca et al., 2004) (Figure 14). Finally, using only the array-computed slownesses, the earthquakes were located using a probabilistic source location method (Saccorotti and Del Pezzo, 2000; La Rocca et al., 2004), and those locations were compared to the network-determined hypocentral locations. Using earthquakes to test the array resolution allows for direct comparison of the calculated slowness vector and locations to a well-established and reliable method of locating seismic events.

The theoretical array response in two frequency bands was calculated for each array (Figure 15). The almost circular isolines for Lopez and Sequim arrays indicate that the array response is independent of direction, and so the errors in the slowness in the east and north directions will be roughly equal. The elliptical isolines at Sooke are a reflection of the elongated array configuration. Errors in apparent velocity will be largest for signals propagating along the azimuth of the long axis of the ellipse (~N15E), and errors in back-azimuth will be largest for signals propagating along the short axis (~N105E). As expected, the higher frequencies have a tighter correlation peak, than the lower.

The slowness at each array was calculated using the Zero-Lag Cross-Correlation (ZLCC) technique (Frankel et al., 1991; Del Pezzo et al., 1997) for 51 earthquakes. The computed slowness and back-azimuth of the source were then compared to the expected slowness and back-azimuth given the network-determined location of the earthquake. The average of the stacked

distributions of estimated ray parameter for P- waves is 0.128 + 0.021 s/km and for S-waves is 0.224 $\pm$ 0.031 s/km, respectively. Statistical analyses of the difference between the theoretical and calculated values yield a standard deviation in the back-azimuth of 10 degrees for P-waves and 8 degrees for S-waves and a standard deviation in the apparent slowness of 0.021 s/km for P-waves and 0.033 s/km for S-waves. These values showed very good agreement with the theoretically estimated errors associated with the propagation parameters of the waves as a function of slowness (Figure 16).

In addition to exploring the errors in the array processing for the determination of slowness vectors, these errors were propagated back into location errors. Lastly the network locations were compared to locations determined using a probabilistic source location method (Saccorotti and Del Pezzo, 2000; La Rocca et al., 2004). This probabilistic location method is similar to the method used in the current study, which is described in detail in Section 3.3. While the method of La Rocca et al. (2004) allows for the inclusion of relative arrival times as a constraint on the location, the locations were determined without relative arrival times as a test for their use in tremor locations in which phases cannot be reliably identified and timed across inter-array distances. The locations were in general in agreement with the PNSN locations where the horizontal and vertical distances between the array-calculated and the catalog hypocenter were $\Delta H \leq 10$ km and $\Delta z < 5$ km, respectively.

3.3 Tremor location procedure

The location of the tremor sources was determined by minimizing the misfit between the array calculated slowness values and those predicted by rays traced through a velocity model from trial locations. We used two different S-wave models that were based on P-wave velocity models and a Poisson's ratio of 0.25. These models were a 1D linear gradient velocity model based on the P3 velocity model used by the PNSN to locate earthquakes, and

a 3D P-wave velocity model based on regional and local earthquakes as well as data from the SHIPS experiments (Crosson, 2004). The majority of energy contributing to the tremor signal is from SH-waves (La Rocca et al., 2005). To get our S-wave velocity model we assume a constant ratio between S- and P-wave velocities. Analysis by La Rocca et al. (BSSA submitted, 2006) shows that the ratio between Vp and Vs is constant and equal to 1.75 for analyzed earthquakes.

The travel times and slowness at each array for the 1D model were calculated using the java package TauP (Crotwell et al., 1999). The S-wave velocity model is shown in Table 3. The travel time and slowness were calculated over a series of depths and ranges of distances for the first arriving S-wave phase. These tables of values were then interpolated in order to obtain the slowness and travel time between the points in a regular grid and the centroid of each array.

The same grid was used for the 1D and 3D model calculations. The origin of the grid was 11 km above sea level at 46.25 degrees north latitude and 124.5 degrees west longitude. The grid was then converted to relative kilometer distances using a UTM zone 10 conversion. The extent of the grid in kilometers was 245 kilometers in longitude and 275 kilometers in latitude. The 1D model had a maximum depth of 99 km, which corresponds to a true depth of 88 km. The maximum depth of the 3D model was limited to 76 km, which translates to 65 km in true depth. The grid spacing was 5 km in x-y and 3 km in depth.

The locations of the events were estimated by minimizing the misfit, M, between the observed and calculated slowness computed at each array and the model calculated slowness (1D and 3D), which for this data can be represented as follows:

$$M(\underline{x}) = (\underline{S}_{obs} - \underline{S}_m(\underline{x}))^T * \mathrm{cov}(S_{obs})^{-1} * (\underline{S}_{obs} - \underline{S}_m(\underline{x})), \quad (11)$$

where $\underline{S}_{obs}$ is a column vector of the Sx and Sy for the east-west and north-south components at each array (a total of 12 values) and $\underline{S}_m$ is the predicted

value of slowness in x and y for a given x, y, z grid position ($\underline{x}$). This is the χ^2 statistic which can be compared to the theoretical χ^2 distribution with m-n degrees of freedom, where m (number of observations) – n (number of model parameters) is 10. The expected value of the χ^2 distribution for a large number of degrees of freedom approaches the number of degrees of freedom, ν. Thus if the errors in the data have been properly characterized and the model is reasonable, the value of the minimum misfit should be 10, and the errors in the misfit are characterized by the 95% confidence interval, which for 10 degrees of freedom is 18.307.

However, our misfit values are larger (by an order of at least 5-10) than predicted by the χ^2-distribution, and thus have unreasonably small probabilities of occurrence. This is likely to result from underestimating the uncertainties in slowness, not considering errors in the 3D wave speeds, and problems in which the slowness calculated on the east and north components differ. This probability is obtained by integrating the probability distribution function from the misfit value out to infinity, where the χ^2-distribution has a probability density function

$$f\chi^2(x) = (2^{\nu/2} * \Gamma(\nu/2))^{-1} * x^{\nu/2-}1 * e^{-x/2}. \quad (12)$$

One reason for the discrepancy could result from our choice of velocity model. It is beyond the scope of this project to determine a better velocity model for the region, and we have characterized the errors in the measured slownesses to the best of our knowledge, therefore we will take a Bayesian approach to understanding the error in our locations (Aster et al., 2005). In essence we will rescale the probabilities of obtaining all the locations within the grid such that they add up to one. We can then add up the probabilities in ever-expanding concentric ellipsoids to determine the area of 95% confidence. We anticipate that the x-y locations will have similar errors but that the depth errors will be greater. This assumption is based on the shapes of contours of the misfits for located events (Figure 17).

3.4 Analysis window determination

An important part of the analysis was to determine how to break the data into analysis windows. There is a large quantity of data to be analyzed and this needs to be done efficiently. Thus for characterizing the entirety of the sequence we sought to minimize the number of windows to analyze while retaining reasonable values of correlation and information regarding the location and movement of the tremor source. For this purpose we chose 5-minute time windows with no overlap to look at the entire sequence as recorded on the arrays.

In order to better understand how the tremor progresses in space and time, we need a smaller time window over which to analyze a smaller subset of data. Another consideration was we wanted to eliminate the need to know the relative arrival times of common signals in each time window between arrays. This set the lower limit on the size of the smallest window. The largest distance between arrays and the largest distance we expect between a source and an array for this analysis is almost 80 km. Assuming the slowest transit over this distance is the surface velocity, 3.06 km/s, the time difference would be 26.1 s. We think this overestimates the largest time difference, because the sources have a velocity move-out of 3.8 – 4.2 km/s (from network data), for this reason we chose windows that are 30s long with a 60% or 30% overlap. Therefore the overlapping 30s time windows are sure to include the same tremor sources at each array when the source is located between the three arrays.

Several different size windows ranging from 30s to 6 minutes (no overlap) were examined to see how the misfits (Figure 17) and subsequent locations (Figure 18) changed with respect to this parameter. Errors in slowness were also examined for the suite of window sizes (Figure 19). The general characteristics, locations and errors remain consistent between the

window sizes, indicating that the larger time windows are still reasonable for examining the bulk properties of the tremor episode.

3.5 Polarization analysis

The principal components of motion in each time window were calculated following the method set out in Jurkevics (1988). For each time window, the seismograms were aligned using the relative time delays, and the aligned seismograms were stacked by component (E, N, and Z). The three resulting stacked seismograms were used to calculate the covariance matrix, and the principal components of motion were determined from the eigenvalues and vectors of this covariance matrix. These principal components of motion can be used to determine the properties of the wave-field such as polarization angle of the principal component of motion, the incidence angle of the wave front, and the degree of rectilinearity or planarity of the wave-field (Jurkevics, 1988). For purely rectilinear motion, only one eigenvalue is significantly different from zero; therefore the degree of rectilinearity can be calculated from

$$r = 1 - ((\lambda_2 + \lambda_3)/2*\lambda_1, \quad (13)$$

where the eigenvalues are ordered in size such that $\lambda_1 \geq \lambda_2 \geq \lambda_3$, and r has a value of one for purely rectilinear motion. For purely planar motion, two eigenvalues are significantly different than zero; the degree of planarity can be calculated from

$$p = 1 - (2*\lambda_3 / (\lambda_1 + \lambda_2)), \quad (14))$$

where p has a value of one for purely planar motion. Other properties such as the azimuth of P-wave propagation or the apparent P-wave incidence angle can be determined from the eigenvectors.

3.6 Beam-forming analysis

In the initial stages of data analysis the technique of beam-forming was used to determine the slowness vector at each array. Each horizontal component of each array was processed separately for the determination the

slowness vector. The vertical components were not used because the signal strength was much lower and was close to the background noise. In the beam-forming analysis, for each time window the seismograms for all the stations at a given array were stacked by component at a given magnitude and direction of slowness. Then the power in that stack was calculated. This was repeated for all reasonable values of slowness (< 0.4 s/km). The power values for a given time window were plotted on an X-Y grid ins slowness space and contoured (Figure 20). This procedure was very useful for identifying time windows with more than one simultaneous active tremor source (Figures 21 and 22).

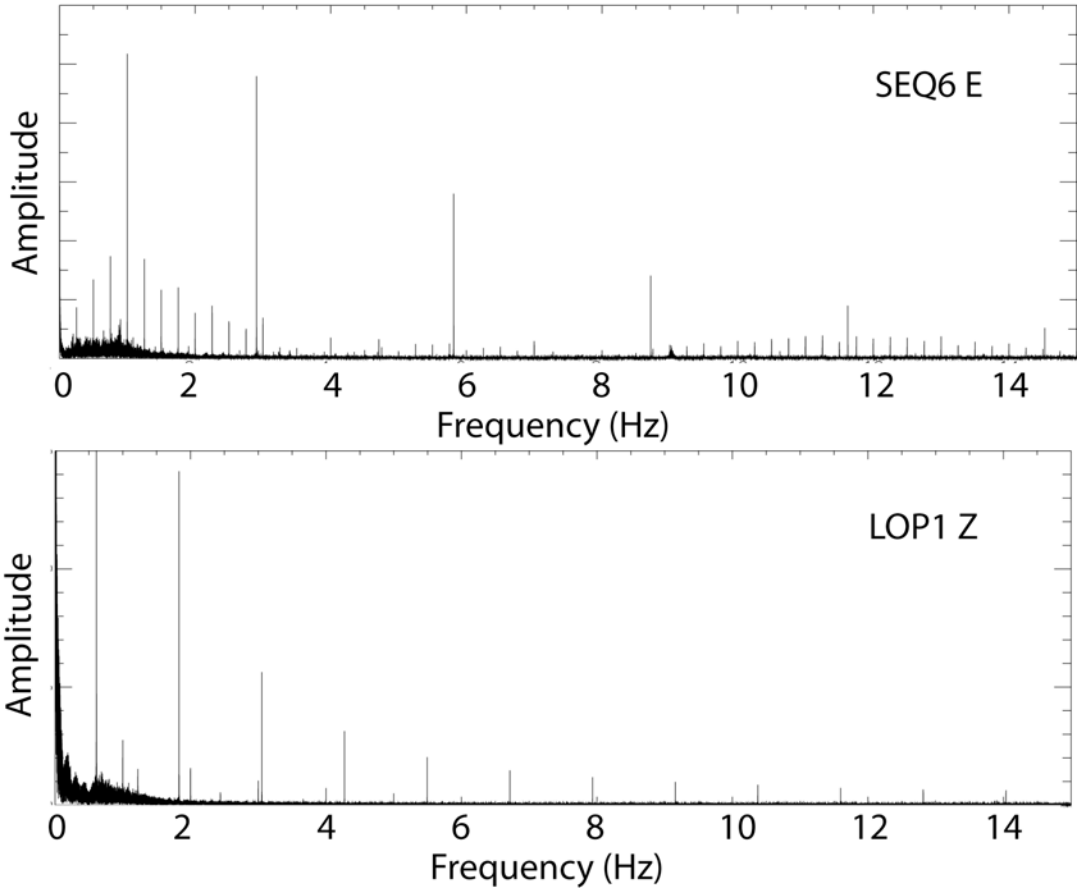

Figure 10 Noise Spectra. Representative examples of amplitude spectra for one hour of data at the Lopez and Sequim arrays showing the regular spikes in the spectra.

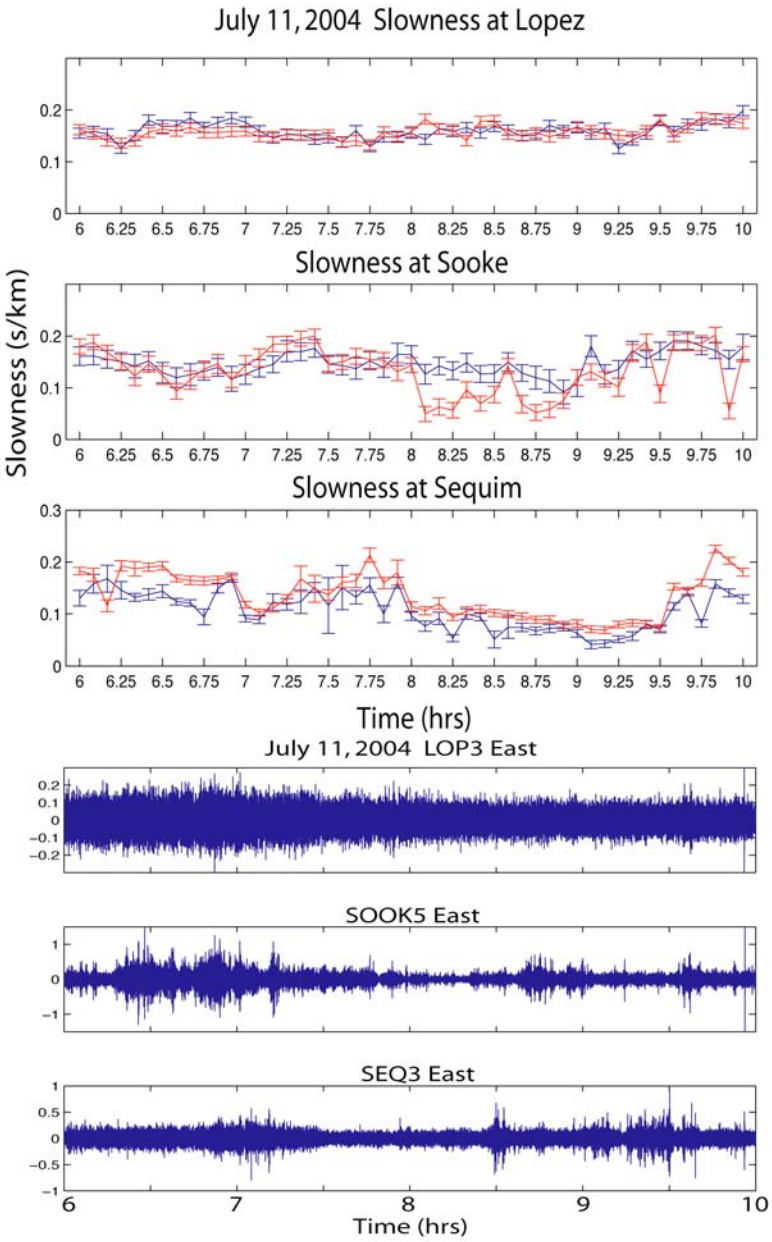

Figure 11 Example of Computed Slowness and Corresponding Seismograms. Slowness values with computed error bars for five-minute analysis windows for all three arrays and an example of the corresponding seismograms at each array. For top figure, horizontal axis is time in hours; the vertical is slowness in s/km. Red points are the slowness computed on the east components of data; blue are for the north. A slightly different filter was used on the Sooke data, thus the errors in the data are slightly larger, but comparable. Slowness calculated on the different components do not always agree within the errors. This disagreement in components is seen at both Sooke and Sequim, even during times when tremor signals are strong.

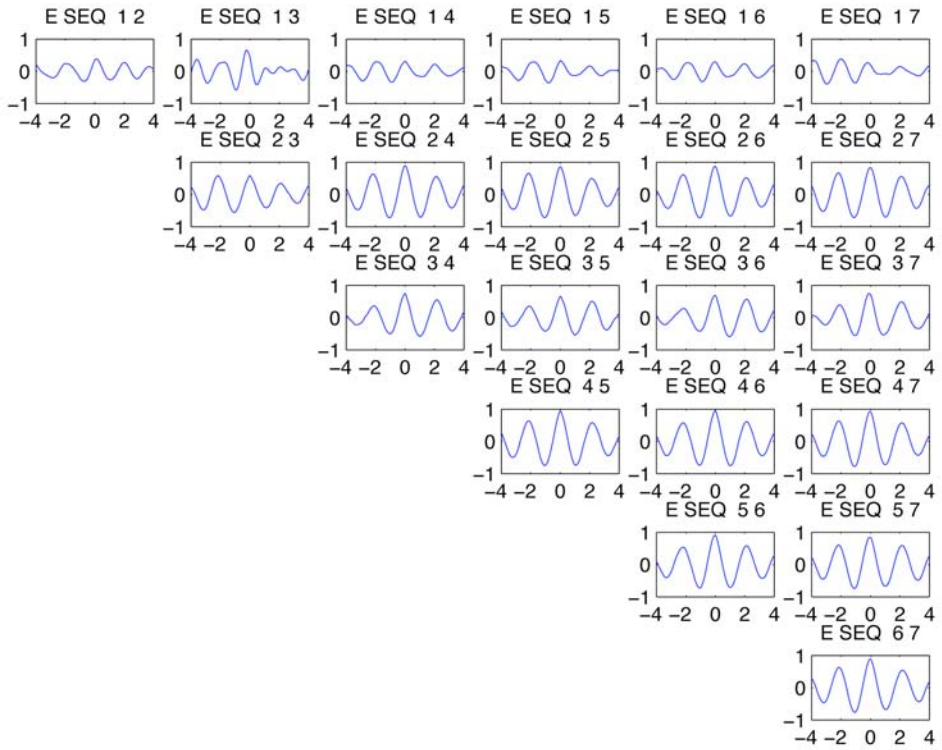

Figure 12 Cross-Correlation Function at Sequim. Cross-correlation functions of a 30s time window on the east components at Sequim array on July 15, 2004. First row is the correlation functions of SEQ1 with all other stations, second row is SEQ2 with the remaining stations, and so on. SEQ1 does not correlate well with the other stations. For stations SEQ2 and SEQ4, the first two correlation peaks are of similar amplitude, showing the complicated nature of choosing the right time lag for time windows with more than one source. This time window includes some of the time windows in Figure 19 where more than one source is active. Horizontal axis is time in seconds, vertical axis is the value of the cross-correlation coefficient.

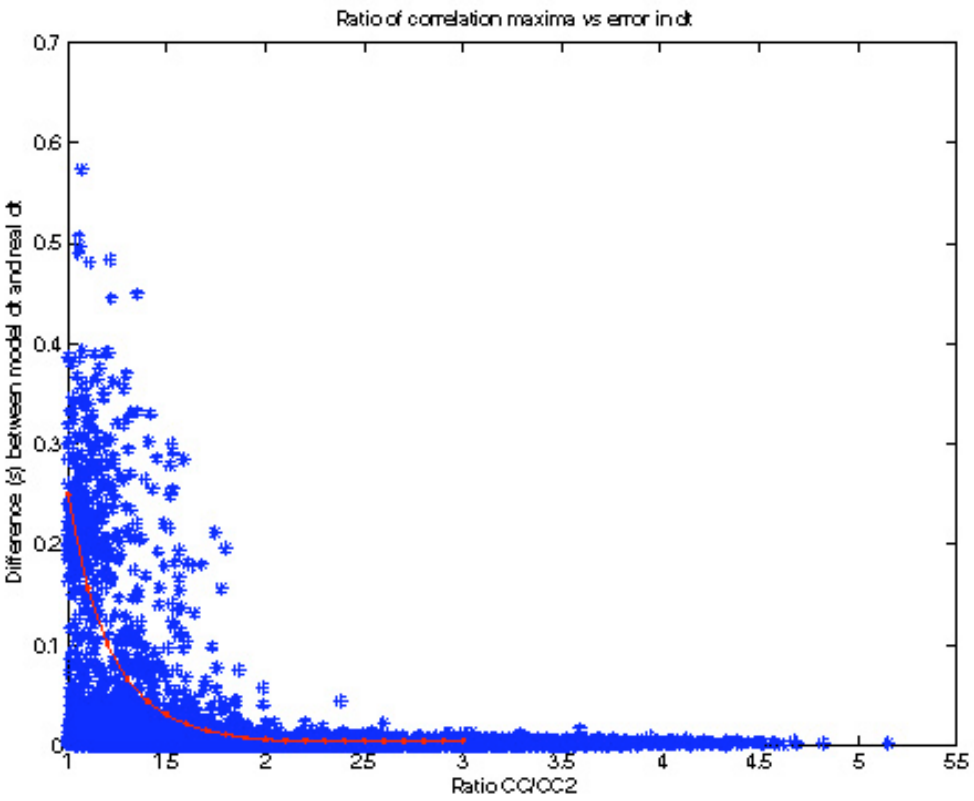

Figure 13 Ratio of Cross-Correlation Peaks Versus Relative Arrival Time Residuals. Figure comparing the ratio of the amplitude of the largest two cross-correlation peaks to the absolute value of the relative arrival times residual. Data for this plot come from all five-minute analysis windows on July 11, 2004. The red curve represents the best fit to these data, as cited in equation 10.

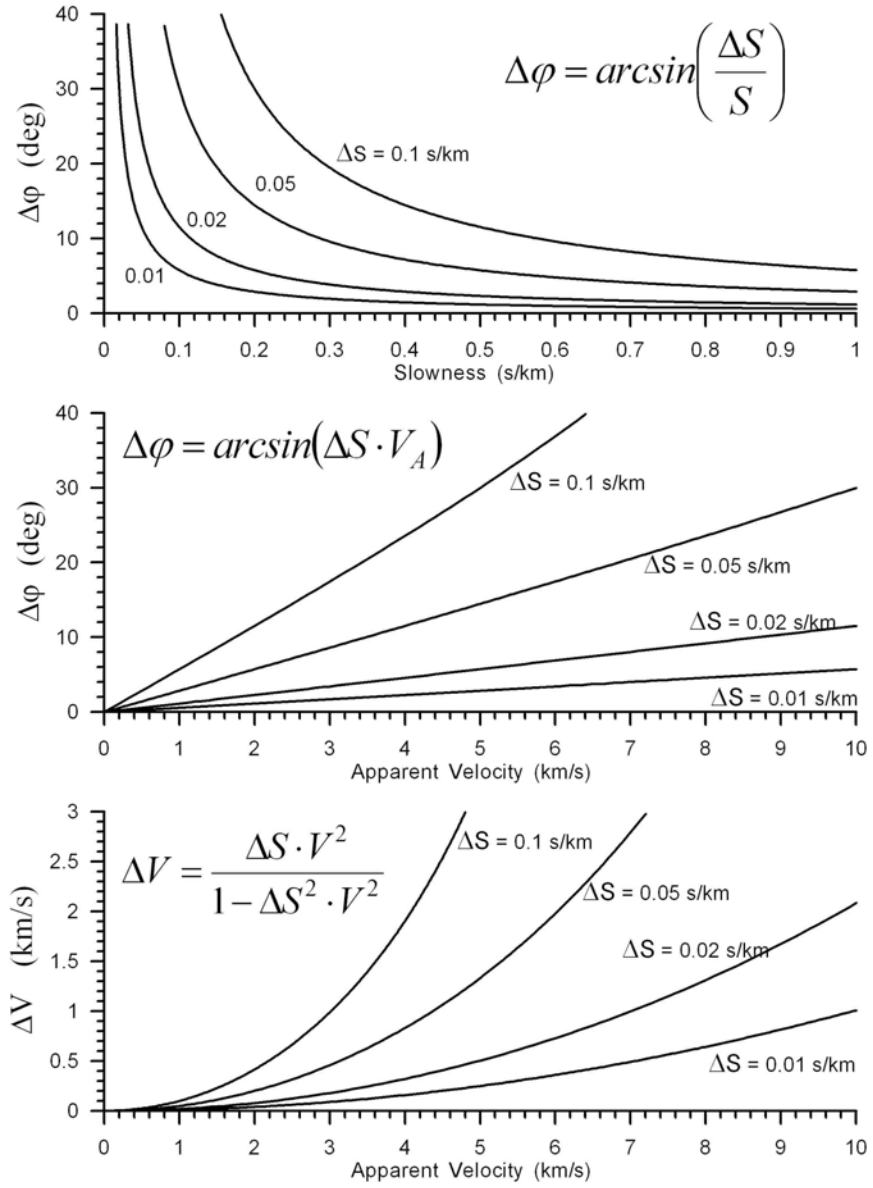

Figure 14 Affect of Slowness Uncertainty on Other Parameters. Families of curves for different values of the slowness uncertainty (ΔS) showing the error on back-azimuth (Δϕ) and apparent velocity (ΔV) as functions of apparent velocity, V and slowness, S (from La Rocca et al., submitted 2006). Equations follow from simple algebraic relations between the back-azimuth and slowness, and slowness and velocity. The top figure shows that as the slowness decreases, the error in the back-azimuth increases exponentially. The bottom figure shows how as apparent velocity increases, so does the uncertainty in apparent velocity. Thus as sources get very deep or beneath the array, the arrays have no resolution in back-azimuth.

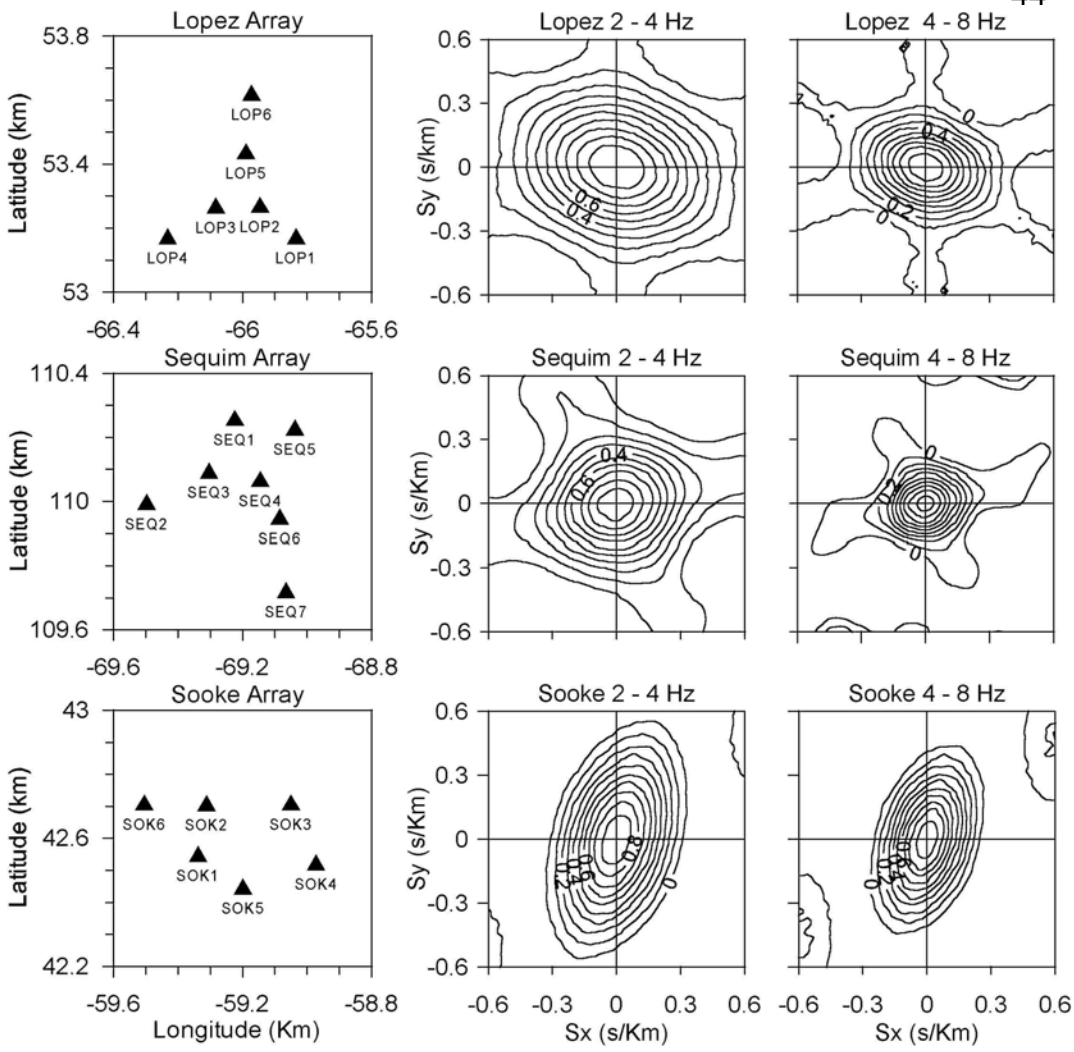

Figure 15 Theoretical Array Responses. Theoretical array responses for two frequency bands. Theoretical array responses calculated at each array using a synthetic seismic waveform. The almost circular isolines for Lopez and Sequim indicate that the array response is independent of direction. The elliptical isolines at Sooke are a reflection of the elongated array configuration. Errors in back-azimuth will be largest for sources arriving along the azimuth N105E, and errors in the apparent velocity will be greatest for signals arriving along the azimuth N15E. The higher frequencies have a tighter correlation peak than the lower.

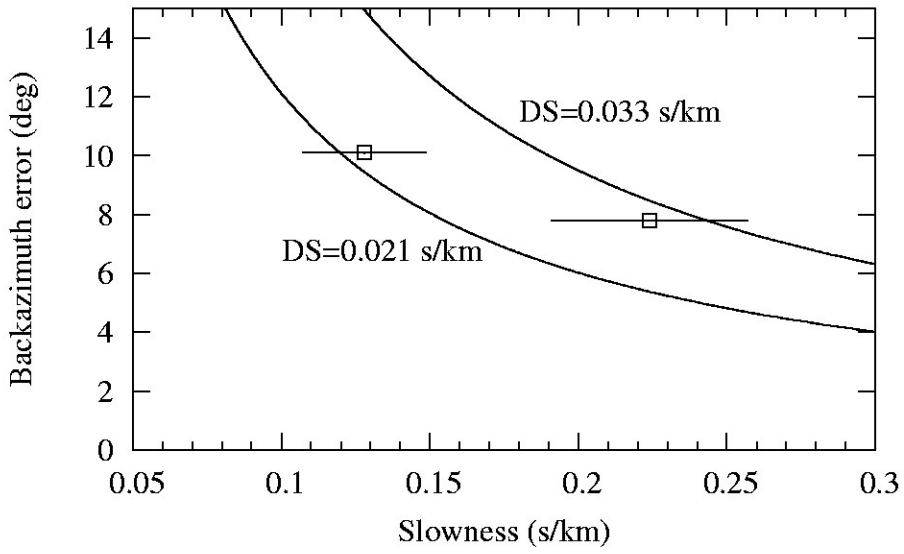

Figure 16 Calculated Versus Theoretical Errors in Slowness. Calculated errors in slowness compared to the theoretical curves. DS is the same as ΔS from previous plots. Curves are plotted for DS = 0.021 s/km and DS = 0.033 s/km, as in the top figure of Figure 14. Squares with error bars are the values of σ_{BP} = 10.1° and σ_{BS} = 7.8° computed from the back-azimuth differences for P ($S_{0P} \pm \sigma_{SP}$ = 0.128 ± 0.021 s/km) and S ($S_{0S} \pm \sigma_{SS}$ = 0.224 ± 0.033 s/km) waves. (figure from La Rocca, submitted 2006). Calculated values agree with theoretical values with the errors.

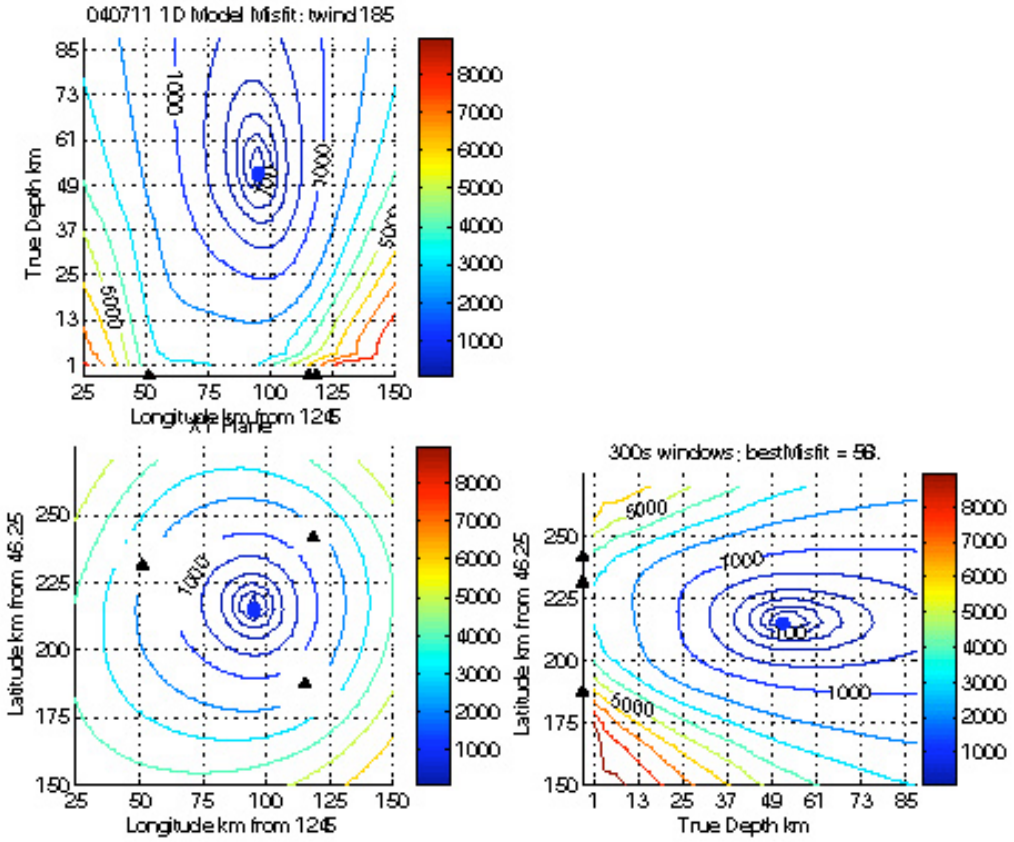

Figure 17 Misfit Contours. Figure showing the contours of the misfit between the 1D model values of slowness and the true array slowness for the 185th time window on July 11, 2004. The contours are show for the X-Y, X-Z, and Y-Z planes, with the best misfit location shown as a blue circle. The locations of the arrays are shown by black triangles. Plotted contours are at misfit values of 75,100, 150,250,500, 1000, 2000, 3000, 4000, 5000, 6000, 7000, 8000, and 9000.

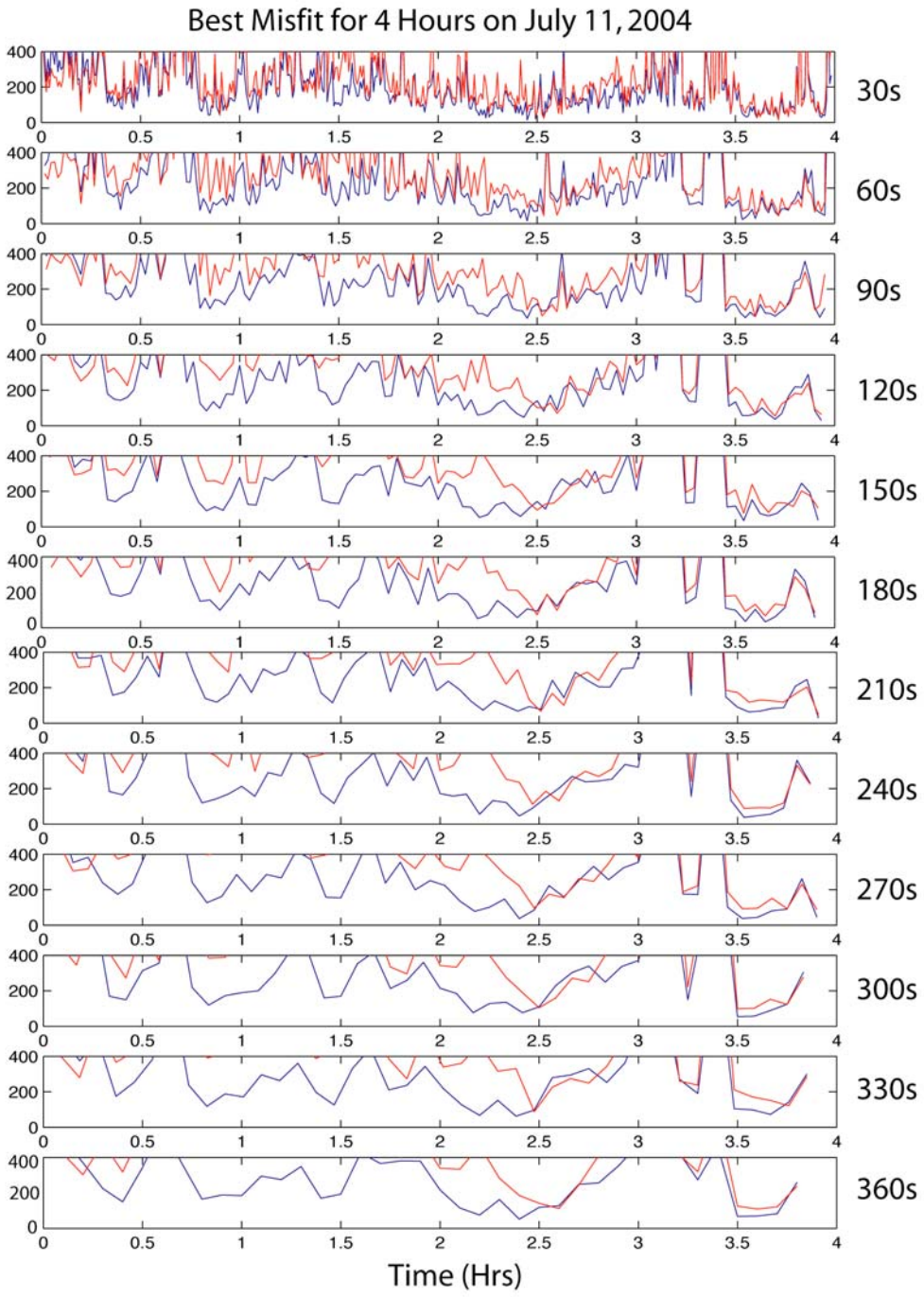

Figure 18 Affect of Window Size on Misfit. Affect of Window Size on Misfit. Plot of best misfit value by time window for different size analysis windows. The same nearly 4-hour period was used, windows had no overlap. Blue line is for a 1D model and red for the 3D model. Different sized windows have very similar values of the misfit just at different resolution. Some windows do not have a good location solution for any of these window sizes.

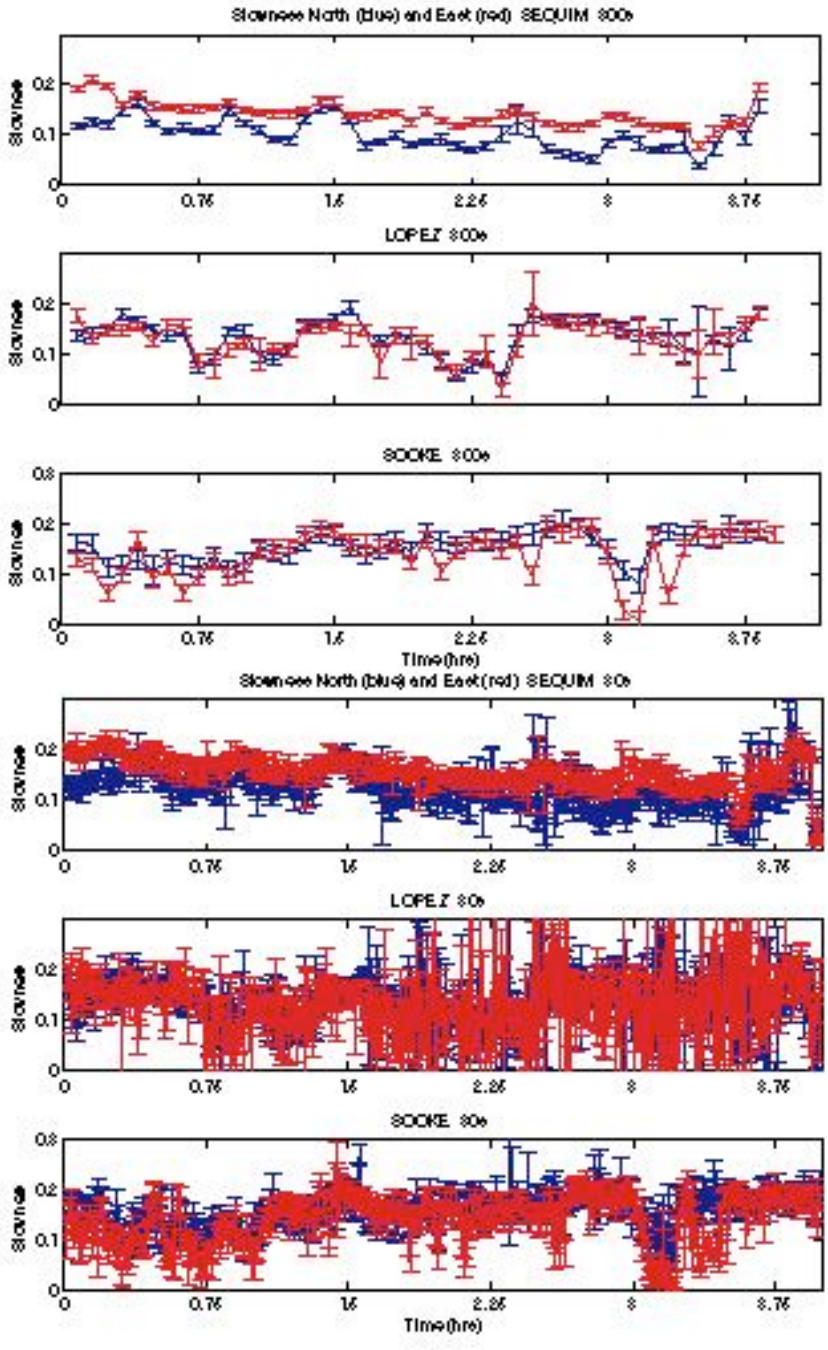

Figure 19 Slowness Values and Errors for 2 Window Sizes. Plot of the slowness and the errors on the slowness comparing 30s and five-minute analysis windows for the last 4 hours of July 11, 2004. Horizontal axis is time. Red is for the E-W components and blue is for the N-S components. This is a particularly noisy section of data (same data as in Figure 15) as illustrated by the size of the slowness errors, particularly on the Lopez array.

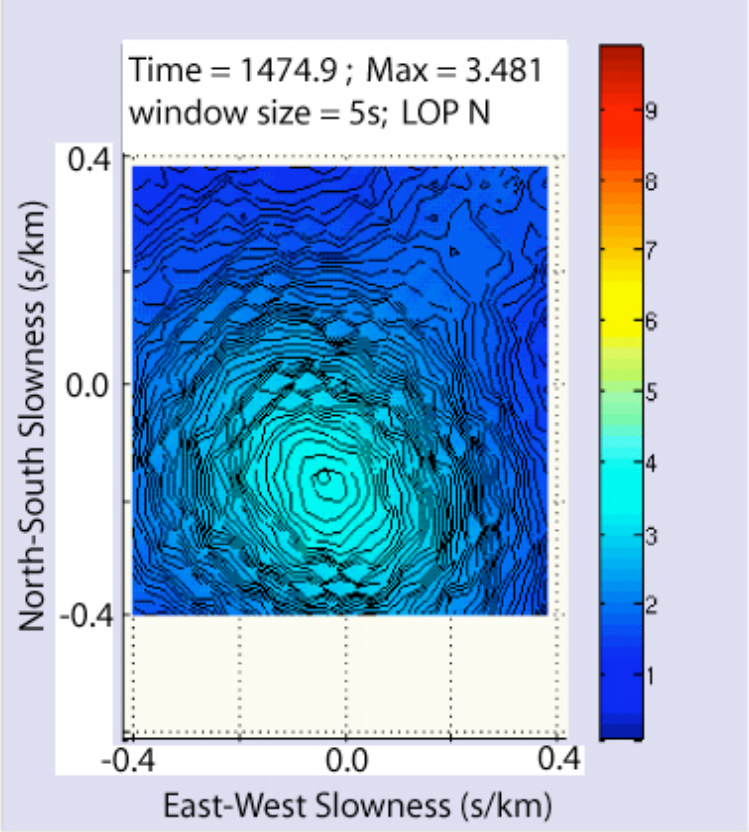

Figure 20 Beam-forming Example. Beam-forming example from Lopez array. Figure is a plot of the power in the stack of the north components at Lopez array for a 5 s time window on July 15, 2004. Color indicates the intensity of the power in the stack at a given slowness vector. The color scale is on the right-side of the figure. In this figure just one active source is resolved by the Lopez array.

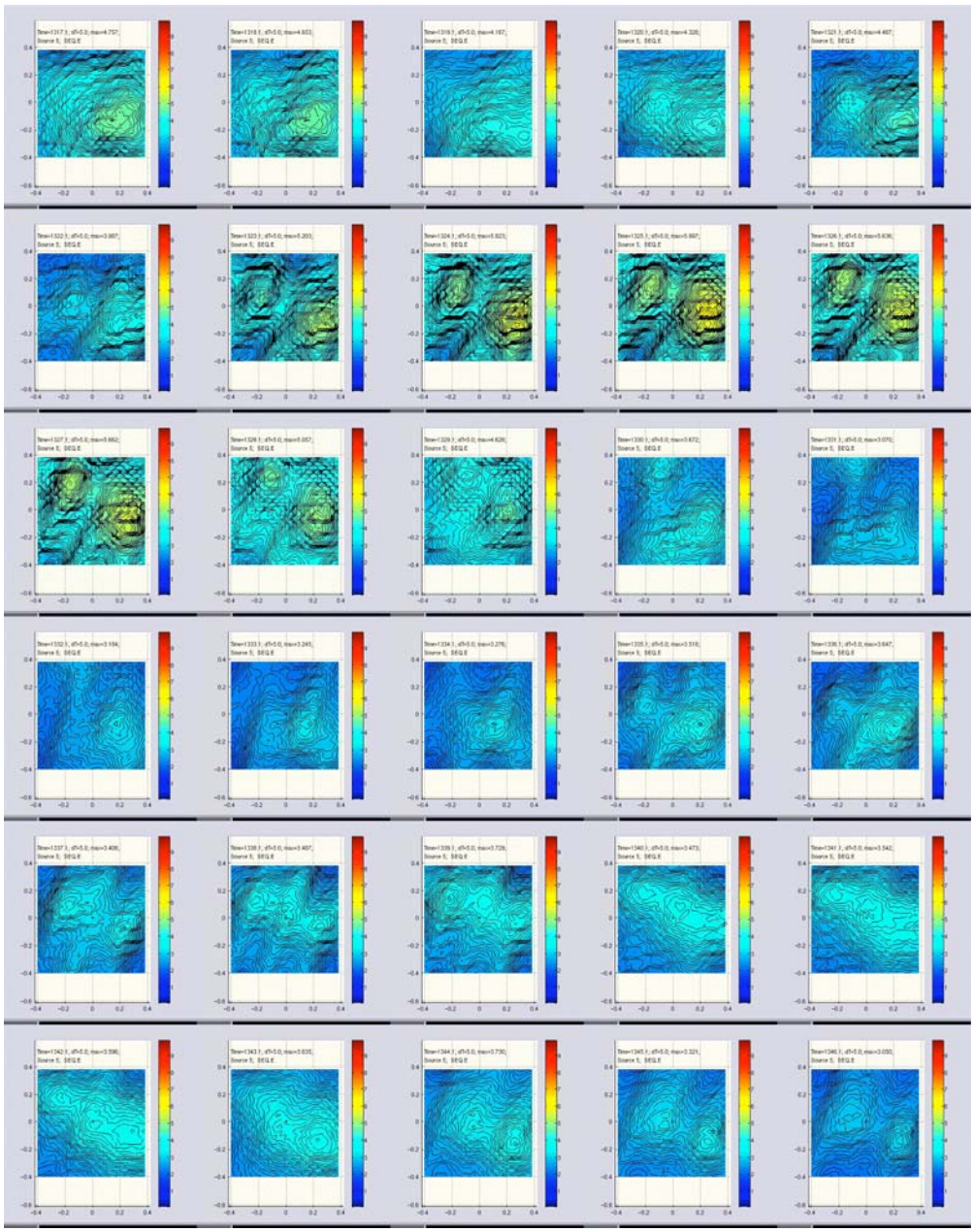

Figure 21 Time Series of Beam-Forming Example at Sequim Array. Time series view of beam-forming results in the slowness plane for the east components of Sequim on July 15, 2004. The time window for each figure is 5 s, and the time between windows is 1 s (4 s overlap). Time begins at the upper left corner, increases to the right, and ends at the bottom right corner. The axes in each figure are the x and y components of slowness ranging between -0.4 and 0.4 s/km. Color indicates the relative power at each value of slowness where red is the most and blue is the least. More than one tremor source is clearly evident in many of the time windows.

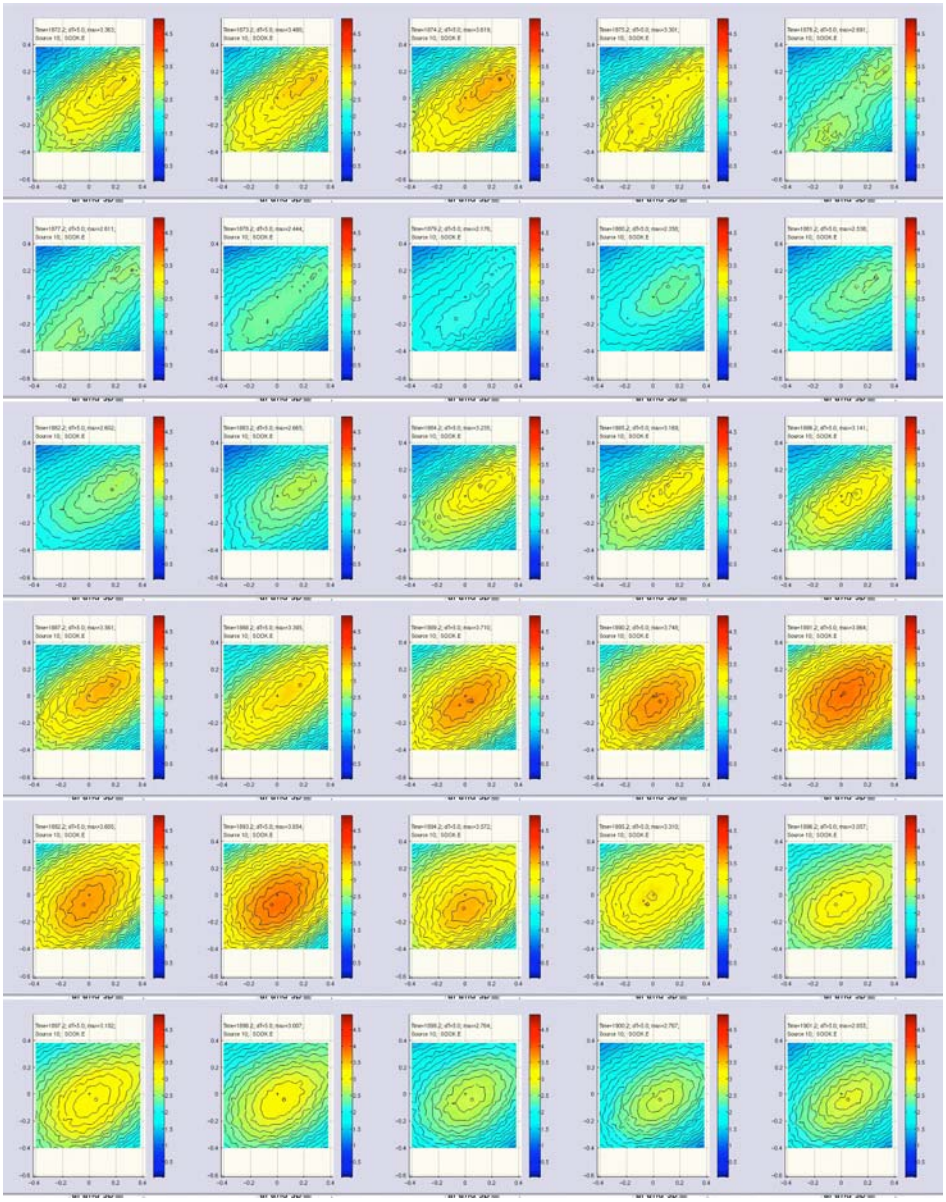

Figure 22 Time Series of Beam-Forming Example at Sooke Array. Time series view of beam-forming results in the slowness plane for the east components of the Sooke array on July 15, 2004. The analysis time window for each figure is 5 s, and the time between windows is 1 s (4 s overlap). The earliest time window is at the upper left corner, time increases left to right, then top to bottom, such that the last time window is at the bottom right corner. Figure axes are the east and north components of slowness ranging between -0.4 and 0.4 s/km. Color indicates the power in the stack at each value of slowness where red is the most and blue is the least. The presence of more than one tremor source is most evident in the upper right figure, subsequent windows show the two sources persist, but become indistinguishable.

Table 3 One-Dimensional Velocity Model. Velocity model used for 1D travel time and slowness calculations

Depth (km)	S-wave velocity (km/s)
0.0	3.06
4.0	3.17542
6.0	3.6373
6.5	3.68349
12.5	3.80473
18.	3.88556
22.5	3.96062
33	4.01258
39	4.09918
42	4.44559
410	4.7

CHAPTER 4:
Array Analysis Results

4.1 General observations

Small aperture seismic arrays are extremely useful for tracking and locating subduction tremor as was suggested by the preliminary array processing results from this study (La Rocca et al., 2005, McCausland et al., 2005). Array processing is more sensitive to low levels of tremor than network data processing is. From PNSN data, we initially determined that the July 2004 tremor episode in Cascadia began on July 8 and lasted until July 24 in the region of the arrays. However, through the cross-correlation of the array data we determined that the tremor sequence in the region of the three arrays lasted from July 6 - 24, 2004 (Figures 23 and 24), and could be recorded on the arrays through July 27, when the arrays were dismantled. Cross-correlating the array data in five-minute analysis windows, we observed that tremor occurred during most hours (at the most, 99%; at the least, 63%) of the tremor episode (Table 4), something that is also not evident from the regional network data alone.

Gross migration of the tremor over many hours to days is consistently observed using network processing and array processing. The first tremor bursts in the July 2004 episode located beneath the region of the Strait of Juan de Fuca east of Lopez and Sequim arrays (Figure 24), and subsequent epicenters migrated first in the east and west directions between the arrays. Then the epicenters migrated bi-directionally, to the south of the strait under the northern Olympic Peninsula and to the northwest of the strait under Vancouver Island (Figure 25 and Appendix 1). This second (bi-directional) migration is the same as was observed from the location of tremor bursts using the PNSN stations (see Chapter 1, section 1.3).

The tremor data are well-correlated between stations (Table 5, Appendix 2). The quality of the correlation between two seismograms is a

function of both the amplitude of the maximum peak of the cross-correlation function and the relative amplitude of the first two peaks of the cross-correlations (Figure 13). The best individual correlations are better than 0.8 and the smallest of the good array-averaged correlations are greater than 0.5.

The data at Lopez had the best signal-to-noise and the data at Sequim had the worst, which was largely a reflection of the geology of the sites. Station 1 at Sequim was located away from any obvious rock outcrops and never correlated well to the other stations and was therefore not used for the analyses. As with network stations the tremor was strongest on the horizontal components. Because the signal was weaker on the horizontal components and close to the noise level, the vertical component data were not analyzed.

The average inter-station cross-correlation, the slowness, the back-azimuth, the degree of rectilinearity, the degree of planarity and the wave incidence angle calculated for the non-overlapping five-minute time windows are plotted for each array and day in Appendix 2. Values are plotted only when the root-mean square error on the relative delay times is less than 20 ms, and when the computed slowness is less than 0.35 s/km. These cut-off values for plotting the data should eliminate noisy data and sources that do not travel with body wave velocities. For the five-minute time windows the data are rarely purely rectilinear or planar, indicating that the wave-field is more complex at that time scale. The slownesses and back-azimuths vary smoothly for most of the analyzed episode. Changes are on the order of 30 to 60 degrees in back-azimuth over 2 to 4 hours, and 0.1 s/km in slowness over 2 to 4 hours (Figure 26). Exceptions to this are seen on Sooke and Sequim arrays when more than one source is active (e.g. July 12 to 17) (Figure 27, Appendix 2).

Errors in slowness and back-azimuth estimated by comparing array-calculated slowness and back-azimuth for regional earthquakes to the slowness and back azimuth calculated from the network location are 0.033 s/km in slowness for S-waves and 8 degrees in back-azimuth (La Rocca et al., submitted 2006). Averaging the weighted root-mean square errors on the

slowness (determined from the slowness inversion) over an entire day (July 11, 2004) on the east and north components are 0.009 s/km and 0.007 s/km respectively on Sooke, 0.013 s/km and 0.018 s/km on Sequim, and 0.006 s/km and 0.006 s/km on Lopez. These errors are based on the ability to measure the relative arrival times between stations, and therefore are smaller than the theoretical slowness and back-azimuth errors and those measured by processing earthquake data (Chapter 3, section 3.2.3).

For the Sequim and Sooke arrays the slownesses and back-azimuths calculated independently on the north and east components do not always agree with each other to within the estimated errors on the Sequim and Sooke arrays (Figures 11, 19, and Appendix 2). This does not occur at the Lopez array. Because this effect was not seen at Lopez, and because it did not always occur at Sequim and Sooke, I can reasonably assume that the discrepancy is not an artifact of the processing techniques, of the station installations or of local site effects. For these same reasons, I do not believe that we have incorrectly characterized the errors in the computed back-azimuth and slowness. I do not yet understand the nature of this discrepancy, but ways of doing so are discussed in Chapter 6.

4.2 Locations

4.2.1 Results from five-minute time window analysis

There are several time scales on which I examined the array data. The largest scale is the day-to-day changes in the locations, for which I used 5-minute non-overlapping time windows to process the data during the time period when the tremor was located in the region between the three arrays (July 6 – 22). Then to track changes on the order minutes, I used thirty-second time windows with a ten-second overlap on a day where the tremor was confined to one source volume (to be discussed in section 4.2.2).

Locations determined from the 3D velocity model had similar epicentral locations to those determined from the 1D velocity model (Figure 28). However the depths rarely converged on a solution within the model space, and most often located at the base of the model. For these reasons, the 3D model was abandoned because the depth problem could not be resolved.

For the July 2004 tremor and slip episode, the tremor began on July 6 beneath the Strait of Juan de Fuca, where the tremor remained through July 11, 2004. During these first days, the majority of tremor epicenters were confined to a small region (approximately 250 square kilometers on any given day), where on a day-to-day scale the tremor epicenters migrated between a region east of Lopez and Sequim and a region to the west between the three arrays separated by a distance of about 50 km (Appendix 1). The depths of the tremor range primarily from 40-60km on July 8 through July 11. Depths are generally, but not always, deeper to the east during these days. The shallowest depths are on July 6 and 7.

More specifically, on July 6 the majority of epicenters are halfway between the Sequim and Lopez arrays in latitude and about 5 km east of the two arrays. On July 7, the epicenters then move northward by roughly 10 km and westward by 5 to 10 km. On July 8 the epicenters move southward by 5 km and westward about 5 km, with a greater spread in the locations in the east-west direction. On July 9 the epicenters move eastward to 15 km east of Lopez and Sequim, without much change in latitude. On July 10 the epicenters move about 25 km to the west (15 km west of Sequim and Lopez). On July 11 the epicenters are in the same region as the previous day, but there are more locations. Finally on July 12, the epicenters cover a large region from about 10 km east of Sooke to about 25 km east of the line between Sequim and Lopez, and they cover 50 km in latitude from Sooke to Sequim.

Appendix 3 contains a sequential series of locations for each hour between 15:00 on July 11 and 2:00 on July 12. On an hourly time scale, the

tremor moved around within this region smoothly, but without any specific pattern (such as upwards or downwards, along a line or outward from a given point).

Beginning on July 12, the epicenters and depths of the tremor became more diffuse, with the tremor epicenters migrating toward the northwest and a minority of epicenters migrating to south of the strait. At this point, the epicenters covered a much larger region, from the lateral midpoint of the arrays extending westward for around 50 km and extending for at least 125 km in latitude (Figure 25). The depths of the tremor were more diffuse and deeper, with many of the events locating at the bottom edge of our grid and had larger errors, particularly in depth.

This greater distribution of locations from these days made the hourly-scale temporal progression harder to follow. Our analysis picks out the strongest source in any given window; therefore when there exist multiple tremor sources, the source that is the strongest in one window may not be the strongest in the next window. This has the potential to cause the temporal progression appear more chaotic or sporadic than it truly is. Binning the locations into larger (15 minute or greater) time slices helped to smooth out this effect.

The apparent widening of the tremor region on July 12 coincided with the time periods in which multiple sources began to be evident based on beam-forming analysis at individual arrays in the slowness domain (Figures 21, 22 and 4.5) and from network locations (Chapter 1). Beam-forming analysis from July 15 showed that from the perspective of the Sequim array, there were tremor sources to the northwest and southwest (Figure 21). From the perspective of the Sooke array, the sources were to the northeast and southeast of the array (Figure 22). These back-azimuth directions are consistent with array locations. Multiple sources were most common between July 12 and 17 (e.g. Figures 4.3 and 4.5), and are easily observed on the Sequim and Sooke arrays. Because each array will most strongly record the

event that is closest to that array, and that source may not be the same for each array, there are time windows in which no location will exist that satisfies the calculated slowness and back azimuth at all three arrays.

Between July 17 and 24, the tremor located primarily around and to the northwest of the Sooke array. Depths during this time period were poorly to completely unconstrained because the Lopez and Sequim arrays were too far away to help constrain the depth. The epicenters had migrated out of our area of robust constraints (between the three arrays) by July 24. Figure 29 shows all locations with misfits less than 200 for July 6 -22. For comparison all locations with no cut-off are plotted on the same figure. The locations are all within the same region and depths, even the data with large errors. Appendix 1 includes two dimensional histograms of the locations for July 6 – July 22 for the five-minute time windows.

The errors in the locations were determined for the five-minute time windows from the size of the 90% region of the misfit calculation. The relationship between the error and misfit for July 11 is shown in Figure 30. The figure is typical of all the analyzed days. Small misfits correspond to the smallest errors in location and the largest misfits have the largest errors in locations, as expected. Figure 31 shows how the average location error varies by day for different upper limits of the misfit. As the misfit upper limit increases, so do the size of the errors in the location. The size of the average error is greater as the days increase and is the worst when more than one source region is active (July 12 – 17) and when the epicenters are closest to the Sooke array.

The errors in the array-determined locations computed by comparison to network-determined locations for earthquake data were less than 10 km in x and y, and less than 5 km in z (La Rocca et al., submitted 2006). The average errors in the locations calculated from the width of the 90% confidence interval for misfits less than 100 between July 6 and July 22 are of the order of 5 km in x, 6 km in y, and 10 km in depth for 300s time windows (Table 6). Average

errors based on the misfit are shown by day in Figure 31 for different upper limits (cut-off) of misfit.

The best locations on July 11 (misfit < 100) are plotted in Figure 32 along with the 90% confidence interval for the locations. The majority of locations are clustered in one region, with one outlier location to the east. Depths are between 37 and 61 km for the cluster. If the misfit criteria is relaxed to misfits < 200, more locations can be plotted. In order to see the locations more clearly the day was broken into the first (top) and second (bottom) twelve hours for Figure 33. In the first half of July 11, there is one source region. In the second half of the day there are two source regions. The more western region is shallower than the eastern region, but error ellipses are larger for the deeper, more eastern region. Smaller analysis windows (30 s) were used to investigate how the epicenters transition between these two regions, or if the two regions are simultaneously active.

4.2.2 Location results from 30-second time window analysis

For further understanding of the progression of the tremor, on a smaller time scale, I looked in detail at windows in the early days of the sequence when the tremor were recorded on all three arrays, were epicentrally located between the three arrays and seemed to be isolated to a small region (e.g. Figures 32 and 33). During the first days of the tremor episode, there was just one source active in a given time window, and the direction and slowness of the waves from a source were steady over time periods of 20-30 minutes or longer (Figure 26). During these time periods and at this time scale, the direction to and slowness of the tremor sources did not vary wildly; rather, the changes in the direction and slowness occurred gradually and systematically. Changes in azimuth were within 30-60 degrees; changes in slowness were within 0.1 s/km. Both of these changes occurred over time periods of 2-4 hours. I examined these time periods using shorter averaging windows to help to elucidate the temporal and spatial changes in the tremor locations. I also

examined the end of July 11, when the tremor moved from one active region to another. Finally I looked at locations on July 15, when more than one source was active.

First I chose July 11 to study in detail, because on this day, the tremor amplitudes were the largest for the days when the 5-minute analysis indicated a spatially limited source region (Figures 32 and 33). In particular, I examined the first six hours of July 11, 2004 in thirty-second time windows with an 18-second overlap (Figure 34). The locations are consistent with those obtained from the non-overlapping five-minute windows (Figure 35). The locations moved around within roughly 15 km in latitude, 40 km in longitude and 20 km in depth. From time window to time window, the locations do not change greatly. The average epicentral change in location was 7 $\pm$ 6 km, and the average change in depth was 5 $\pm$ 5 km. When I examined the distribution of epicenters on the time scale of 15 minutes, the locations vary smoothly over the six hours, but with no obvious pattern to the movement, such as vertically, east-west, north-south etc. Only in the more complicated time windows do the shorter analysis windows show more extreme variation in the tremor source.

During the last hours on July 11, 2004, there was more than one active source region (Figure 32 and Appendix 3). When the same time period was examined in thirty-second time windows with ten-second overlap, the tremor locate in the same two regions (Figure 36). Appendix 4 shows a filmstrip in which each frame represents the thirty-second time window locations binned into five-minute frames. The transition of the tremor from one region to another occurs between 21:00 and 22:00 hours. The tremors do not simply jump from one region to another, but the movement is not smooth either. The epicenters move west to east, back west, and then settle in to the east for a few hours.

Locations from 2 hours on July 15 for thirty-second time windows are shown in Figure 37. The top part of the figure shows locations for misfits < 100 with the 90% confidence region. Errors are larger than for the same misfit criterion on July 11. The bottom part of the figure shows a histogram for

locations with misfits < 600 gives a better indication of the source distributions, which cover a much larger region than in earlier days. The same result was found for the five-minute time windows.

For the thirty-second time window analysis, the windows were overlapped to get better resolution on the migration of the tremor locations and to ensure the same source was present in the window at each array. Figure 38 shows the difference between locations calculated in non-overlapping and overlapping time windows from 4:00 to 6:00 on July 11. For the overlapping windows, more locations within the same region were resolved. Errors plotted with respect to misfit and changes of error with time are plotted in Figures 39 and 40, respectively. The relationship between misfit and error is similar to that for the five-minute windows and size of the errors are similar. The errors are not constant, but become larger and smaller throughout the two hours (Figure 40), which is typical of all analyzed days.

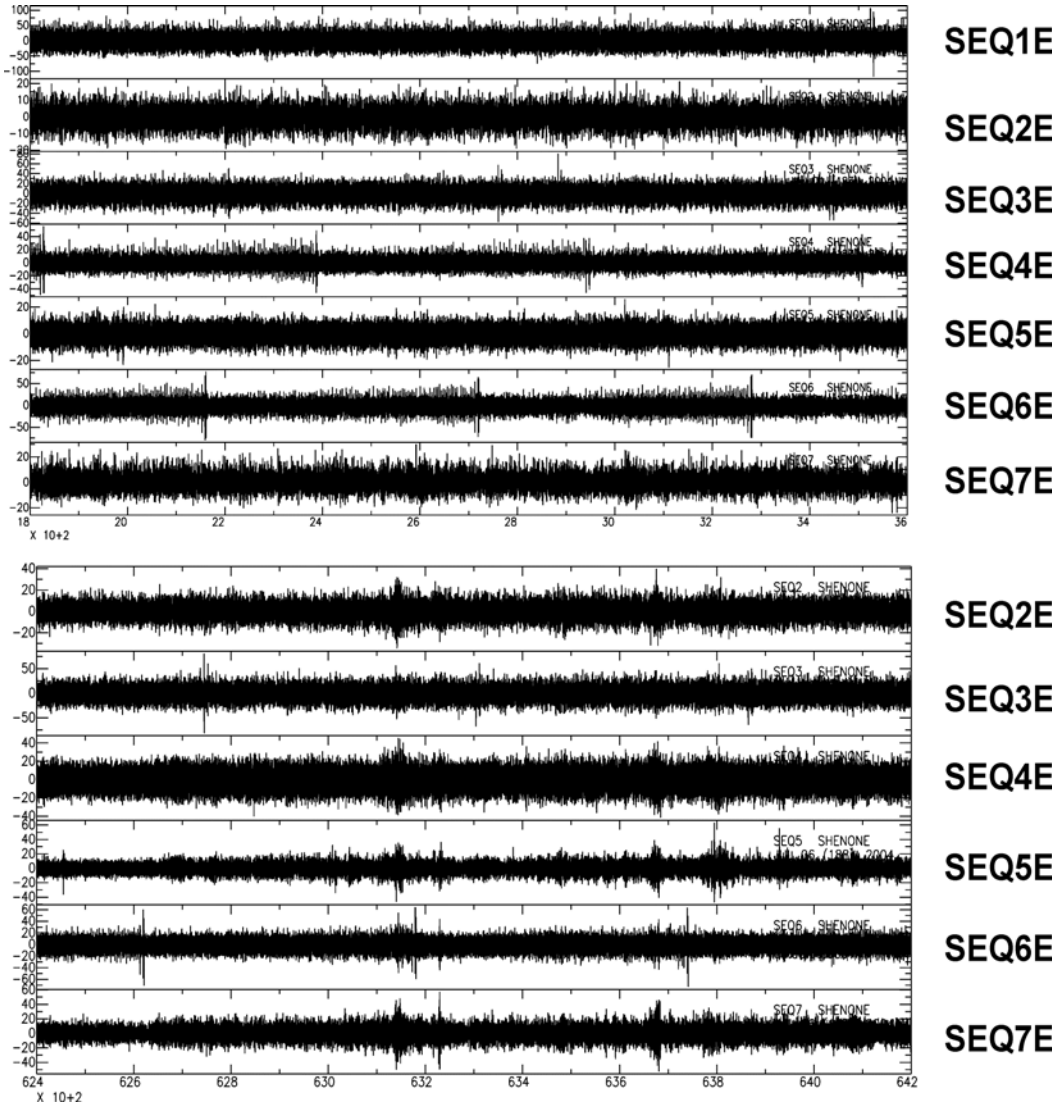

Figure 23 Background Noise and Tremor Onset. Figure showing background noise and then beginning of tremor on July 6, 2004. Top figure is a plot of the band-pass filtered (1-6 Hz) seismograms on the east components of the Sequim stations for 30 minutes on July 1, 2004. There is no tremor during this time period. Bottom figure is a plot of band-pass filtered seismograms on the east components at Sequim for 30 minutes on July 6, 2004. Tremor is just beginning on this day and is only just visible above the noise level.

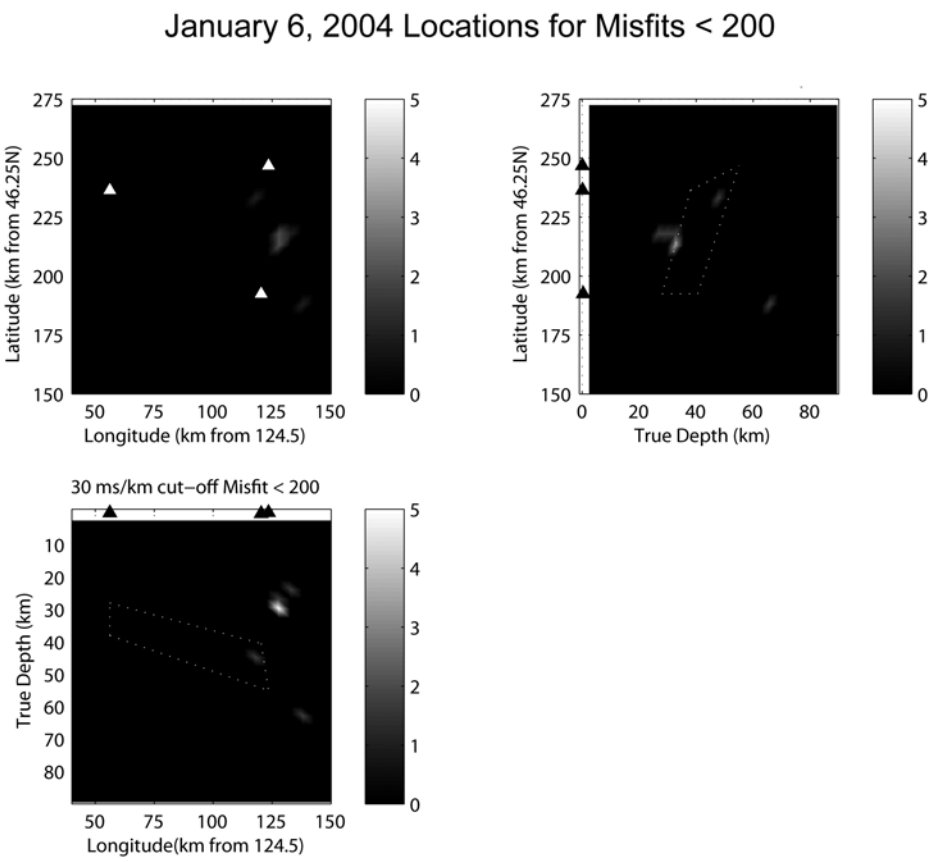

Figure 24 Locations on July 6, 2004. Figure shows 2D histograms of the locations on the first day of tremor during the July 2004 tremor episode. The misfit cut-off for plotting the location is 200. Top left figure is the X-Y plane, top right figure is the Y-Z plane and the bottom left figure is the X-Z plane. Latitude is plotted as kilometers from 46.25 degrees North, and longitude is plotted in kilometers from 124.5 degrees West. The number of locations at any given grid point is indicated by the colorbar to the right; white indicated more locations, and black indicates zero. Locations are between and just east of the Lopez and Sequim arrays with the majority of depths at 30 km.

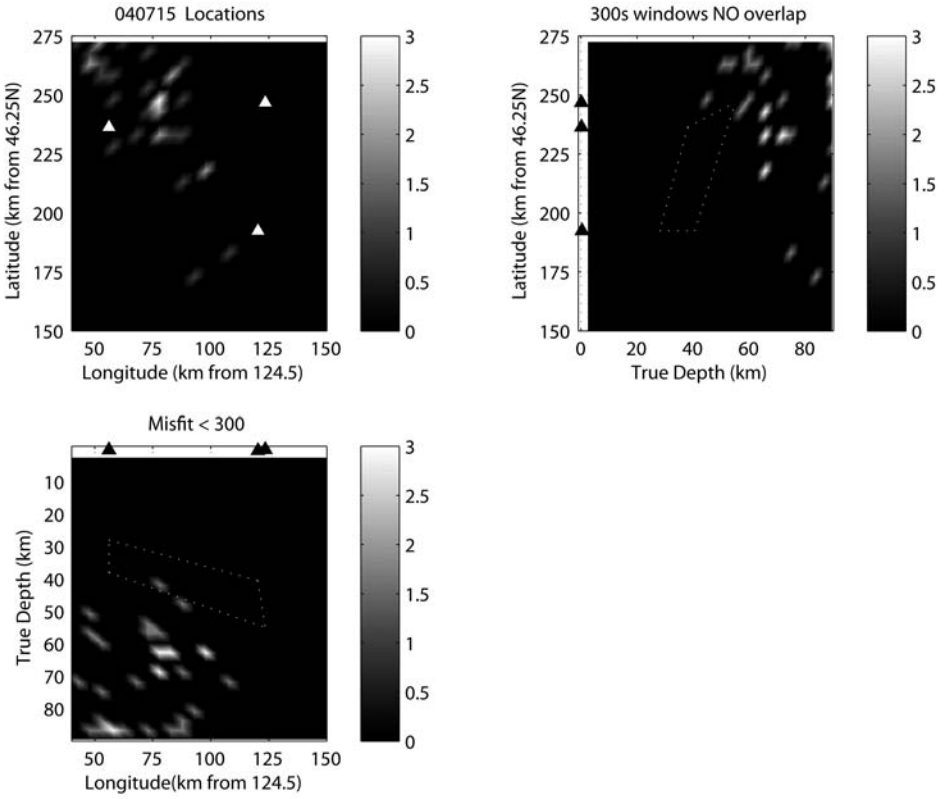

Figure 25 Locations on July15, 2004. 2D Histogram of all locations on July 15, 2004 projected onto X-Y, X-Z and Y-Z planes. Epicentral locations are closer to the Sooke array and distributed over a larger region than previous days. Misfit cut-off for plotting the location was 300.

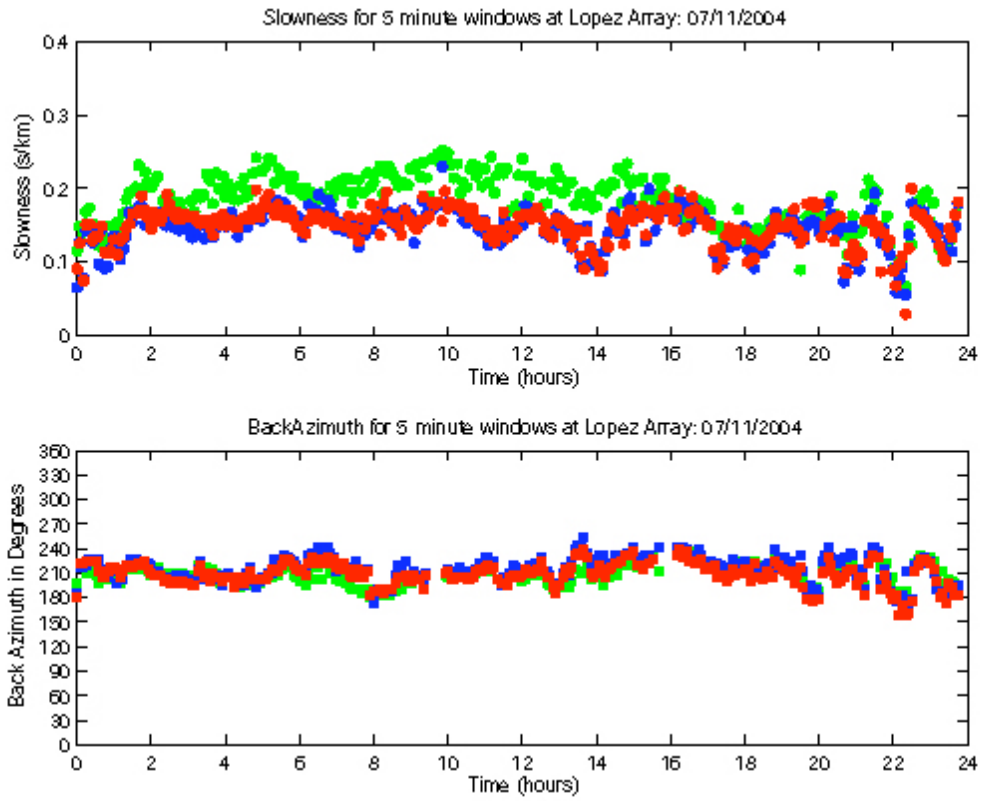

Figure 26 Slowness and Back-Azimuth at Lopez on July 11, 2004Time series of slowness and back-azimuth measured on the Lopez array on July 11, 2004. Time windows were five-minute long. The calculated slowness and back-azimuths vary slowly over around 0.1s/km in slowness and 60 degrees in back-azimuth.

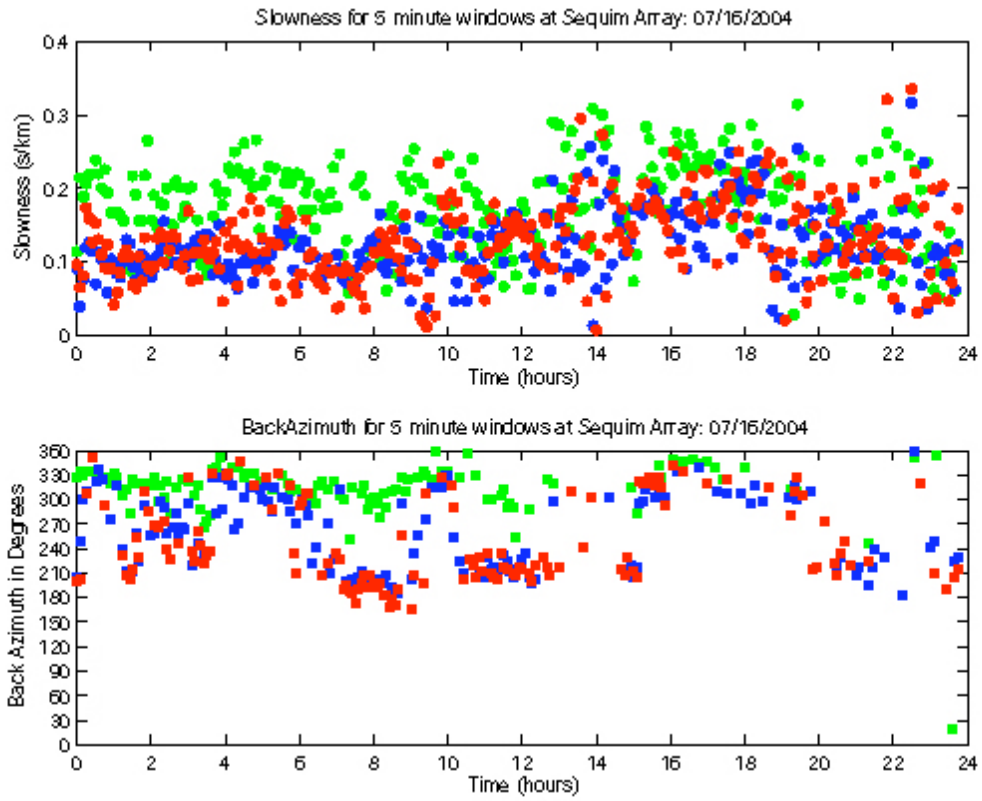

Figure 27: Slowness and Back-Azimuth at Sequim on July 15, 2004. Time series data for slowness and back-azimuth at Sequim array on July 15, 2004 showing presence of multiple active source regions. Back-azimuth jumps between different directions, particularly in the first 12 hours of the day.

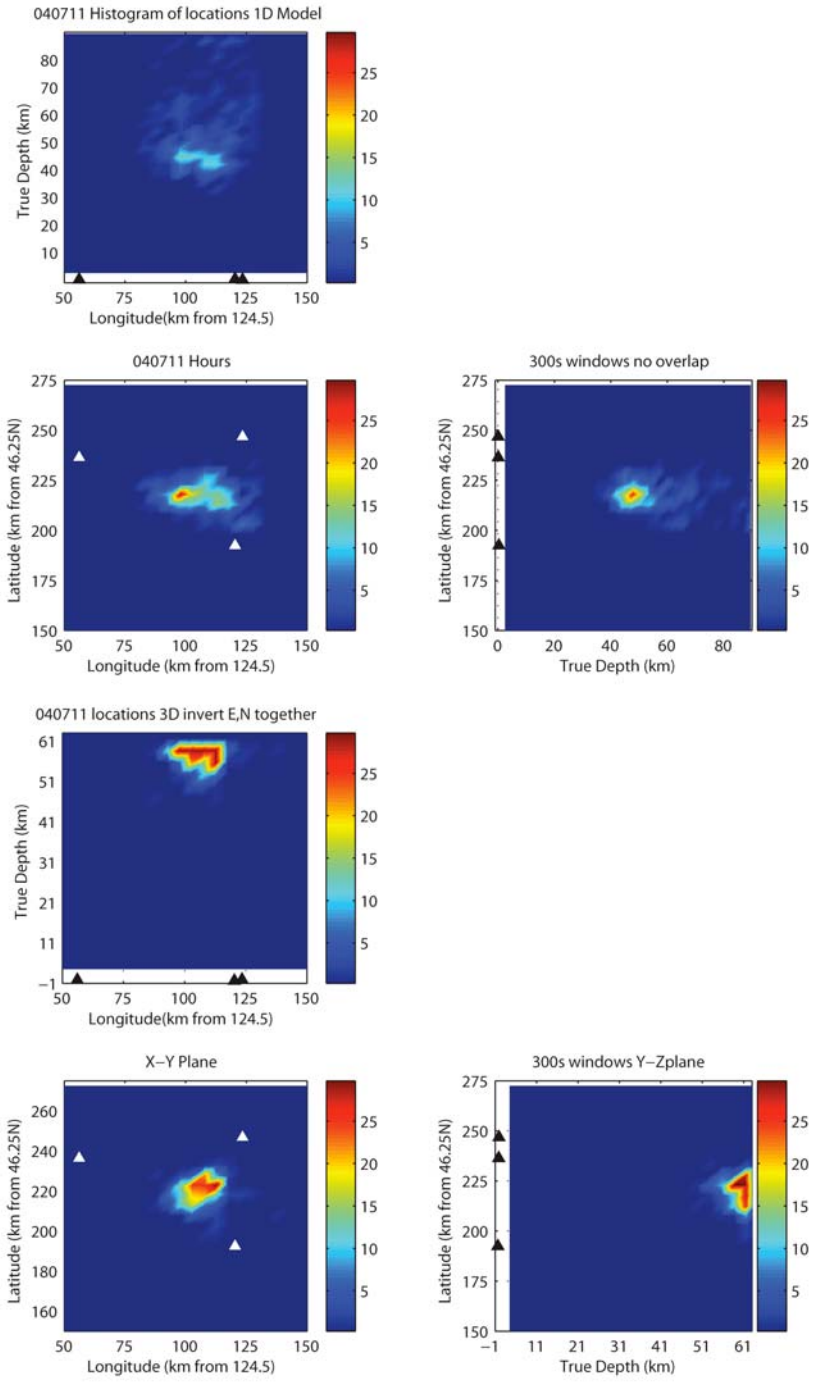

Figure 28 Comparison Between Locations from 1D and 3D Models. Top figure shows two-dimensional histograms of the location using a 1D model. Bottom figure shows the 2D histograms using a 3D model. Epicentral locations are similar, but the depths are not well-constrained for the 3D model.

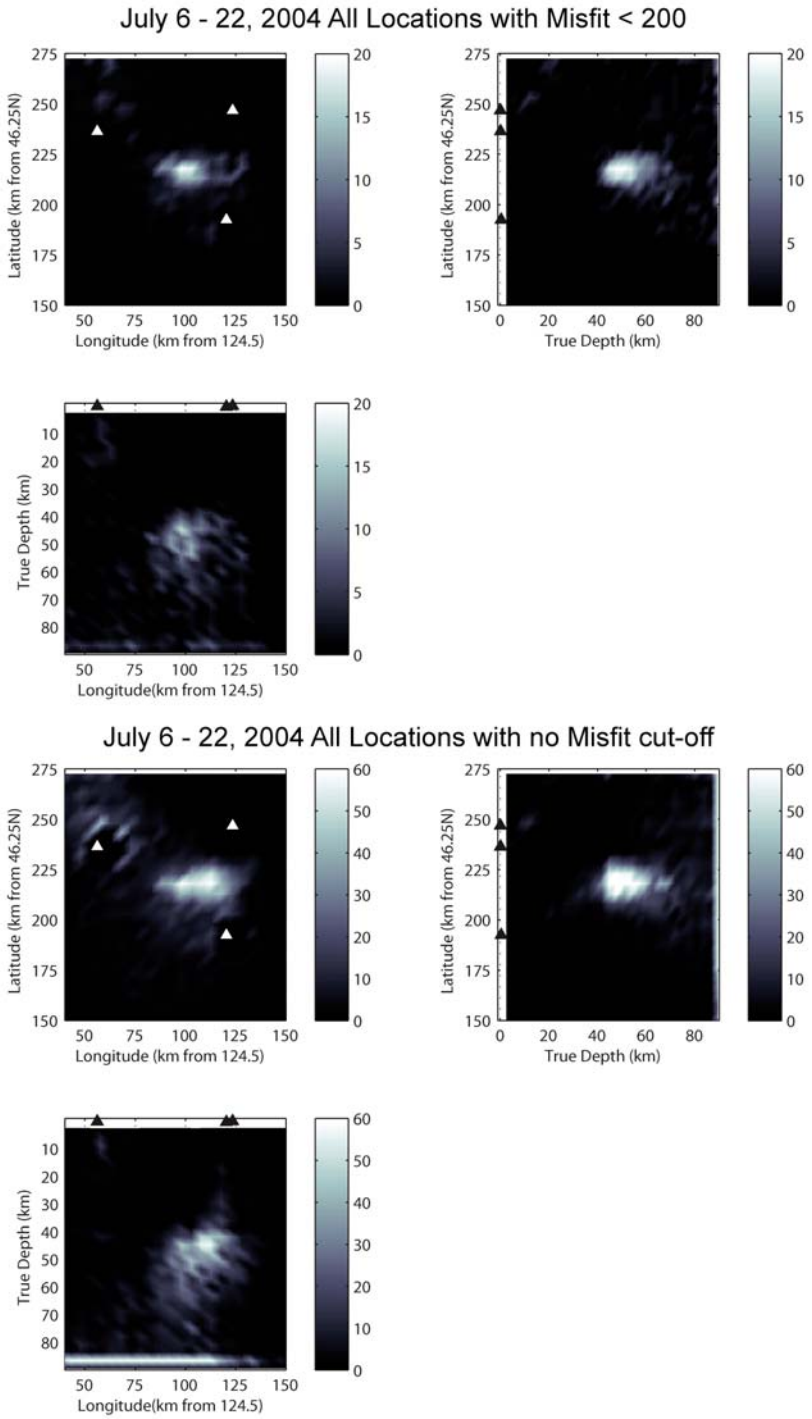

Figure 29 Cumulative locations July 6 – 22, 2004. Figure shows the cumulative locations for 300s time windows from July 6 – July 22, 2004. Top figure has a strict misfit cut off (< 200) for plotting the location. Bottom figure has no cut-off for plotting the location.

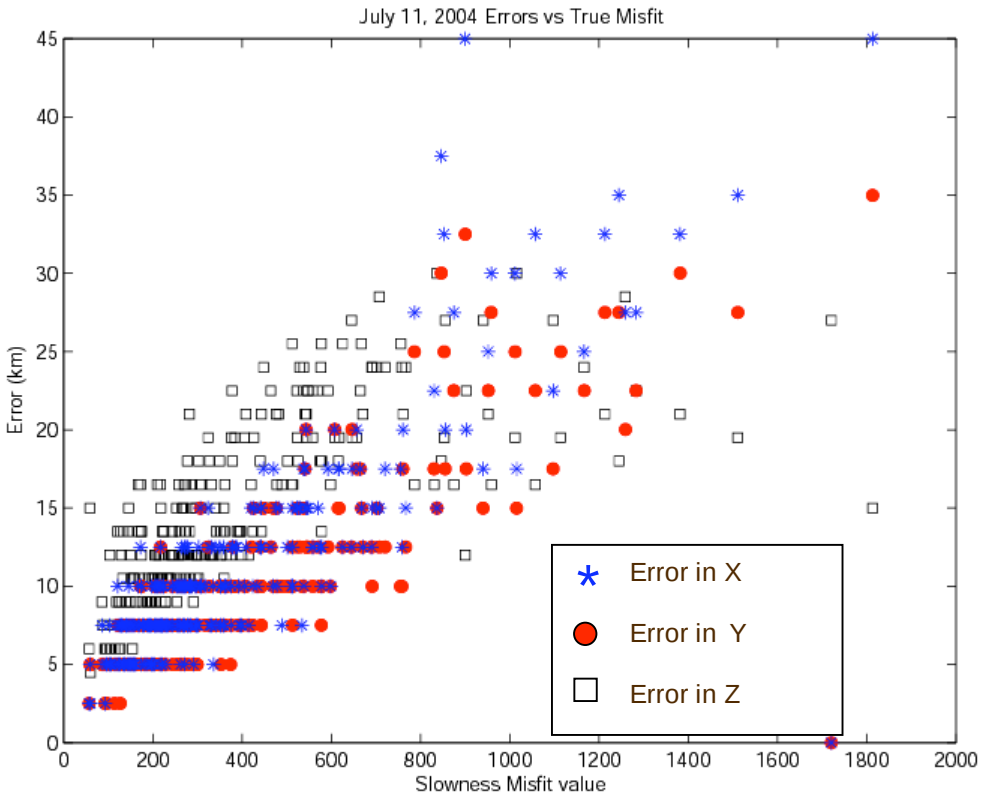

Figure 30 Location Uncertainty Versus Slowness Misfit. Plot of uncertainty in location determined from the 90% confidence region and the size of the misfit for that location. Errors in x are blue stars, errors in y are red circles and errors in z are white squares. Figure shows the increase in the location error as the misfit increases.

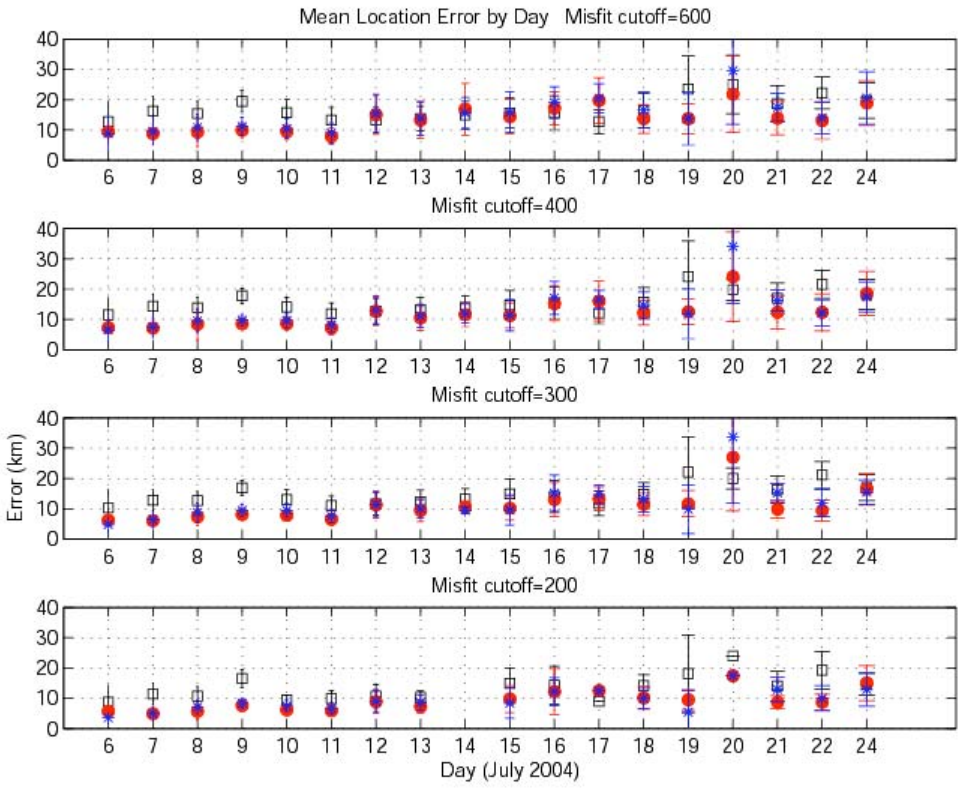

Figure 31 Plot of Mean Location Uncertainty July 6 – 24, 2004. Mean location error plotted by day for five-minute time windows with different values of misfit cut-off for the calculation of the mean. Horizontal axis is the day in July 2004; vertical axis is the error in kilometers.

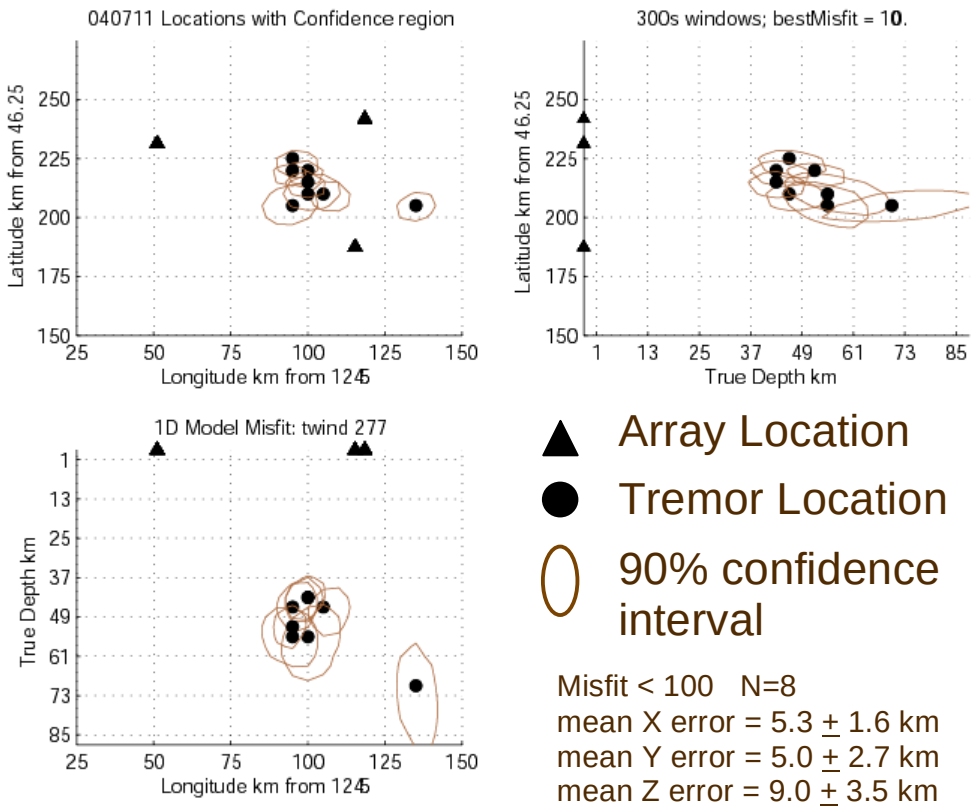

Figure 32 Best Locations for July 11, 2004. Locations for five-minute time windows are plotted on the X-Y, X-Z, and Y-Z planes with 90% confidence intervals drawn as brown ellipses for misfits less than 100. Mean errors listed are the average errors in the locations described by the 90% interval. Latitude is plotted as kilometers from 46.25 degrees North, and longitude is plotted in kilometers from 124.5 degrees West.

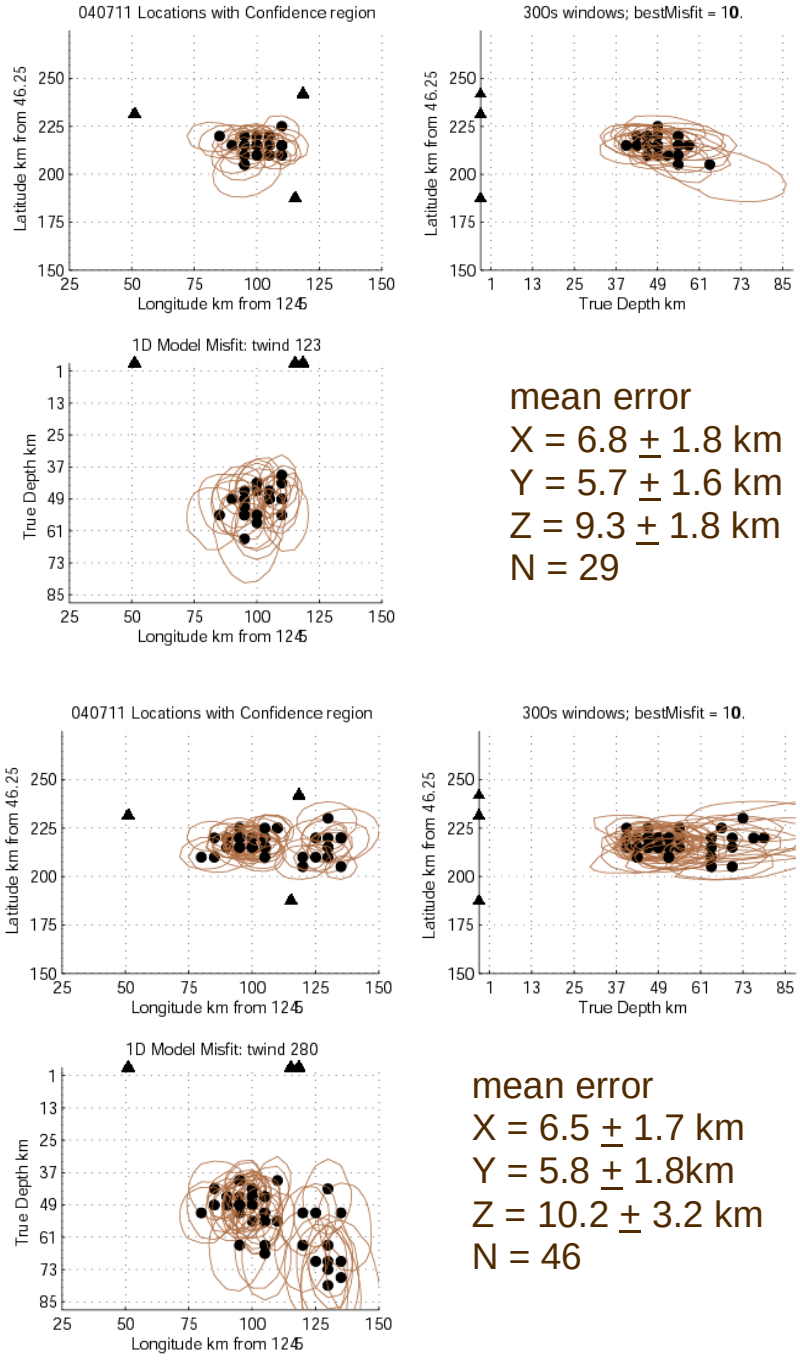

Figure 33 Locations on July 11, 2004. Locations for five-minute time windows from July 11, 2004 with misfits < 200. Top figure plots locations from the first 12 hours of the day. Bottom figure plots locations from the second 12 hours of the day. Two distinct clusters of locations are present in the second 12 hours.

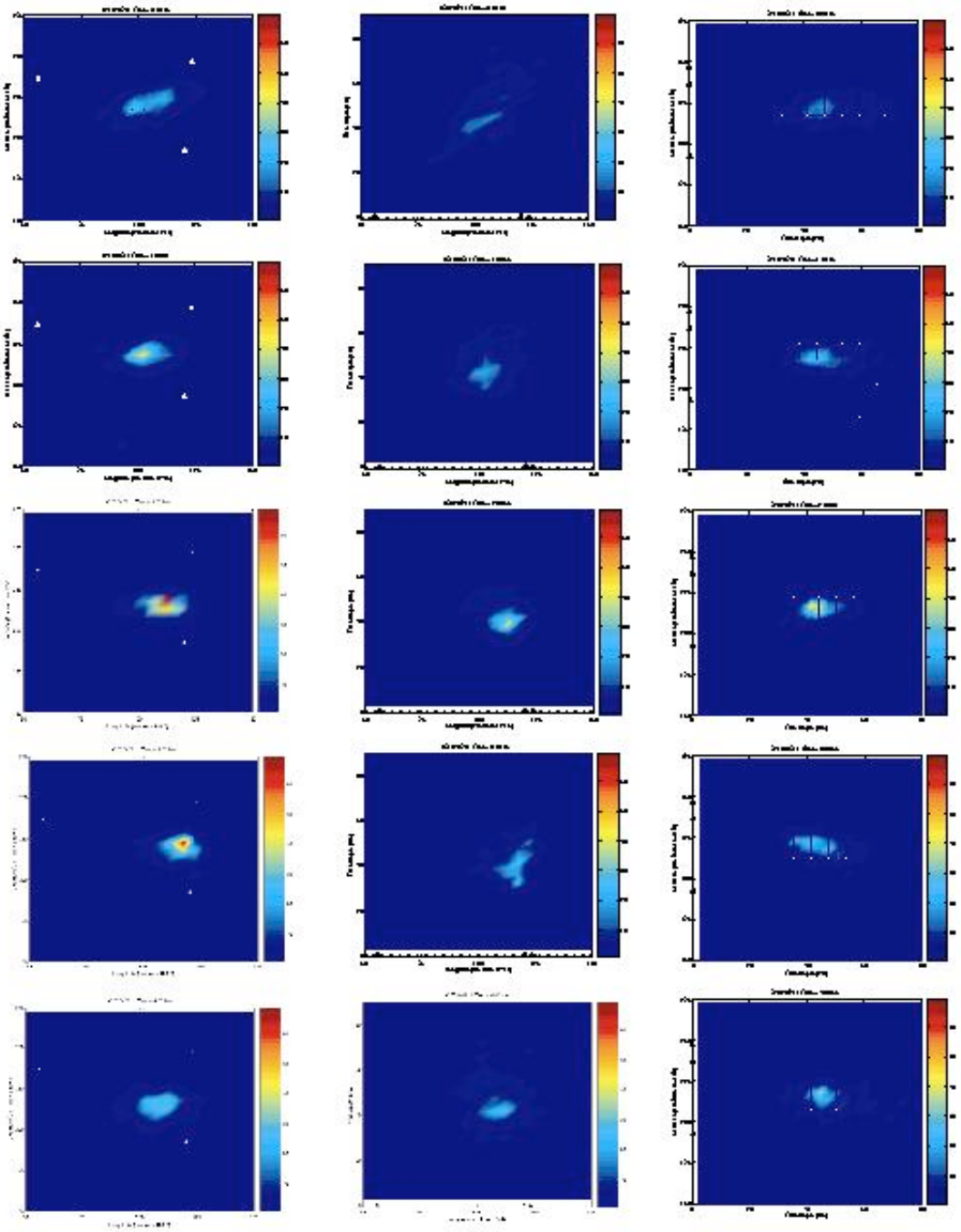

Figure 34 Filmstrip of Tremor Progression July 11, 2004. Filmstrip representation of changes in tremor over 5-hour period on July 11, 2004. First column is a 2D histogram of locations in the x-y plane. Next column is the 2D histogram projected in the x-z plane, and finally the last column is the y-z projection. Each plot represents one hour of data, 30 s windows with 18s overlap. Time increases from top to bottom.

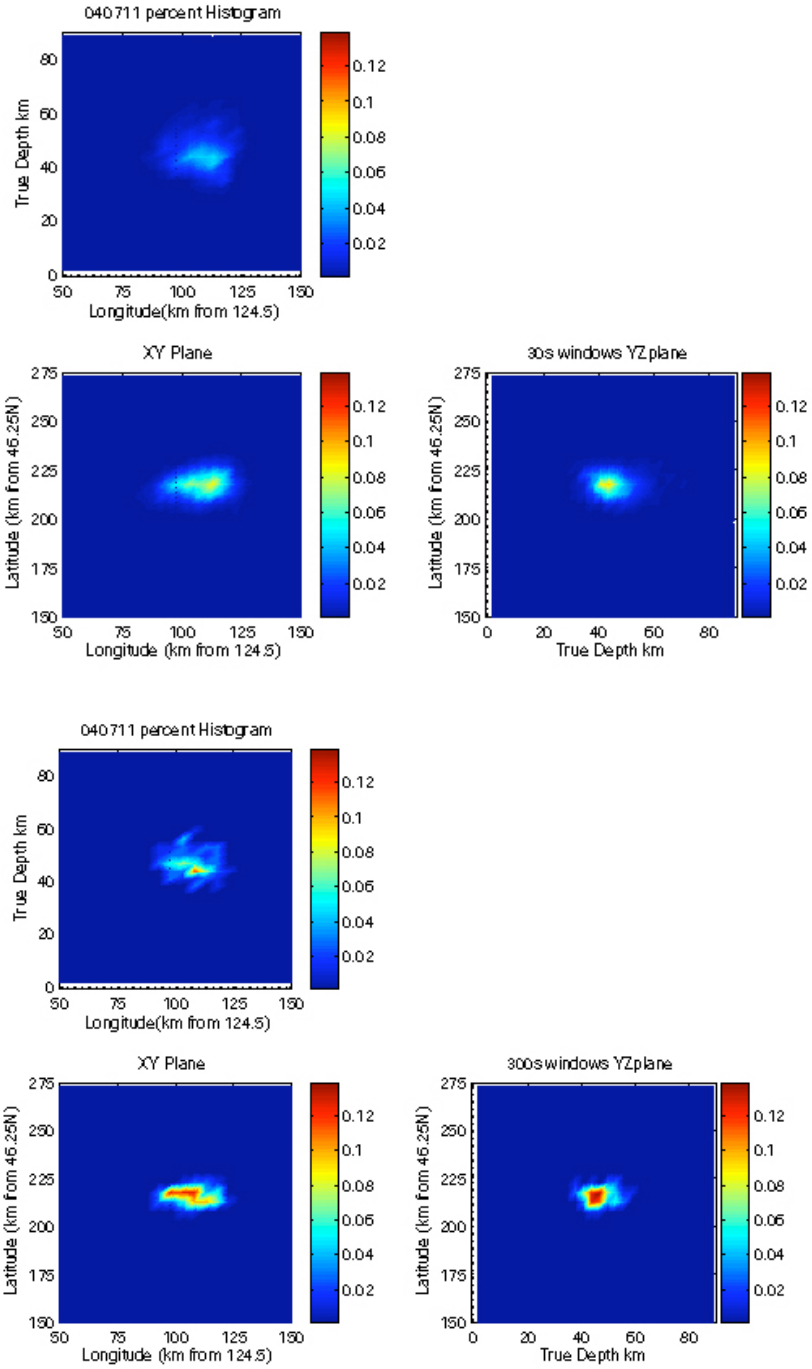

Figure 35. Locations for Non-Overlapping Windows Versus Overlapping Windows. Both plots are 2D histograms of the percentage of locations over a 6-hour time period that locate at a given location. Data is from the first 6 hours of July 11. Top figure is for 30s windows overlapping by 10s, and the bottom figure is for the non-overlapping five-minute windows. Locations for the two window sizes are very similar.

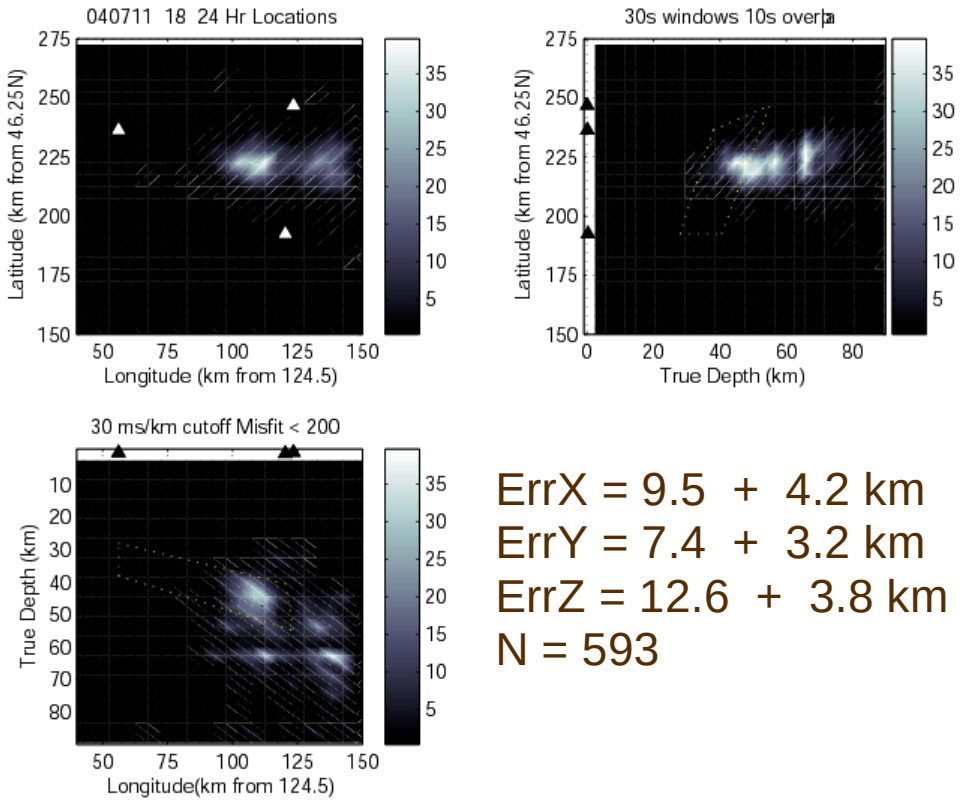

Figure 36 Two Tremor Regions for 30-s Time Windows. Thirty-second time window location, last 4 hours of July 11, 2004. Misfit cut off is less than 200. Same time window as some of the windows in Appendix 3. Two regions still evident in the figures. Average location errors for the four hours are from on the 90% confidence intervals of the misfit. Same two regions of tremor are evident as in Figure 4.10 for the five-minute time windows.

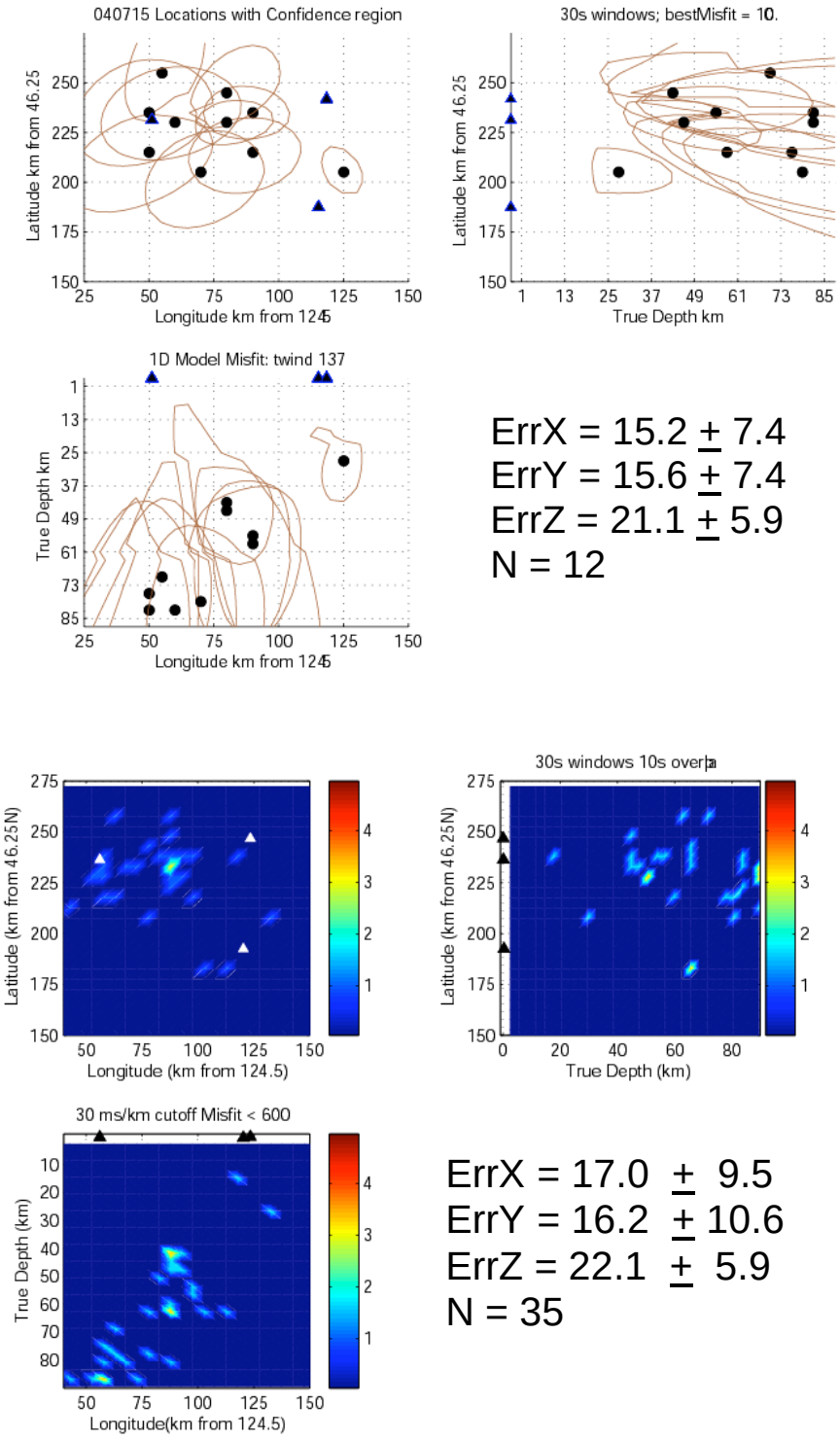

Figure 37 Multiple Source Regions July 15, 2004. Figure of locations showing time period with multiple source locations. Top figure shows location and confidence interval for misfits less than 100 for 2 hours on July 15, 2004. Bottom figure is a histogram of locations for the same time period, but a misfit cut off of 600. Average errors in the locations for each case are indicated.

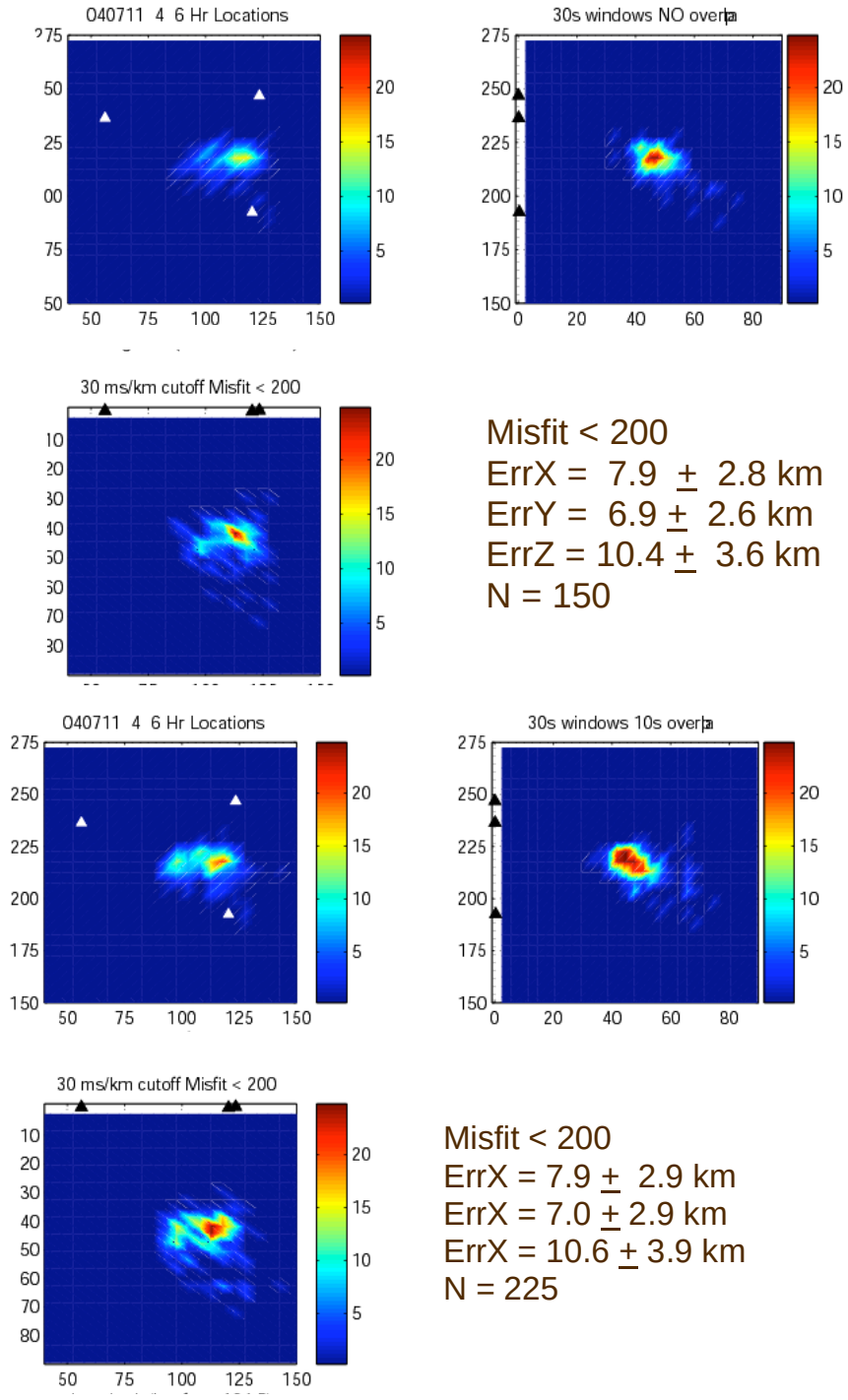

Figure 38 Overlapping Versus Non-Overlapping Windows. Figure showing difference between overlapping windows and non-overlapping windows. Locations for 4:00- 6:00 on July 11, 2004. Misfit cut off is 200, overlap is 10s. Top figure shows locations for non-overlapping windows, bottom figure shows locations for overlapping windows.

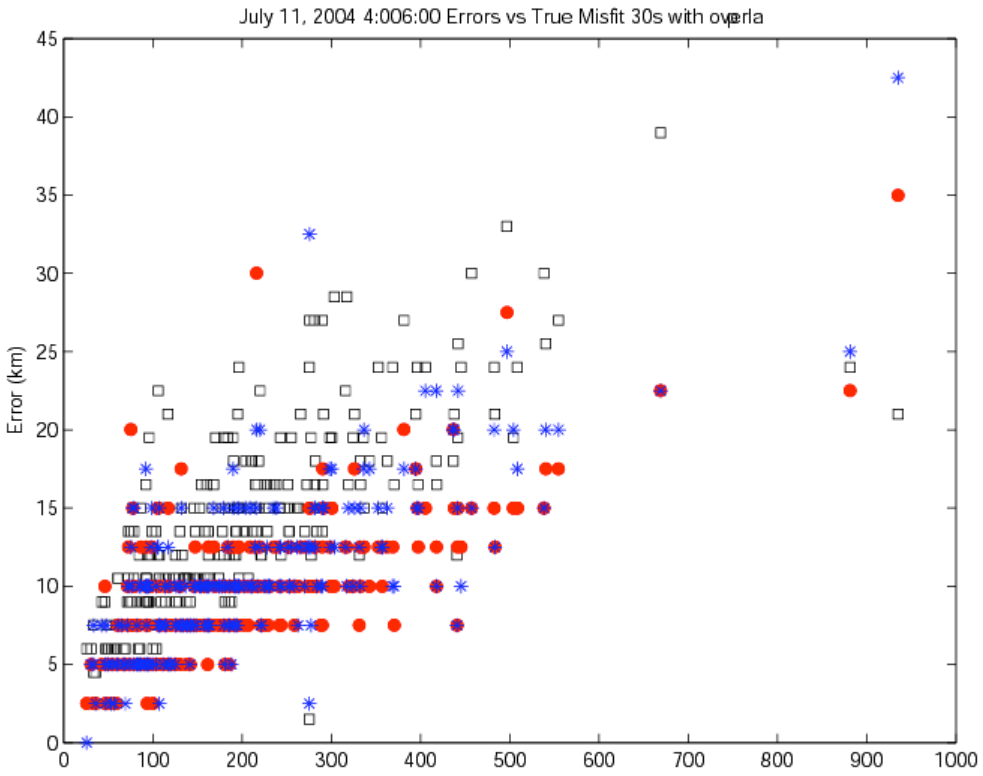

Figure 39 Location Error Versus Misfit: 30-s Time Windows. Plot of error in location determined from the 90% confidence region and the size of the misfit for that location. Errors in x are blue stars, errors in y are red circles and errors in z are white squares. Figure shows the increase in the location error as the misfit increases. Time windows were 30s with 10s overlap for 4:00 – 6:00 on July 11, 2004.

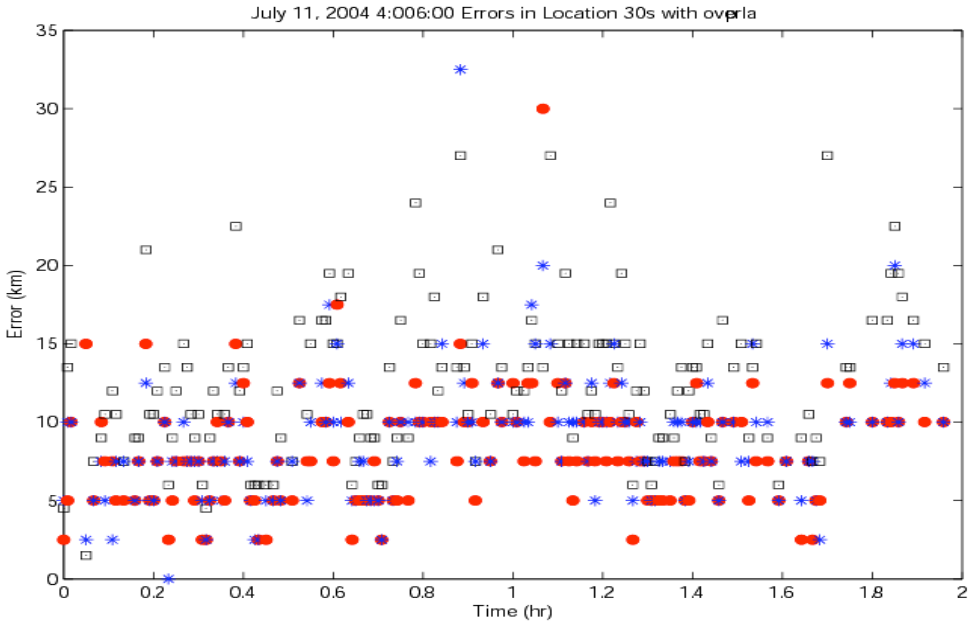

Figure 40 Location Errors for Two Hours, July 11, 2004. Location errors for 4:00-6:00 on July 11, 2004. Errors in x, and z are shown as blue stars, red circles and white squares, respectively. Time windows were 30s long with 10s overlap

.

Table 4 Percentage Tremor Occurrence. Percentage of five-minute and thirty-second time windows in which tremor occurred f. Each component and array was considered separately.

	Sooke	**Sequim**	**Lopez**
July 6 – 22, 2004 five- minute windows North	84.6	63.1	95.1
July 6 – 22, 2004 five- minute windows East	80.3	77.1	98.5
July 11, 2004, 0-6:00 30 s windows North	98.7	89.4	99.2
July 11, 2004, 0-6:00 30 s windows East	99.7	91.4	99.0
July 11, 2004, 20-24:00 30 s windows North	99.0	96.0	99.4
July 11, 2004, 20-24:00 30 s windows East	99.2	99.6	97.5

Table 5 Average mean and maximum value of inter-station cross-correlations for July 11, 2004.

040711	LOP E	LOP N	SEQ E	SEQ N	SOOK E	SOOK N
mean avg	0.6158	0.7082	0.4888	0.518	0.6267	0.6156
mean max	0.8154	0.8304	0.772	0.7416	0.8432	0.8421

Table 6 Location Uncertainties. Uncertainty in the locations for five-minute time windows for different misfit values. The number of events used in the calculation (locations that meet the misfit criterion) is indicated in the last column.

Misfit	X error (km)	Y error (km)	Z error (km)	N
< 100	5.0 +/- 3.4	6.4 +/- 3.4	10.1 +/- 4.6	62
< 200	7.7 +/- 3.8	7.6 +/- 3.7	11.8 +/- 5.0	342
< 400	10.9 +/- 5.2	10.2 +/- 5.1	14.5 +/- 5.4	1160
< 600	13.1 +/- 6.5	12.1 +/- 6.4	15.7 +/- 5.7	1811

CHAPTER 5:
Interpretation

The goals of this study were to better locate the tremor, to track the progression of tremor sources during an ETS event, and thus to better understand the source of the tremor and how it relates to the processes of subduction. In this section, I will comment on the results from both the network and small aperture seismic array studies. I will also offer and evaluate multiple working hypotheses for the tremor source, taking into account the tremor observations, GPS observations and other geochemical and geophysical observations found in Cascadia and other warm, young subduction zones. It is not yet possible to determine a definitive source for the tremor. However I can comment on which hypotheses are more or less plausible.

5.1 Comments on results from network and array studies

The signal characteristics of tremor on the regional network are similar to those reported in Japan (Obara, 2002). We also know that geodetically-measured slow slip events are concurrent with major tremor episodes. However there is also significant tremor activity during periods with no discernable GPS deformation (McCausland et al., 2005). These episodes fall outside the 14 $\pm$ 2 month ETS periods and last from hours to almost two weeks. Similar observations of tremor with no deformation have been made in the Nankai subduction zone where the geodetic signal is measured by borehole tiltmeters (Obara and Hirose, 2003). Average reduced displacements for tremor with and without a known slow slip event are similar (Table 1) indicating that the amplitude of the seismic signal is independent of whether a slip event occurs. However the epicentral region for the Cascadia tremor events without slip are smaller than those with slip. This suggests that if the tremor and slip always occur together then perhaps the slip patch is below the current resolution of regional GPS networks.

On the time scale of days and over great distances (hundreds of kilometers), the network-determined tremor epicenters are consistent with the progression of previously modeled slow slip events (e.g. Dragert et al, 2001). However on shorter time scales (minutes to hours), the source locations are more chaotic (Figure 6). In the first days of a tremor episode, tremor in areas 1 and 3 migrate bi-directionally from the point of initiation.

From the small aperture seismic array data we observe the same signal characteristics as with the network data. From the array data we observe that the migration of tremor hypocenters on a several day time scale is not smooth, but rather the hypocenters are localized to within 15 km horizontally and 20-40 km range in depth for several days, and then the active volume rapidly (within hours) shifts to a new position.

It is not clear from this study what it means to have the tremor source stable within a region over a period of hours to days and then shift to a new location. Does this behavior reflect a stable source of water over a period of hours to days that is heterogeneously distributed along the subduction zone? Does this behavior reflect a stable disturbance that facilitates the movement of fluids? Are these same volumes active for every tremor episode or are they different each episode?

The depth range observed with the arrays (30-70km) is not as large as with the network locations (12 – 60 km) (McCausland et al., 2005; Kao et al., 2006). The array result is probably an artifact of the phases used to calculate the modeled slowness, where the first arriving up-going (s) or down-going (S) direct S-waves was used to calculate the theoretical slowness vector at each array. No converted phases were considered e.g. (sS, pS, etc). This disfavors shallower sources by possibly making the shallow source slowness vector larger than what is observed, thus the minimum misfit solution at a greater depth could be favored over a shallow solution. The shallowest possible sources' epicenters locate at the center point between the three arrays.

Location solutions for the 1D velocity model have the smallest misfits and errors when there is a single tremor source active at one time and when the source region of the tremor (as defined by the locations within a 12 to 24 hour period) is confined to a single region (250 km^2 in epicenter and 20-40 km range in depth), and become almost impossible with the present methodology when multiple source regions are active. The presence of multiple active source regions can be seen in the network data, from beam-forming analysis on 2s time windows and in the 300s cross-correlated time windows (Figures 21 and 22). Therefore a more sophisticated methodology needs to be developed to track the tremor when it resolves into simultaneous multiple source regions near the arrays.

Location solutions using the 3D velocity model have similar epicentral locations as for the1D solutions. The 3D velocity model should give more accurate locations, however the location depths rarely converge on a solution within the model space, and most often locate at the base of the model. For these reasons, the use of the 3D model was abandoned because the depth problem could not be resolved.

5.2 Discussion of source hypotheses

Other seismic, geophysical and geochemical observations involving the presence of fluids at depth are important to this discussion. Seismic observations include the signal characteristics: low frequency content, emergent onset, long durations, small amplitude and dominance of the waveform by S-waves (Obara, 2002; McCausland et al., 2005; Kao et al, 2006). The seismic observations also include spatial and temporal characteristics: frequent concurrence with cyclic geodetically measured slow slip events (Rogers and Dragert, 2003), migration of tremor epicenters on several day times scales (Obara, 2002; Rogers and Dragert, 2003; McCausland et al., 2005; Kao et al, 2006), large depth distribution of locations (12 – 70 km) (McCausland et al, 2005; Kao et al, 2006), persistence of tremor

within a localized volume on the time scale of hours, presence of multiple active source regions in both short (2s) and long time windows (300s), and independence of size of average reduced displacements for a given episode from measured geodetic slip (McCausland et al., 2005).

To help with the interpretation of the seismic data there are a variety of geochemical and geophysical studies that help provide constraints on the nature of the tremor source. Geochemical studies indicate that fluids are released from the subducting crust and sediments in the region where tremor and slow slip are observed (e.g. Peacock, 1993; Hyndman and Peacock, 2003) (Figures 41 and 42). These same geochemical studies also indicate that the introduction of fluids to the overlying mantle in this region is likely fracture-controlled and interacts with the mantle peridotite to form serpentinite, reducing the density and seismic velocities and increasing Poisson's ratio of the overlying mantle (Hyndman and Peacock, 2003; Christensen, 2004; Evans, 2004). These material changes are corroborated in Cascadia by seismic studies (e.g. Bostock et al., 2002; Brocher et al., 2003; Nicholson et al, 2005) that indicate anomalous shear wave velocities in the overlying mantle (Figure 43). Magnetotelluric studies in Japan (Seno et al, 2001, Matsumoto et al, 2003; Umeda et al, 2006) and Cascadia (Kurtz et al, 1986; Soyer and Unsworth, 2006) show conductivity anomalies in the lower crust above the subducting slab. In Cascadia the anomaly is located at approximately 20 km beneath Vancouver Island (Soyer and Unsworth, 2006). In both Japan and Cascadia, the anomaly is interpreted as resulting from the presence of interconnected fluids (Figure 44).

A suite of plausible models for tremor fall into two basic categories: sources that invoke many, overlapping, small earthquakes either along the subduction interface or distributed in a volume, or continuous sources related to the presence or migration of fluids at depth. In the following paragraphs I

explore the pros and cons of five generic models and summarize contributions to each of the relevant observations in Table 7.

The first model (Model 1) is that the tremor is a series of small earthquakes along the subduction interface or in a zone parallel to and near the interface whose signals interfere in such a way as to produce tremor-like signals (Rogers and Dragert, 2003). These earthquakes could represent the release of seismic energy in the transition zone (between stick-slip and stable sliding behavior) Thus these earthquakes could represent the rupture front of the slow slip event. Key supporting observations for this model include the coincidence of tremor with slow slip events, the slow migration of tremor epicenters roughly coincident with the slow slip events, the long duration and emergent onset of the signals and the presence of P- and S-wave pairs in the signals (La Rocca et al, 2005). Not supporting this model is the band-limited and low (1-6 Hz) frequency content of the tremor, which is unlike earthquake spectra (regional earthquakes of similar depth have a tectonic earthquake spectrum). However if low-stress drop earthquakes comprising tremor occur in a low-strength plastic material with a very low shear modulus, then we could expect a low frequency content for the events (e.g. Kamaya et al., 2005; Ito and Obara, 2006a; Ito and Obara, 2006b). The tremor locations cover a larger depth range than this model would predict, both above and below the subducting plate interface.

The second model (Model 2) is that the tremor is a volume-distributed series of low-stress drop earthquakes that result from the presence of confined fluids throughout a volume above the slab. Increases in fluid pore pressure decrease effective normal stress on a distributed set of faults allowing for strain energy release at low shear stresses (examples from other tectonic settings include e.g. Linde et al, 1994; Vidale and Shearer, 2006; Segall et al, 2006). In this model these earthquakes are distributed over a volume and need not be limited to near the slab interface. This model can explain the concurrence of tremor and slow slip events because the occurrence of the

slow slip event changes the stress in the surrounding material, which in turn increases pore pressure and allows localized low stress drop earthquakes. This model also can explain the duration and emergent nature of the tremor signals. As with Model 1, Model 2 cannot explain the limited frequency content of the tremor signals unless we consider the source volume to occur in a low-strength plastic material with a very low shear modulus.

The third model (Model 3) is that the addition of fluids to the mantle wedge results in the serpentinization of mantle peridotite, a transition that is accompanied by a significant volume increase (e.g. Fryer and Mottl, 1997; Hopkinson et al., 2004; Evans, 2004). This localized inhomogeneous volume change would cause anomalous micro-earthquake producing stresses in the surrounding material. Slow slip events could modulate the stress changes in this volume and trigger the tremor sequences. The ability of serpentine to move on time scales relevant to ETS events is supported by the geologic evidence of intrusive movement of serpentine at the Marianas Trench where there are serpentine mud volcanoes extruded at the surface near the trench (Fryer and Mottl, 1997) and at the Lost City at the Mid-Atlantic Ridge where there are off-axis serpentine volcanoes (e.g. Kelley et al, 2001). This model agrees with most of the observations including the signal characteristics, the distribution of locations, the concurrence with slow slip events, the migration of sources on the time scale of several days, and the persistence of the source volume on the scale of hours. The observation that does not agree with this model is the frequency content of the signals, unless we consider the source volume to occur in a low-strength plastic material with a very low shear modulus.

Field evidence of exhumed serpentinites (e.g. Keleman, et al.,1995; Hopkinson et al., 2004; Evans, 2004) suggests that the volume change as peridotite is serpentinized causes outcrop-scale radial fracturing in the surrounding the material being serpentinized (O'Hanley, 1992; Evans, 2004). This fracturing not only causes low stress drop earthquakes but also develops

fractures that could transport fluids (see Model 4). The region that has been serpentinized is a mechanically weaker zone than the surrounding material (Guillot et al., 2000; Guillot et al, 2001; Hopkinson et al., 2004) and therefore could also be where slip is occurring (as in Model 2, but here with or without increased fluid pore pressure).

The fourth model (Model 4) is that the tremor results from the migration of fluids released from the down-going plate by dehydration reactions. These fluids migrate buoyantly through the overlying mantle and lower crust (Peacock, 1993). Field evidence shows that fluid movement and serpentinization in the mantle is likely fracture controlled (Evans, 2004). Minor stress changes resulting from slow slip events could accelerate fluid movement producing more hours of and longer lasting episodes of tremor during the slow slip events. The fluids must find some path into the mantle, lower crust and even to the surface. Fluids rich in high $^{3}He/^{4}He$ ratios (indicative of a mantle origin) are found in surface hot springs in the Kii Peninsula, Japan (Seno et al, 2001, Matsumoto et al, 2003; Umeda et al, 2006) and at Hotsprings Cove on Vancouver Island, BC (Clark and Phillips, 2000). In addition, gaseous methane is discharged with the geothermal fluids at Hotsprings Cove indicating a deep crustal source (Clark and Phillips, 2000). Further supporting the presence of fluids and an interconnected fracture system over a large depth range is a region of high conductivity in the lower crust in the Kii Peninsula, Japan (Umeda et al, 2006) and at approximately 20 km depth under Vancouver Island in Cascadia (Kurtz et al, 1986, Soyer and Unsworth, 2006). The signal character of non-volcanic tremor is similar to volcanic tremor generated by the movement of fluids (Julian, 1994; Chouet, 1996), so perhaps it is not unreasonable to find an analogy to this model in the subduction system. All current observations are consistent with this model.

The fifth model (Model 5) is that the tremor represents the intrusive ascent of serpentine into the mantle wedge, lower crust, or along the plate interface. The fluids released from the down-going slab react with the

overlying mantle to produce serpentine (Peacock, 1993; Hyndman and Peacock). This serpentine is less dense than mantle peridotite and would migrate buoyantly toward the surface. The tremor could then be the seismic manifestation of the stress change induced by the intrusive movements of the serpentine. Observations that support this model include the coincidence with slow slip events (whereby the movement of the serpentine could be facilitated by stress changes resulting from the slow earthquake), the emergent nature and long durations of the tremor signals, and the depth distribution of the tremor. However the ascent of the serpentine would have to be fast enough to generate seismic signals, and there must exist serpentine bodies at a variety of depths and all along the sections of the subduction zone where we see tremor.

Finally I cannot eliminate the possibility that more than one source is contributing to the seismic signals we describe as non-volcanic tremor. Low frequency earthquakes can sometimes be found embedded within the tremor signals in Japan (Shelly et al, 2006) and in Cascadia (La Rocca et al, 2005; M. La Rocca pers. commun. Sept., 2006). Depths of the Japanese low frequency earthquakes are well-constrained because of the identification of P- and S-wave pairs and these events locate several kilometers above the subducting plate interface. Yet we have tremor without clear P- and S-waves pairs and tremor with locations greatly different from the location of the subducting slab (McCausland et al, 2005; Kao et al, 2006; and Figure 29). Thus a combination of Model 2 and Model 4 would allow for low stress drop earthquakes along or parallel to the plate interface possibly indicating a direct seismic manifestation of the slow slip event, and it would allow for the movement of fluids throughout the volume affected by stress changes resulting from the slow slip event. This combination would explain the coincidence of the tremor with the slow slip events providing the stress changes needed to cause the seismic signals, as well as the remaining observations of the tremor.

Models 2 and 4 have the fewest contradictions with observational data. Models 1, 3, and 5 have more contradictions, though none of the contradictions are fatal if we allow combinations of sources. The tremor and slip must be related to the presence of fluids at depth and whether the presence of fluids cause the tremor and slow slip or just facilitate their occurrence under the correct stress conditions is not yet clear. Further data relating the exact timing of the initiation of the tremor and slip events is required to understand which occurs first and if they always accompany one another. For instance the Plate Boundary Observatory borehole strain meters can resolve slow events on shorter time scales than GPS. Using the co-located borehole seismometers, which have better signal-to-noise than surface stations, one might be able to discern the timing of the initiation of slow slip event and tremor. In addition, the borehole seismometers might also allow for the better detection and quantification of wave types such as P-waves or other phases that would be used to further develop and distinguish between the source models.

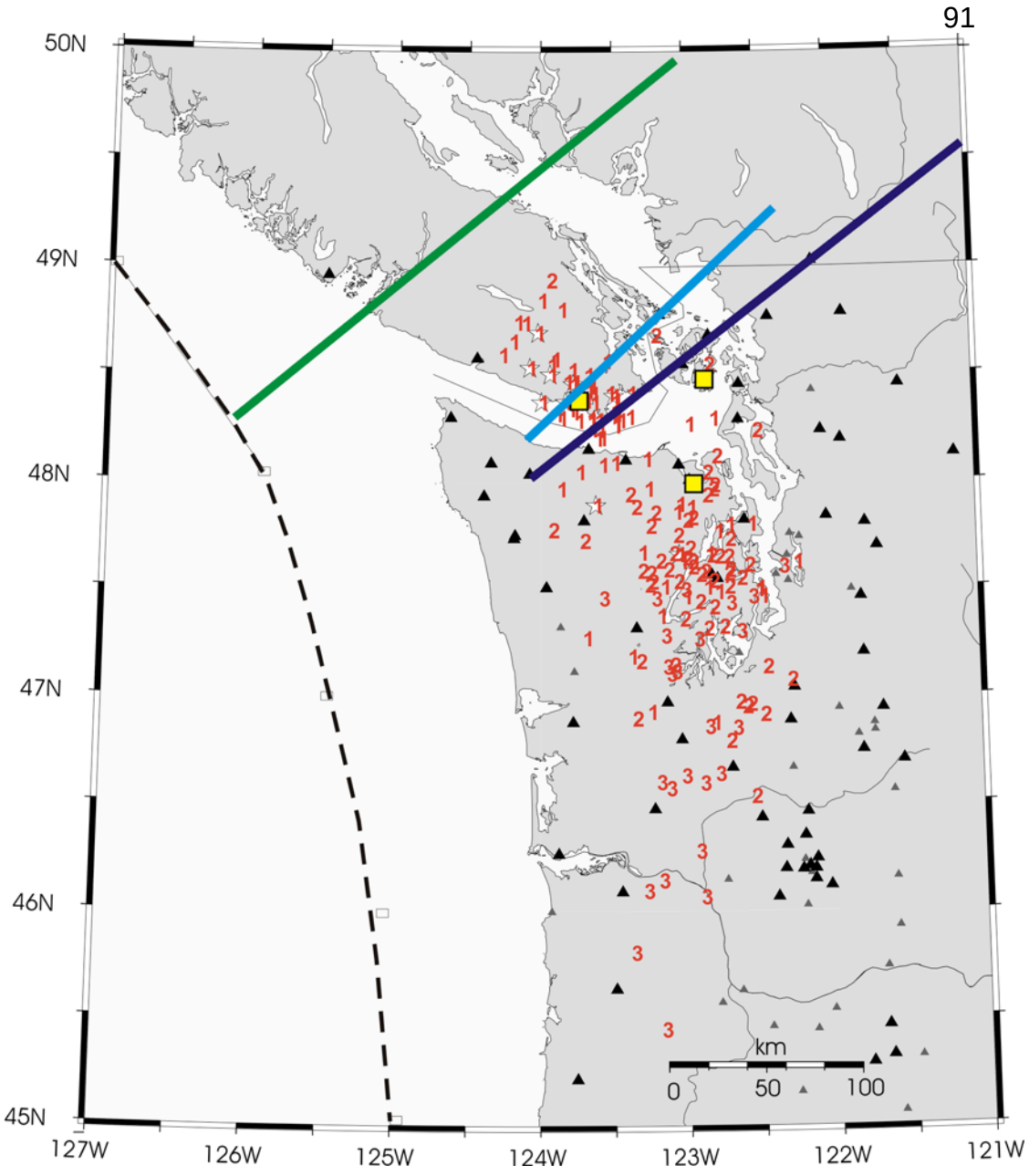

Figure 41 Index Map. Index map for Figures to follow. Tremor locations are indicated by red area numbers (like Figure 5), PNSN and PGC network stations indicated by grey and black triangles, array locations are indicated by yellow squares, and the approximate location of the trench (from Hyndman and Wang, 1995) is indicated by the black dashed line. Location of the cross-section in Figure 5.2 indicated by the green line, the location of the cross-section from Figure 5.3 is indicated by the dark purple line, and the location of the cross-section for Figure 5.4 is indicated by the blue line. Array locations have been projected perpendicularly onto the cross-sections.

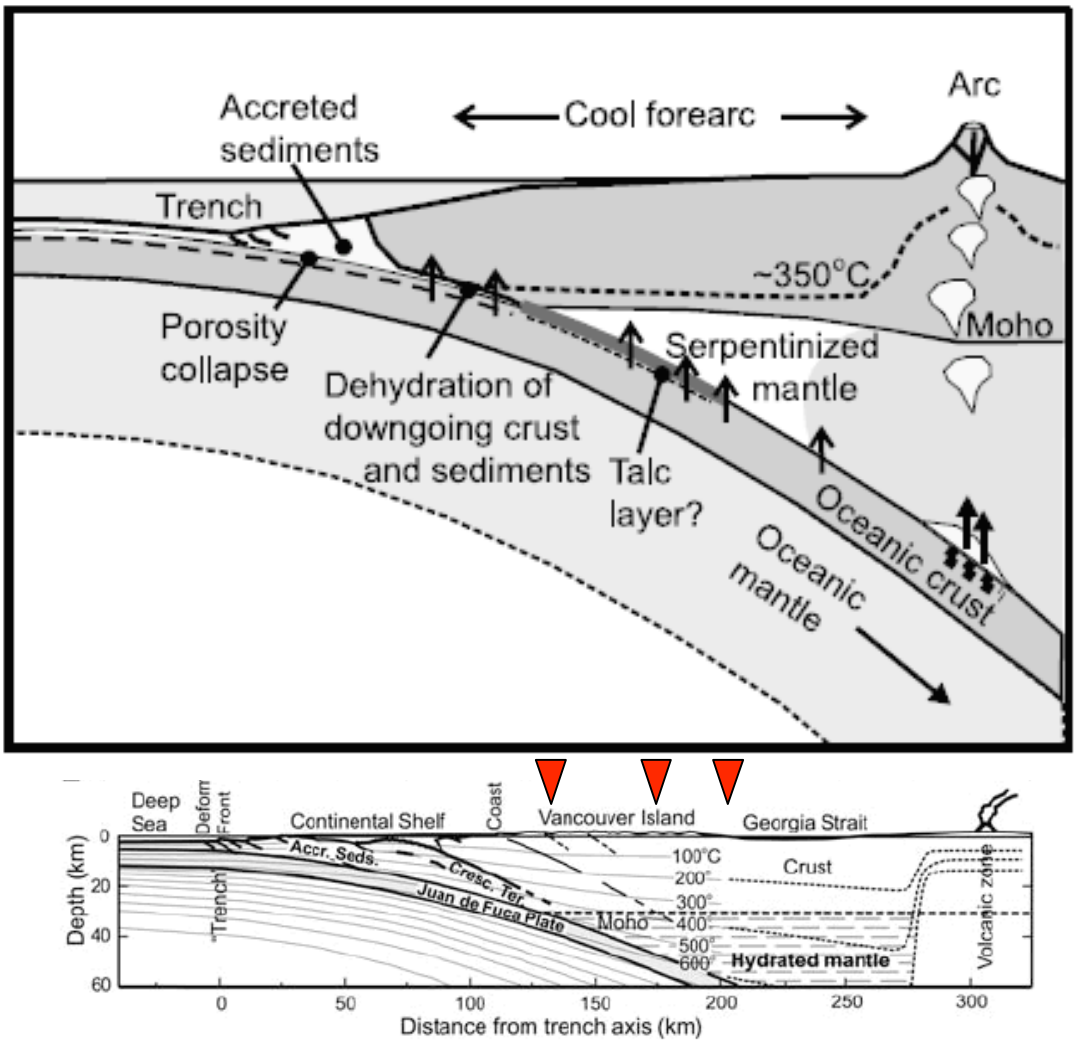

Figure 42 Heat Flow and Schematic Cross-Section of Subduction Zone. Schematic cross-section showing where fluids are being released in the subduction process and cross section from the trench to the volcanic arc with modeled temperature contours and interpreted structure (modified from Hyndman and Peacock, 2003). Red triangles indicate the locations of our seismic array as projected onto the profile, these arrays lie above a region where fluid is being released from the subducting slab and the western most edge of the hydrated and locally serpentinized mantle wedge.

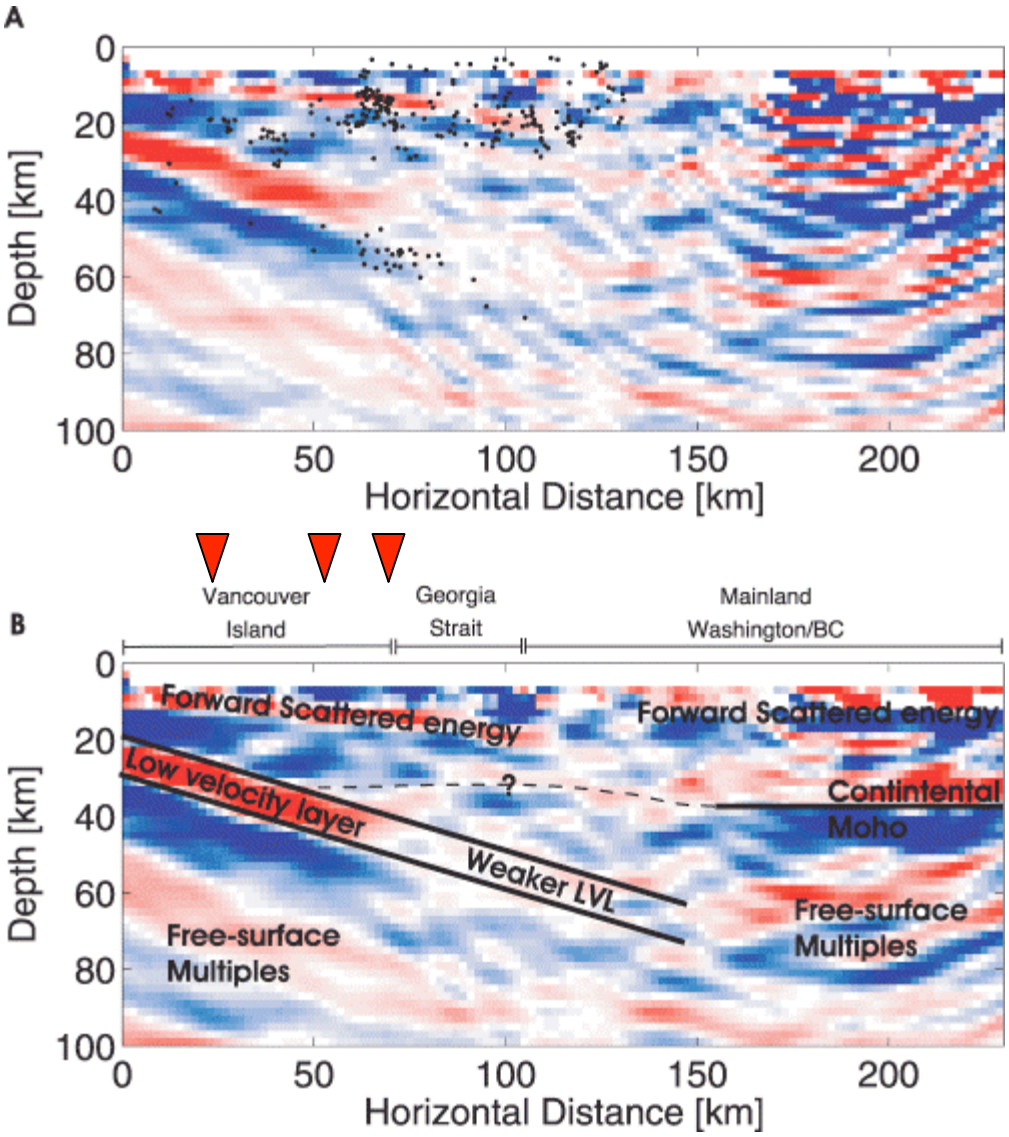

Figure 43 Shear-Wave Velocity Anomaly Cross-Section. Teleseismic migration image showing shear wave velocity perturbations along a profile oriented perpendicular to the trench in Northern Cascadia. Blue areas indicate high S-velocities and red areas indicate low S-velocities. Circles indicate are hypocenters of earthquakes. Image b is a lower-frequency version of the top figure (Figure from Nicholson et al, 2005 including interpretation). Red triangles indicate the location of the arrays as projected onto the profile. In this model the arrays lie above a region where the sediments are de-watering and above the western edge of the velocity anomaly associated with a serpentinized mantle wedge.

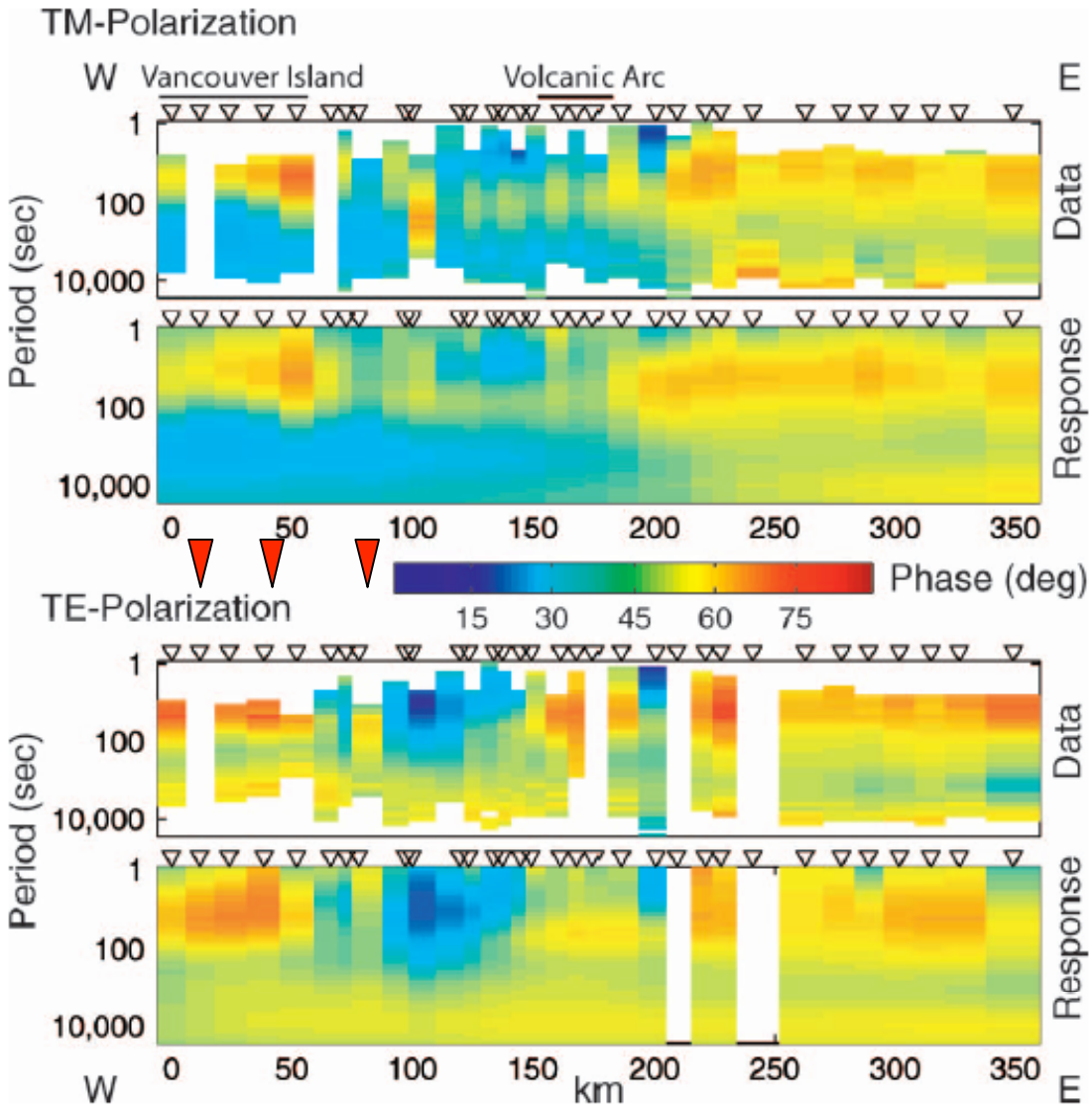

Figure 44 Magnetotelluric Cross-Section. Magnetotelluric data and model results from Northern Cascadia. Profile is oriented perpendicular to the trench showing a high conductivity anomaly at approximately 20 km depth beneath Vancouver Island both along and perpendicular to strike. Phases > 45 degrees indicate a high conductivity anomaly (figure modified from Soyer and Unsworth, 2006). Red triangles indicate the location of the arrays as projected onto the profile. The arrays lie above the region with the conductivity anomaly associated with a region of interconnected fluids.

Table 7 Summary of Models and Observations

Observations	Model 1:Chattering of slow slip on slab interface	Model 2: increase in fluid pressure which leads to a series of low-stress-drop earthquakes	Model 3: Volume expansion – transition of mantle peridotite to serpentinite	Model 4: Seismogenic movement of fluid	Model 5: Intrusive ascent of serpentine
Emergent onset	+	+	+	*	+
Duration of tremor (minutes to hours)	+	+	+	*	+
Frequency content dominated by 1-6 Hz	?	+	+	*	?
Signals dominated by S-waves	+	?	?	*	?
Tremor strongly associated with GPS-measured slow slip events	*	*	+	+	+
Tremor occurs over large depth range (12-70km)	x	+	*	*	+
Epicenters migrate on timescale of several days	*	*	+	+	+
Source region in hourly timescale is consistent to within 250 km2	+	*	+	+	*
Tremor moves laterally as well as vertically	?	*	*	*	?
Multiple sources can be active in a given time window (at 2s to 300s time scales)	?	+	*	+	+
* strongly favors + suggestive ? creates doubt x fatal objection					

CHAPTER 6

In any experiment it is important to consider what further tests and computations could improve the results. In this chapter I will discuss tests that could be applied to this or other small aperture array data and other ways of analyzing the data that would improve the results and error estimates.

A simple change that could improve the slowness estimates and therefore the locations would be to ensure that velocity changes did not happen at or near grid nodes in the model; because the path that the rays take in the computed slowness grid are sensitive to large changes in the velocity structure near the source. Another change that might improve the solution would be to re-interpolate the slowness grid near the source location, then recalculate the location. This could improve the value of the misfit for locations that are not on the grid nodes, and therefore improve the confidence in the location. Finally we used a simple constant ratio between Vp and Vs to determine the regional shear-wave velocity model. In places where there is a good understanding of the Vp/Vs ratio, a more sophisticated shear-wave velocity model could be generated. To date there is no comprehensive shear-wave velocity model for the Cascadia region.

6.1 The effect of unknown velocity structure on the data

Changes in the horizontal and vertical velocity structure can greatly change the direction and path that a ray travels. Therefore it would be prudent to have a better understanding of the effect of unknown velocity structure on the data. We only measure what happens at the surface, thus we can never precisely know the true ray path, but we can run tests to see how changes in the velocity structure would affect the theoretical slowness and therefore the locations.

The first structural effect to consider is that I used a 1D velocity model to locate the tremor. To first order, the 1D velocity structure is a good

approximation. However, we know that there is a dipping sharp velocity contrast (subducting slab and Moho) beneath the study region (e.g. Bostock et al., 2002). In addition the continental Moho is not imaged in this part of the forearc region (e.g. Bostock et al., 2002). The sharp velocity contrast (continental Moho) disappears to the east of our arrays, and beneath our arrays there is a dipping velocity contrast (subducting slab and slab Moho). Not accounting for the dipping velocity contrast will bias the locations; they will locate deeper and laterally further down-dip than the true locations. Where the Moho disappears, the velocity does not change as quickly. Having a greater velocity contrast than truly exists will increase the curvature of the ray, making the source appear closer to the array. Having a greater velocity contrast will decrease the travel time, making the source appear shallower.

A second complication is lateral velocity variations in the crust. There exists a high velocity anomaly at the south end of Vancouver Island (Ramachadran et al., 2005). By not accounting for the presence of the higher velocities in our velocity model, the magnitude of the slowness will be overestimated, and a source will appear further from the array or shallower. The opposite is true under the Olympic Mountains, where there exists a low velocity anomaly. While this region is at the southern end of our model and outside the region between the three arrays, it could still lead to an underestimation of the slowness for sources coming from the south, and would make a source appear closer to the array or deeper than the true location.

In order to gain a better understanding of how the choice of velocity structure will affect the data, synthetic tests could be run in a place where the 3D velocity structure is well known (for instance Crosson, 2004; Preston and Creager, 2003). One could compare the slowness vectors calculated for waves through a realistic 3-D structure to those through an equivalent 1-D structure. A statistical analysis could then be made of the errors in the locations as well as for the difference between the slowness calculated for the 1D and 3D velocity models.

3-D velocity structure may effect the back projection of plane waves more than it does absolute travel times thus developing a technique for including travel times, while beyond the scope of the current study could provide considerable improvement in mitigating the problems dealing with complex structure. In the following section I outline a strategy for developing such improvements in the future.

6.2 Inclusion of travel time information

One way to improve the locations of the tremor would be to include travel-time information in the source location procedure. The inclusion of another set of parameters, the relative arrival time at each array, would further constrain our array-determined locations. This procedure was used in our array analysis of regional earthquakes (La Rocca et. al. 2006, in preparation). The results indicated that the array-determined locations that utilized travel-time information as well as S-phase slowness were much closer to the network determined locations (within one kilometer for events near the arrays) than those locations that only used the slowness of the S-phase (errors in x and z are 10km and 5km, respectively). While our estimates of relative arrival times for non-impulsive tremor signals will be less precise than for impulsive signals, we can still expect improvement in the error estimates on our tremor locations. Because one cannot identify individual phases at each array, one could use the relative arrival time of energy pulses that can be identified at all three arrays.

To obtain relative arrival times at each array, one could combine the method using network data (Chapter 1), in which the signal envelopes would be cross-correlated between arrays, with the previously described array location procedure (Chapter 3). For each time window, the relative time delays at each array station would be determined through cross-correlation. Then for each component at each array, the seismogram at each station would be stacked using the appropriate relative delay times. This would greatly increase

the signal-to-noise ratio of the resulting stacked seismogram. Then the envelope of the stacked seismogram would be calculated (as described in Chapter 1). Next the envelopes of the three components would be stacked to produce one envelope for each array. This stacked envelope then describes an average at each array. Finally the three envelopes would then be cross-correlated to find the relative arrival times of energy bursts at the array within the given time window at each array. The relative arrival times would then be used in the location procedure by comparing them to theoretically determined values in the Misfit calculation (Equation 11, Chapter 3).

This procedure could be repeated iteratively, in which a new time window is defined for each array based on the relative arrival times (at the arrays). These windows would then be cross-correlated to find new relative inter-station delay times. The seismograms would once again be stacked, envelopes calculated for each component, and then the component envelopes stacked, and so on. This could refine the results such that the same burst is being considered in the time window at each array.

A potential drawback to the use of the relative arrival time information is that the addition of parameters may make a solution impossible for more of the time windows throughout the episode. Another drawback is that this technique requires energy bursts or variations that can be tracked between arrays, limiting the number of windows that could be analyzed. This might make tracking the tremor from time window to time window impossible for large time periods.

6.3 Better understanding of error in locations

6.3.1 Jack-knife tests

In addition to the calculated statistical uncertainties, theoretical uncertainties of the array geometry, and uncertainties determined from the application of our methods to earthquakes, all covered in the analysis chapter (Chapter 3), there are other ways that the uncertainties in our locations could

be investigated. Jack-knife tests could be performed on the inversion for the slowness vectors. During a time period with the strongest tremor signals located between the three arrays, individual stations or pairs of stations could be randomly removed from the slowness calculation at each array. This would produce a large number of combinations to be tested, as each of these slownesses would then be used to calculate a location. Statistical analyses could then be performed on the changes in the locations as different stations were removed.

An alternative, which would involving fewer calculations, would be to perform Jack-knife tests on the location procedure. Different pairs of components at each array could be removed, such that each array used only one estimate of the slowness in x and the slowness in y. Remember that in the present inversion there are two estimates of slowness in x and y, from the north components of data and from the east components. Statistical analyses of the differences in locations over many time windows could give a good indication of the stability and quality of the locations and provide estimates of the errors in the calculated slowness.

6.3.2 Forward modeling

Another way to quantify the error in the locations would be to use forward modeling to generate synthetic waveform data, with added random noise, for each array for a known source location. The waveform would be propagated to the arrays through a velocity model. Then for each array, the synthetic waveform data would be processed in the same way as the tremor data, cross-correlating for relative arrival times and inverting for the slowness vectors. Then the calculated slowness at each array would be used to locate the synthetic waveform data. The calculated location would be compared to the true location of the synthetic source. This process would be repeated for all locations in the model grid space, for various levels of random noise, and for different velocity models.

The sensitivity of the model could be investigated in another way. Synthetic waveform data could be propagated through a velocity model, then located using array processing techniques. Then one could modify the velocity model, and regenerate the synthetic waveform data at the array locations. Then the event would relocated using the original velocity model. This could be repeated for a variety of velocity models and would show how various differences between the true velocity model and the assumed velocity model affect the locations.

6.4 Differences in calculated slowness between station components

One complication that begs further consideration is when the computed slowness and back-azimuth do not agree when computed on different components (N and E) on the same stations, and the difference in the computed values is greater than the known errors (Figures 11 and 19). This occurs at both the Sooke and Sequim arrays, but not at the Lopez array. Because we never see this effect at Lopez, and because it does not always occur at Sequim and Sooke, we can be reasonably certain that it is not an artifact of our processing techniques, of the station installations or local site effects. For the same reasons, I do not believe that we have incorrectly characterized the errors in the computed back-azimuth and slowness. Thus we need to consider other reasons for the discrepancy.

If we consider any seismic source, it will have a non-uniform radiation pattern for both the P- and S-waves, where the wave amplitudes will be stronger and weaker. Two simultaneous sources located at different places can dominate the signal of different components at an array. So each component is recording a different and real source, and therefore yields a different source direction and slowness. To investigate this further, one could use beam-forming to ascertain the directions and slownesses for all the sources in a given time window, and compare them to the results of the inverted slowness and back-azimuth for the north and east components. If

there is more than one source in the time window, separate inversions for the different source locations could be performed using the different slowness and back-azimuth values.

The extent of this effect and the ability of each array to discriminate sources could be investigated by generating simultaneous synthetic earthquakes at various locations. Array analysis could then be performed on the resulting combined synthetic seismograms to see what combinations of source locations are distinguishable, and how far apart the sources would have to be to be distinguishable.

During time windows when there is only one source active, it is possible that the location of the source is such that one component is close to or along a nodal plane for a shear-wave radiation pattern and the other component is close to or along a plane of maximum shear-wave amplitude for a double-couple radiation pattern. In this case, one component would be dominated by noise and the other component would be dominated by the tremor signal. To investigate this further, one could compare the back-azimuth computed on each component with the dominant polarization direction to determine which component is close to the polarization direction. One could then either use the component closest to the polarization direction or weight the two back-azimuths proportional to their projection on the polarization direction.

While configurations in which one of the components (E or N) is along a nodal plane of a single source, or multiple sources dominate the signal on different components are possible, it is unlikely that source configurations are always the cause of the disagreement in the slowness vectors measured on the different components. In either case (multiple interfering sources or single sources), the horizontal seismograms should be rotated into their radial and tangential components to separate SH from SV waves, thus making the array analysis results cleaner, more stable, and more reliable.

6.5 Future work

A more advanced way of combining three-component analysis with array analysis needs to be developed. One approach is to determine the wave-field polarization for each station first, then rotate components into the radial and transverse directions before applying the array analysis. Because different stations are likely to have different polarization directions, an alternative approach is to average the array polarization before the rotation. Yet another approach is to perform the polarization analysis on component stacks (one stack at each array for E, N and Z) with delays based on array analysis. In any case determining the degree of planarity or even rectilinearity of the waveforms, and using this information to separate phase types or to average or weight the waveforms before array analysis is needed. Such detailed investigations are beyond the scope of this study.

A new study that could be implemented would be to use the Plate Boundary Observatory borehole strainmeters to resolve the slow events on shorter time scales than GPS; and simultaneously use the co-located borehole seismometers, which have better signal-to-noise than surface stations, to discern the timing of the initiation of the slow slip event and the tremor. In addition the borehole seismometers might allow for the better detection and quantification of wave types such as P-waves, and other phases. These phases could be used to understand the source process that causes the tremor. The borehole seismometers might allow for the detection of low frequency earthquakes within the tremor signal as is seen in Japan (Shelly et al, 2006).

Another small aperture seismic array experiment could be implemented. Ideally the number of stations in each array would be increased, the inter-station spacing would be decreased in order to better correlate the higher frequencies (at least up to 6 Hz), and the extent of the array would be increased to improve the estimation of the slowness vector. More than three of these arrays could be installed to cover a larger region such that the tremor

epicenters remain between at least three of the arrays at any given time. The arrays could also be located such that the time periods with multiple active source regions could be resolved by selectively using different subsets of the arrays. Then the tremor hypocenters could be tracked over a longer time period and possibly during all windows within the region of the arrays. However all of this comes at a substantial increase in labor and monetary costs.

BIBLIOGRAPHY

Abers, G.A., P.E. van Keken, E.A. Kneller, A. Ferris, and J.C. Stachnik (2006), The thermal structure of subduction zones constrained by seismic imaging: Implications for slab dehydration and wedge flow, *Earth and Plan. Sci. Lett., 241,* 387-397.

Aki, K. and R. Koyanagi (1981), Deep volcanic tremor and magma ascent mechanism under Kilauea, Hawaii, *J. Geophys. Res., 86* (B8), 7095-7109.

Almendros, J., B. Chouet, and P. Dawson (2001), Spatial extent of a hydrothermal system at Kilauea Volcano, Hawaii, determined from array analyses of shallow long-period seismicity. 1. Method, *J. Geophys. Res., 106*(B7), 13565-13580.

Aster, R., Borchers, and C. Thurber. *Parameter Estimation and Inverse Problems*. Burlington, MA: Elsevier Science & Technology, 2004.

Blakely, R.J., T.M. Brocher, and R.E. Wells (2005), Subduction-zone magnetic anomalies and implications for hydrated forearc mantle, *Geology, 33*(6), 445-448.

Bostock, M.G., R.D. Hyndman, S. Rondenay and S.M. Peacock (2002), An inverted continental Moho and serpentinization of the forearc mantle, *Nature, 417*, 536-538.

Brocher, T.M., T. Parsons, A.M. Trehu, C.M. Snelson, and M.A. Fisher (2003), Seismic evidence for widespread serpentinized forearc upper mantle along the Cascadia margin, *Geology*, *31* (3), 267-270.

Brodsky, E. E., B. Sturtevant, H. Kanamori (1998), Earthquakes, volcanoes, and rectified diffusion, *J. Geophys. Res., 103(B10),* 23827-23838.

Calvert, A.J., K. Ramachandran, H. Kao, and M.A. Fischer (2006), Local thickening of the Cascadia forearc crust and the origin of seismic reflectors in the uppermost mantle, *Tectonophysics, 420,* 175-188.

Chouet, B. (1996), New Methods and Future Trends in Seismological Volcano Monitoring, in *Monitoring and Mitigation of Volcano Hazards*, edited by R. Scarpa and R.I. Tilling, Springer-Verlag, Berlin/Heidelberg, Germany, pp. 23-97.

Chouet, B. (2003), Volcano Seismology, *Pure Appl. Geophys. 160*, 739-788.

Christensen, N.I. (2004), Serpentinites, peridotites, and seismology, in *Serpentine and Serpentinites: Minerology, Petrology, Geochemistry, Ecology, Geophysics and Tectonics*, edited by W.G. Ernst, Bellwether Publishing, Ltd., Columbia, MD, pp. 503-524.

Clark, I.D., and R.J. Phillips (2000), Geochemical and 3He/4He evidence for mantle and crustal contributions to geothermal fluids in the western Canadian continental margin, *J. Volc. Geotherm. Res., 104,* 261-276.

Crotwell, H.P., T.J. Owens, and J. Ritsema (1999). The TauP ToolKit: Flexible Seismic Travel-Time and Raypath Utilities, *Seis. Res. Lett., 70, 2,* 154-160.

Currie, C., J.F. Cassidy, and R.D. Hyndman (2001), A regional study of shear wave splitting above the Cascadia subduction zone: Margin-parallel crustal stress, *Geophys. Res. Lett. 28*(4), 659-662.

Dobson, D.P., P.G. Meredith, and S.A. Boon (2002), Simulation of subduction zone seismicity by dehydration of serpentine, *Science, 298,* 1407-1410.

Dragert, H., K. Wang, K, and T.S. James, (2001), *A silent slip event on the deeper Cascadia Subduction Interface, Science, 292,1525-1528.*

Evans, B. (2004), The serpentinite multi-system revisited: chrysotile is metastable, in *Serpentine and Serpentinites: Minerology, Petrology, Geochemistry, Ecology, Geophysics and Tectonics*, edited by W.G. Ernst, Bellwether Publishing, Ltd., Columbia, MD, pp.5-32.

Fruh-Green, G.L., D.S. Kelley, S.M. Bernasconi, J.A. Karson, K.A. Ludwig, D.A. Butterfield, C. Boschi, and G. Proskurowski (2003), 30,000 years of hydrothermal activity at the Lost City Vent Field, *Science, 301*, 495-498.

Fryer, P., and Mottl, M. (1997), *Shinkai 6500* investigations of a resurgent mud volcano on the southeastern Mariana forearc. *JAMSTEC J. Deep Sea Res., 13*, 103–114.

Gomberg, J., ,(1998) Earthquake triggering by transient and static deformations, *J. Geo. Res.*, *103,* 24411-24426.

Graindorge, D., G. Spence, P. Charvis, J.Y. Collot, R. Hyndman, and A.M. Trehu (2003), Crustal structure beneath the Strait of Juan de Fuca and

southern Vancouver Island from seismic and gravity analyses, *J. Geophys. Res., 108*.

Guillot, S., K.H. Hattori, and J. de Sigoyer (2000), Mantle wedge serpentinization and exhumation of eclogites: Insights from eastern Ladakh, northwest Himalaya, *Geology, 28*(3), 199-202.

Guillot, S., K.H. Hattori, J. de Sigoyer, T. Nagler, and A. Auzende (2001), Evidence of hydration of the mantle wedge and its role in the exhumation of eclogites, *Earth Plan. Sci Lett., 193*, 115-127.

Hacker, B.R., G.A. Abers, and S.M. Peacock (2003), Subduction factory, 1, Theoretical mineralogy, densities, seismic wave speeds, and H_2O contents, *J. Geophys. Res., 108*(B1), 2029, doi:10.1029/2001JB001127.

Hattori, K.H., and S. Guillot (2003), Volcanic fronts form as a consequence of serpentinite dehydration in the forearc mantle wedge, *Geology, 31*(6), 525-528.

Hirose, H., and K. Obara (2005), Repeating short- and long-term slow slip events with deep tremor activity around the Bungo channel region, southwest Japan, *Earth Planets Space, 57,* 961-972.

Hopkinson, L., J.S. Beard, C.A. Boulter (2004), The hydrothermal plumbing of a serpentinite-hosted detachment: evidence from the West Iberia non-volcanic rifted continental margin, *Marine Geology, 204,* 301-315.

Hyndman, R., and K. Wang (1995), The rupture zone of Cascadia great earthquakes from current deformation and the thermal regime, *J. Geophys. Res., 100*(B11), 22133-22154.

Hyndman, R. and S.M. Peacock, Serpentinization of the forearc mantle (2003), *Earth and Plan. Sci Lett., 212*, 417-432.

Ito, Y., and K. Obara (2006a), Dynamic deformation of the accretionary prism excites very low frequency earthquakes, *Geophys. Res. Lett., 33*(2), L02311.

Ito, Y., and K. Obara (2006b), Very low frequency earthquakes within accretionary prisms are very low stress-drop earthquakes, *Geophys. Res. Lett., 33*(9), L09302.

Julian, B.R. (1994), Volcanic tremor; nonlinear excitation by fluid flow, *J. Geophys. Res., 99* (B6), 11,859-11,878.

Jurkevics, A. (1988), Polarization analysis of 3-component array data*, Bull. of the Seis. Soc. of Am., 78*,(5), 1725-1743.

Kamaya, N., A. Katsumata, and Y. Ishigaki (2004), Low-frequency tremor and slow slip around the probably source region of the Tokai Earthquake- A new indicator for the Tokai Earthquake prediction provided by unified seismic networks in Japan, *USGS Open File Report 2005-1131*, 47.

Kao, H, and S. Shan (2004), The Source-Scanning Algorithm: mapping the distribution of seismic sources in time and space, *Geophys. J. Int.*, *157*, 589.

Kao, H., S. Shan, H. Dragert, G. Rogers, J.F. Cassidy, and K. Ramachandran (2006), A wide depth distribution of seismic tremors along the northern Cascadia margin, *Nature*, *436,* 841-844.

Keleman, P.B, N. Shimizu, and V.J.M. Salters (1995), Extraction of mid-ocean-ridge basalt from the upwelling of mantle by focused flow of melt in dunite channels, *Nature, 375,* 747-753.

Kelley, D.S., J.A. Karson, D.K. Blackman, Gretchen Früh-Green, Jeff Gee, D.A. Butterfield M.D. Lilley, E. J. Olson, M.O. Schrenk, K.R. Roe, and Shipboard Scientific Party (2001). An off-axis hydrothermal field discovered near the Mid-Atlantic Ridge at 30°N. *Nature, 412*, 145-149.

Kirby, S., E.R. Engdahl, and R. Denlinger (1996), Intermediate-depth intraslab earthquakes and arc volcanism as physical expressions of crustal and uppermost mantle metamorphism in subducting slabs, in *Subduction: Top to Bottom*, *AGU Monograph 96*, edited by G.E. Bebout et al., American Geophysical Union, Washington, D.C., 195-214.

Kodaira, S., T. Iidaka, A. Kato, J. Park, T. Iwasaki, and Y. Kaneda (2004), High pore fluid pressure may cause silent slip in the Nankai trough, *Science, 304,* 1295-1298.

Konstantinou, K.I. and V. Schlindwein (2002), Nature, wave-field properties and source mechanism of volcanic tremor: a review. *J. Volcanol. Geotherm. Res.*, *119*, 161-187.

La Rocca, M., G. Saccorotti, E. Del Pezzo, and J. Ibanez (2004), Probabilistic source location of explosion quakes at Stromboli volcano estimated with double array data, *J. Volc. and Geotherm. Res., 131*, 123-142.

La Rocca, M., W. McCausland, D. Galluzo, S. Malone, G. Saccorotti, and E. Del Pezzo (2005), Array measurements of deep tremor signals in the Cascadia subduction zone, *Geophys. Res. Lett., 32*, L21319.

La Rocca, M. D. Galuzzo, S. Malone, W. McCausland, G. Saccorotti, and E. Del Pezzo (2006), Array analysis of earthquakes in Puget Sound, Washington, submitted to *Bull. Of Seism. Soc of Amer.*

Linde, A.T., I.S. Sacks, M.J.S. Johnston, D.P. Hill and R.G. Bilham (1994), Increased pressure from rising bubbles as a mechanism for remotely triggered seismicity, *Nature, 371,* 408-410.

Liu, Y., and J.R. Rice (2005), Aseismic transients emerge spontaneously in three-dimensional rate and state modeling of subduction earthquake sequences, *J. of Geophys. Res., 110*.

MacDonald, A.H. and W.S. Fyfe (1985), Rate of Serpentinization in Seafloor Environments, *Tectonophys., 116,* 123-135.

Martin, B., and W.S. Fyfe (1970), Some Experimental and Theoretical Observations on the Kinetics of Hydration Reactions with Particular Reference to Serpentinization, *Chem. Geol., 6,* 185-202.

McCausland, W. and S. Malone (2004), Observations of deep, non-volcanic tremor in the Pacific Northwest, *Seis. Res. Lett., 74*, 281.

McCausland, W., S. Malone and D. Johnson (2005), Temporal and spatial occurrence of deep non-volcanic tremor: From Washington to northern California, *Geophys. Res. Lett., 32*, L24311.

McNutt, S.R. (1986), Observations and analysis of B-type earthquakes, explosions, and volcanic tremor at Pavlof Volcano, Alaska, *Bull. Of the Seism. Soc. Of Am., 76*(1), 153-175.

McNutt, S.R. (1996), Seismic monitoring and eruption forecasting of volcanoes: A review of the State-of-the-Art and case histories, in *Monitoring and Mitigation of Volcano Hazards*, ed. Scarpa, Tilling, Springer-Verlag, Berlin, Heidelberg, Germany, 99-196.

McNutt, S.R., Volcanic Seismicity (2000), in *Encyclopedia of Volcanoes*, ed. Sigurdsson, H., B. Houghton, S.R. McNutt, H. Rymer, and J. Stix, Academic Press, San Diego, CA, 1015-1033.

Medema, G.F. (2006), Juan de Fuca subducting plate geometry and intraslab seismicity, Unpublished doctoral dissertation, University of Washington, Seattle, WA.

Melbourne, T.I., W.M. Szeliga, M.M. Miller, and V.M. Santillan (2005), Extent and duration of the 2003 Cascadia slow earthquake, *Geophys. Res. Lett., 32,* L04301.

Miller, M., T. Melbourne, D.J. Johnson, and W.Q. Sumner (2002), Periodic slow earthquakes from the Cascadia subduction zone, *Science*, *295,* 2423.

Montgomery, D.R. and M. Manga (2003), Streamflow and water well responses to earthquakes, *Science, 300,* 2047-2049.

Nadeau, R.M. and D. Dolenc (2005), Non-volcanic tremors deep beneath the San Andreas Fault, *Science*, *307,* 389.

Nicholson, T., M. Bostock, and J.F. Cassidy (2005), New constraints on subduction zone structure in northern Cascadia, *Geophys. J. Int.*, *161*, 849-859.

Normand, C., A.E. Williams-Jones, R.F. Martin, and H. Vali (2002), Hydrothermal alteration of olivine in a flow-through autoclave: Nucleation and growth of serpentine phases, *Am. Mineral., 87*, 1699-1709.

Obara, K. (2002), Non-volcanic deep tremor associated with subduction in Southwest Japan, *Science*, *296*, 1679-1681.

Obara, K., and H. Hirose (2003), Spatial and temporal correlation between non-volcanic low-frequency tremors and slow slip events detected in the southwest Japan subduction zone, *Eos Trans. AGU, 84*(46), Fall Meet. Suppl., Abstract S42A-0139.

O'Hanley, D.S. (1992) Solution to the volume problem in serpentinization, *Geology, 20,* 705-708.

Peacock, S.M. (1990), Fluid processes in subduction zones, *Science, 248,* 329-337.

Peacock, S.M (1993), Large-scale hydration of the lithosphere above subducting slabs, *Chem. Geology, 108,* 49-59.

Peacock, S.M. (1996), Thermal and petrologic structure of subduction zones, in *Subduction: Top to Bottom, AGU Monograph 96*, edited by G.E. Bebout et al., American Geophysical Union, Washington, D.C., 119-133.

Peacock, S.M. and K. Wang (1999), Seismic consequences of warm versus cool subduction metamorphism: Examples from southwest and northeast Japan, *Science, 286,* 937-939.

Peacock, S., K. Wang, and A.M. McMahon (2002), Thermal structure and metamorphism of subducting oceanic crust: Insight into Cascadia intraslab earthquakes, in *The Cascadia Subduction Zone and Related Subduction Systems – Seismic Structure, Intraslab Earthquakes and Processes, and Earthquake Hazards*, edited by S. Kirby, K. Wang and S. Dunlap, Open-File Report 02328, U.S. Geological Survey,123-126.

Peterson, C., Christensen, D. and S. McNutt (2005), Episodic Tremor in the Alaska/Aleutian Subduction Zone, *Eos Trans. AGU, 86* (52), Fall Meet. Supple. Abstract G51B-0830.

Preston, L., and K. Creager (2003), Intraslab earthquakes; dehydration of the Cascadia slab, *Science, 302,* 1197-1200.

Ramachandran, K., S.E. Dosso, G.D. Spence, R. D. Hyndman, and T.M. Brocher (2005), Forearc structure beneath southwestern British Columbia: A three-dimensional tomographic velocity model, *J. of Geophys. Res., 110*.

Roeloffs, E., and A. Linde (2007), Borehole observations of continuous strain and fluid pressure, in *Volcano Deformation*, ed. D. Dzurisin, Springer-Verlag and Praxis Publishing, p. 305-322.

Rogers, G., and H. Dragert (2003), Episodic tremor and slip on the Cascadia subduction zone: The chatter of silent slip", *Science, 300,* 1942-1943.

Rogers, G., H. Dragert, J. Cassidy, and K. Wang (2003), The north Cascadia Episodic Tremor and Slip (ETS) Event of February and March 2003, *Eos Trans. AGU, 84*(46), Fall Meet. Suppl., Abstract S42G-01.

Saccorotti, G., and E. Del Pezzo (2000), A probabilistic approach to the inversion of data from a seismic array and its application to volcanic signals, *Geophys. J. Int., 143*, 249-261.

Saffer, D., and B.A. Bekins (1998), Episodic fluid flow in the Nankai accretionary complex: Timescale, geochemistry, flow rates, and fluid budget, *J. Geophys. Res., 103*(B12), 30351-3-370.

Saffer, D., and A.W. McKiernan (2005), Permeability of underthrust sediments at the Costa Rican subduction zone: Scale dependence and implications for dewatering, *Geophys. Res. Lett., 32*, L02302, doi:10.1029/2004GL021388.

Schick, R. (1992), Volcanic tremor: seismic signals of (Almost) unknown origin, In *Volcanic Seismology*, ed. Gasparini P, Scarpa R, Aki K, Springer, Berlin Heidelberg New York, 157–167.

Segall, P., E.K. Desmarais, D. Shelly, A. Miklius, and P. Cervelli (2006), Earthquakes triggered by silent slip events on Kilauea volcano, Hawaii, *Nature (442),* 71-7.

Shelly, D. R., G.C. Beroza, S. Ide and S. Nakamula, (2006), Low-Frequency Earthquakes in Shikoku, Japan, and their relationship to episodic tremor and slip, *Nature,442,* 188-191.

Soyer, W. and M. Unsworth (2006), Deep electrical structure of the northern Cascadia (British Columbia, Canada) subduction zone: Implications for the distribution of fluids, *Geology, 34,* 53-56.

Spiegelman, M, and P.B. Kelemen (2003), Extreme chemical variability as a consequence of channelized melt transport, *Geochem. Geophys. Geosyst., 4*(7), doi:10.1029/2002GC000336.

Szeliga, W., T.I. Melbourne, M.M. Miller, V.M. Santillan (2004), Southern Cascadia episodic slow earthquakes, *Geophys. Res. Lett., 31*, L16602.

Vidale, J. and P.M. Shearer (2006), A survey of 71 earthquake bursts across southern California: Exploring the role of pore fluid pressure fluctuations and aseismic slip as drivers, *J. of Geophys. Res., 111* (B), doi:10.1029/2005JB004034.

Voight, B., et al. (2006), Unprecedented pressure increase in deep magma reservoir triggered by lava-dome collapse, *Geophys. Res. Lett. , 33,* L03312, doi:10. 1029/ 2005GL024870.

Wang, Z., D. Zhao, O.P. Mishra, and A. Yamada (2006), Structural heterogeneity and its implications for the low frequency tremors in Southwest Japan, *Earth and Plan. Sci. Lett., 251,* 66-78.

Wegner, W.W., and W.G. Ernst (1983), Experimentally determined hydration and dehydration reaction rates in the system MgO-Sio2-H2O, *Amer. J. of Sci., 283-A,* 151-180

Yamamoto, E., S. Matsumura, and T. Ohkubo (2005), A slow slip event in the Tokai area detected by tilt and seismic observation and its possible recurrence, *Earth Planets Space, 57,* 917-923.

APPENDIX 1

Five-Minute Time Window Locations by Day. Two-dimensional histograms of locations for five-minute time windows from July 6 - 22, and July 24, 2004. Locations misfits < 400 are plotted; average uncertainties for all locations are 10.9 ± 5.2 km in x, 10.2 ± 5.1 in y, and 14.4 ± 5.4 in z. For each day the figure consists of 3 sub-figures: in the top left of the figure, the locations are projected onto the X-Y plane; in the top right figure the locations are projected onto the Z-Y plane; and in the bottom left the locations are projected onto the X-Z plane. Latitude is plotted as kilometers from 46.25N, and longitude is plotted as kilometers from 124.5W. The number of locations at any given grid point indicated by the color bar to the left; red indicates more locations, dark blue indicates none. The array locations are indicated by triangles.

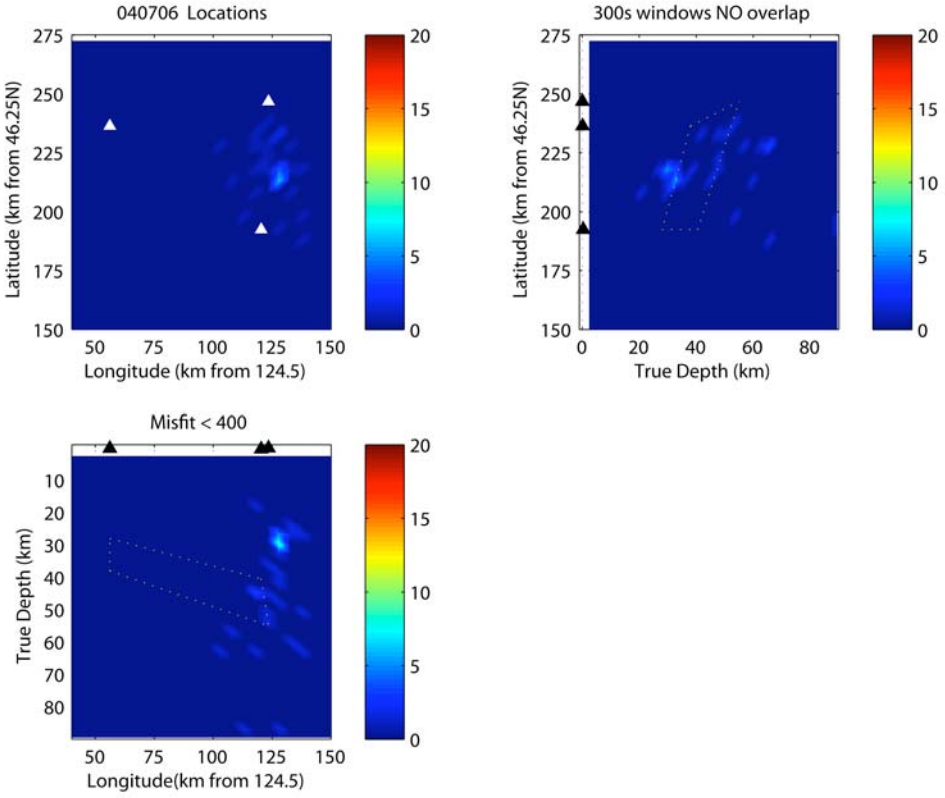

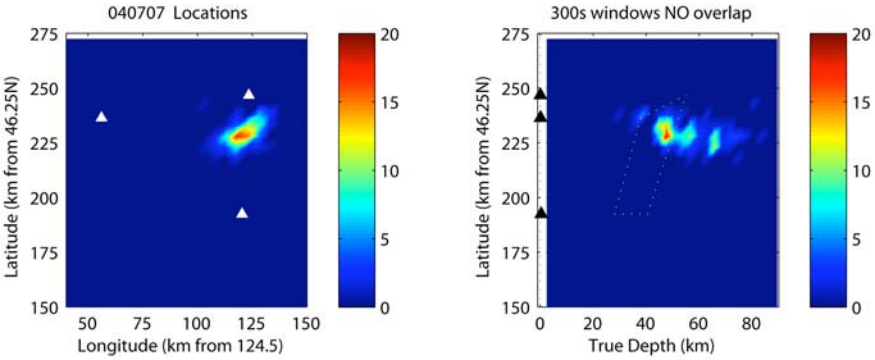
040707 Locations
Latitude (km from 46.25N)
Longitude (km from 124.5)
300s windows NO overlap
Latitude (km from 46.25N)
True Depth (km)

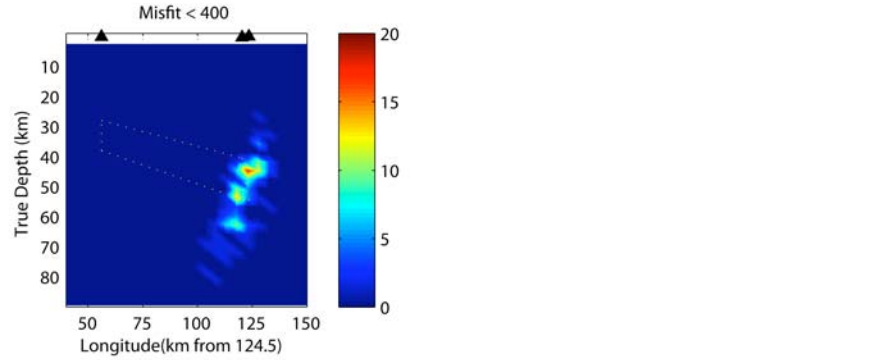
Misfit < 400
True Depth (km)
Longitude(km from 124.5)

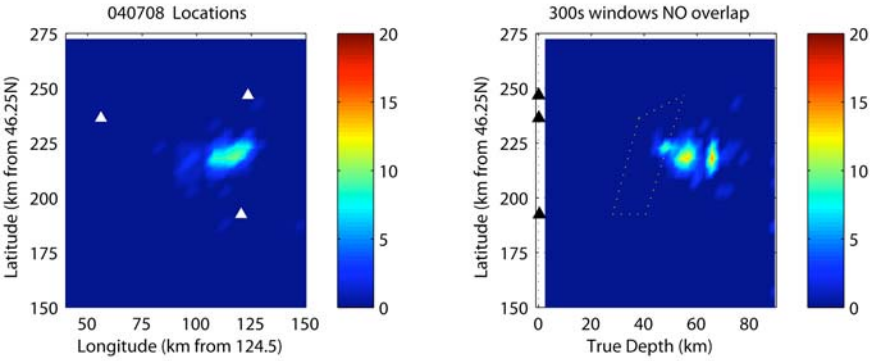
040708 Locations
Latitude (km from 46.25N)
Longitude (km from 124.5)
300s windows NO overlap
Latitude (km from 46.25N)
True Depth (km)

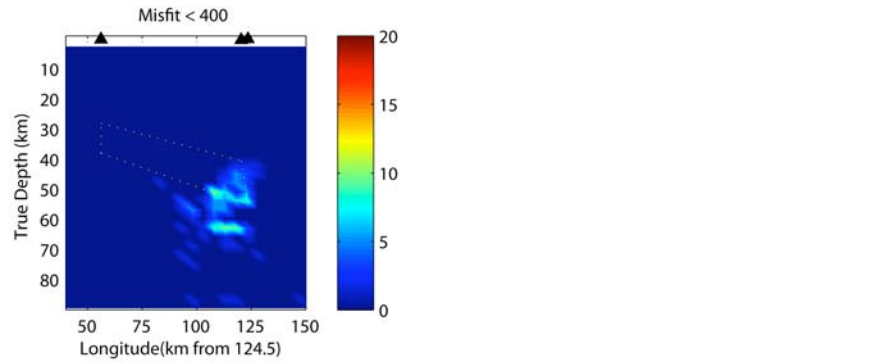
Misfit < 400
True Depth (km)
Longitude(km from 124.5)

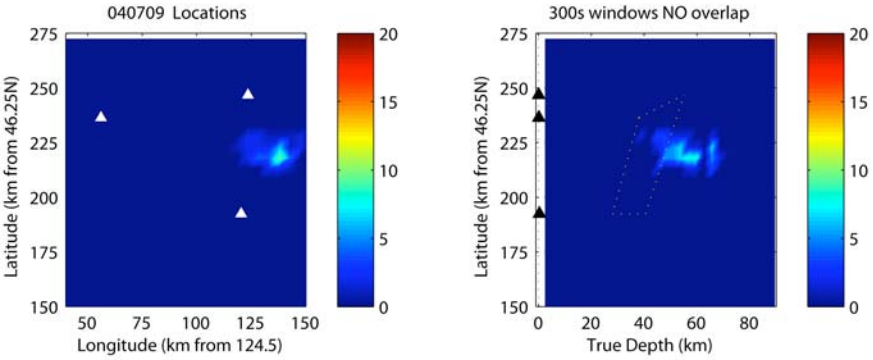
040709 Locations
Latitude (km from 46.25N)
Longitude (km from 124.5)
300s windows NO overlap
Latitude (km from 46.25N)
True Depth (km)

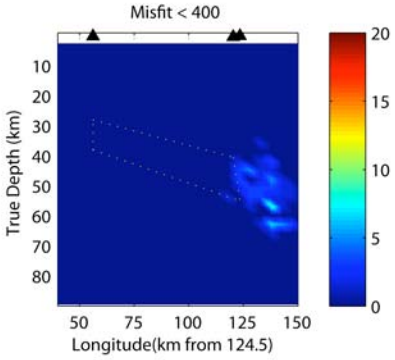
Misfit < 400
True Depth (km)
Longitude(km from 124.5)

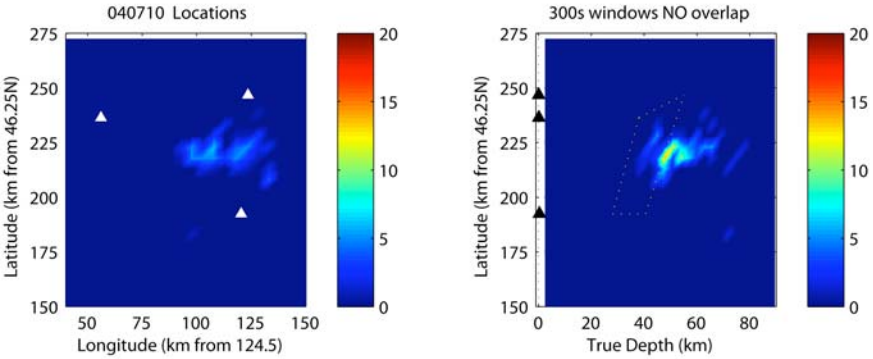
040710 Locations
Latitude (km from 46.25N)
Longitude (km from 124.5)
300s windows NO overlap
Latitude (km from 46.25N)
True Depth (km)

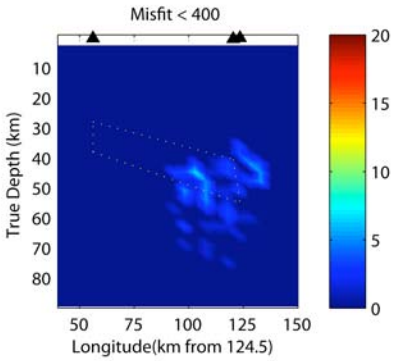
Misfit < 400
True Depth (km)
Longitude(km from 124.5)

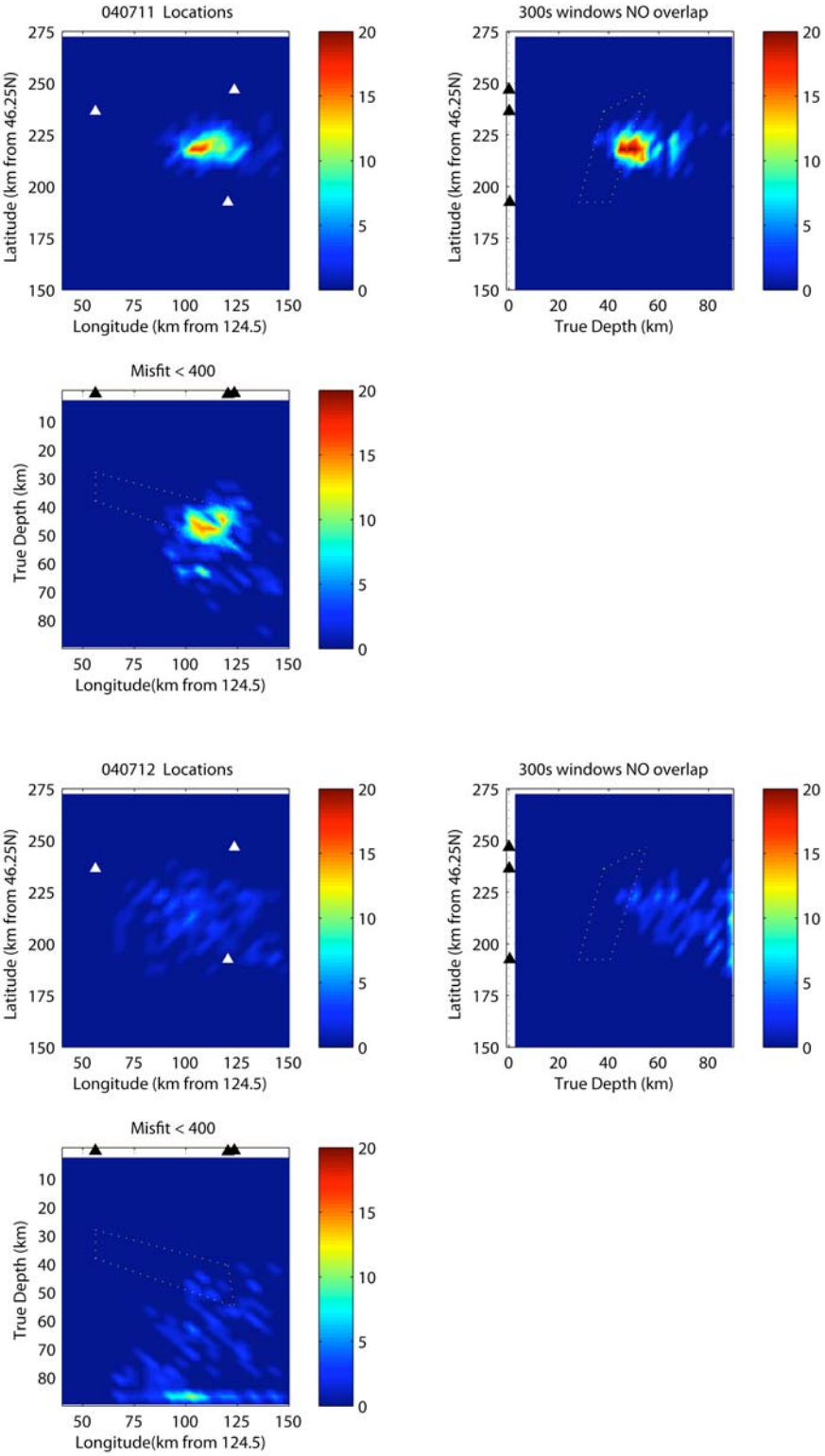
040711 Locations
Latitude (km from 46.25N)
Longitude (km from 124.5)
300s windows NO overlap
Latitude (km from 46.25N)
True Depth (km)
Misfit < 400
True Depth (km)
Longitude(km from 124.5)
040712 Locations
Latitude (km from 46.25N)
Longitude (km from 124.5)
300s windows NO overlap
Latitude (km from 46.25N)
True Depth (km)
Misfit < 400
True Depth (km)
Longitude(km from 124.5)

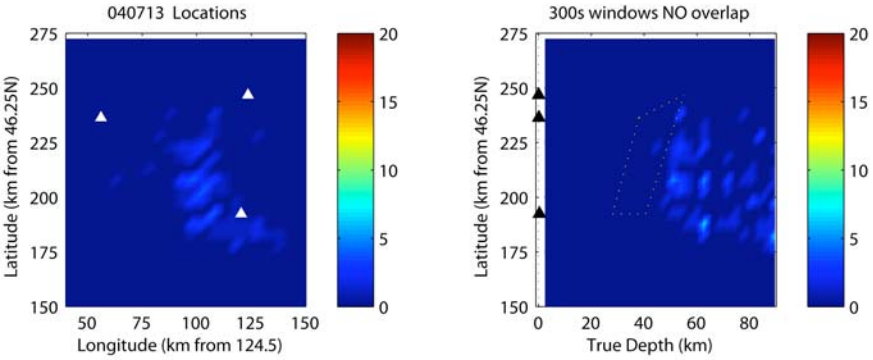
040713 Locations
Latitude (km from 46.25N)
Longitude (km from 124.5)
300s windows NO overlap
Latitude (km from 46.25N)
True Depth (km)

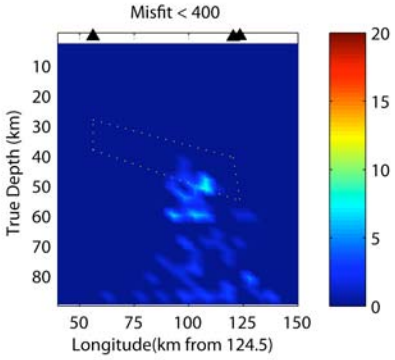
Misfit < 400
True Depth (km)
Longitude(km from 124.5)

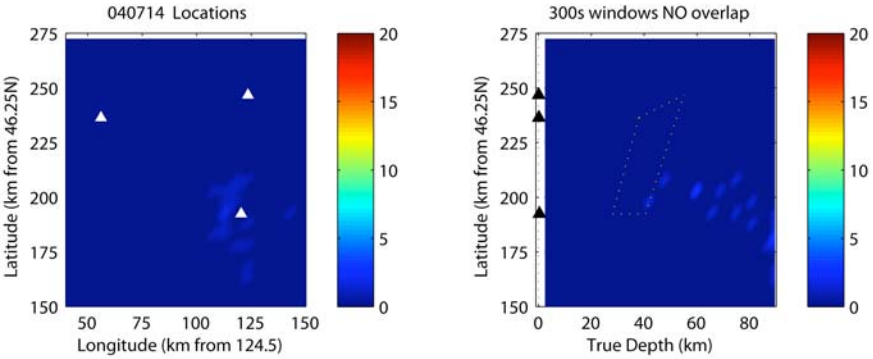
040714 Locations
Latitude (km from 46.25N)
Longitude (km from 124.5)
300s windows NO overlap
Latitude (km from 46.25N)
True Depth (km)

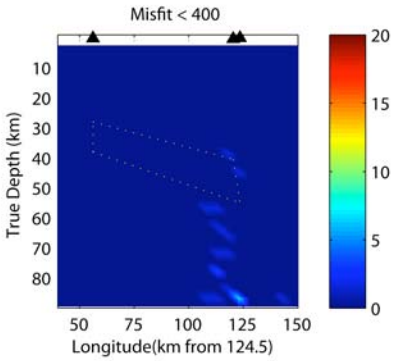
Misfit < 400
True Depth (km)
Longitude(km from 124.5)

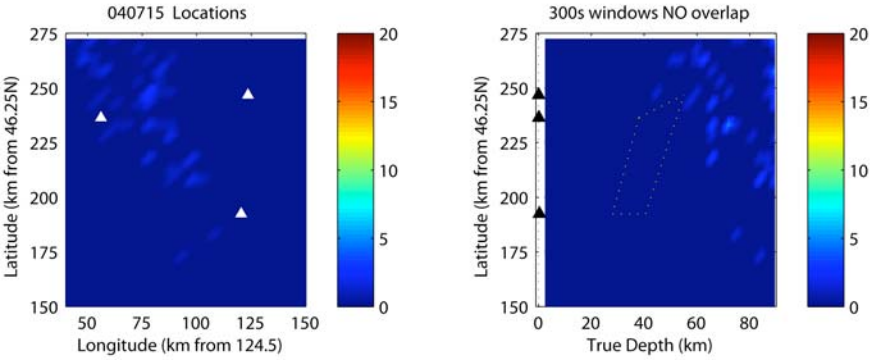
040715 Locations
Latitude (km from 46.25N)
Longitude (km from 124.5)
300s windows NO overlap
Latitude (km from 46.25N)
True Depth (km)

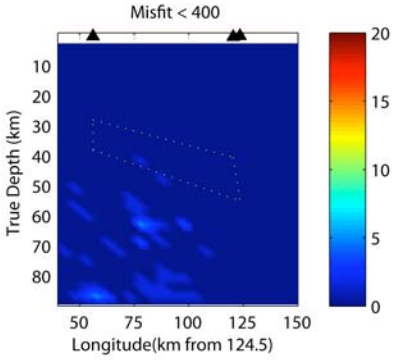
Misfit < 400
True Depth (km)
Longitude(km from 124.5)

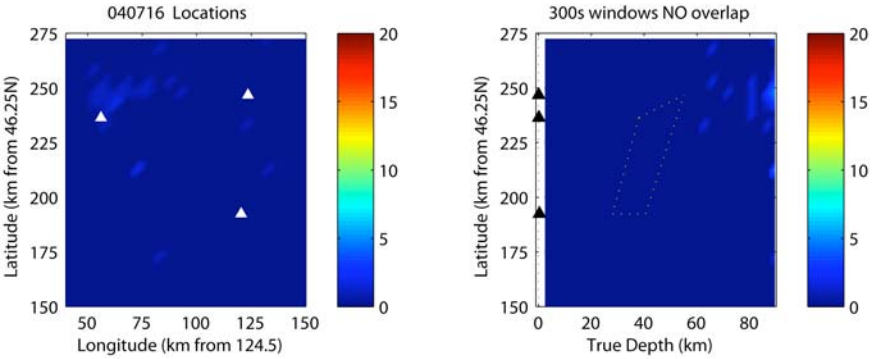
040716 Locations
Latitude (km from 46.25N)
Longitude (km from 124.5)
300s windows NO overlap
Latitude (km from 46.25N)
True Depth (km)

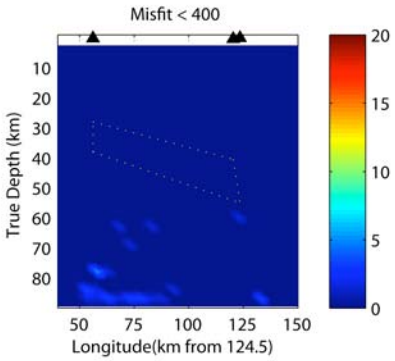
Misfit < 400
True Depth (km)
Longitude(km from 124.5)

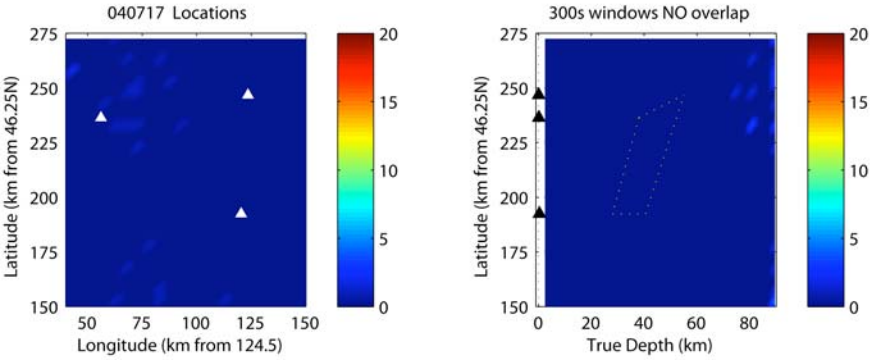
040717 Locations
Latitude (km from 46.25N)
Longitude (km from 124.5)
300s windows NO overlap
Latitude (km from 46.25N)
True Depth (km)

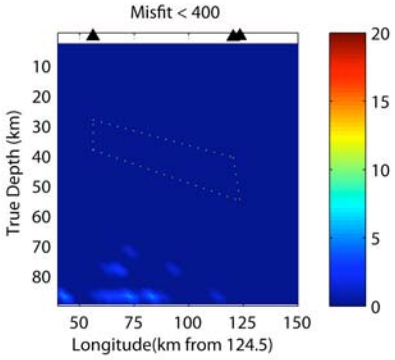
Misfit < 400
True Depth (km)
Longitude(km from 124.5)

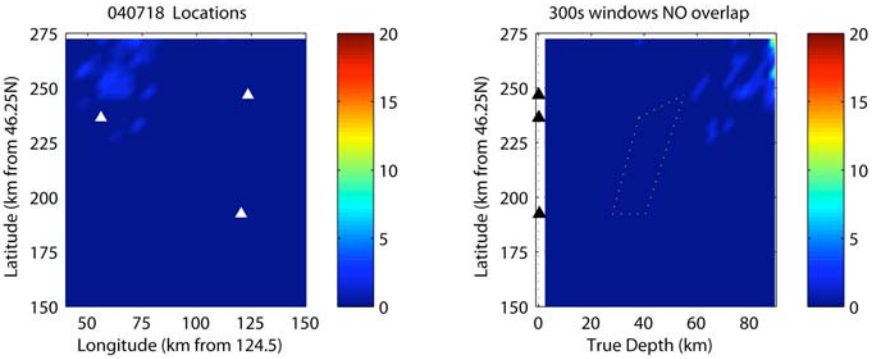
040718 Locations
Latitude (km from 46.25N)
Longitude (km from 124.5)
300s windows NO overlap
Latitude (km from 46.25N)
True Depth (km)

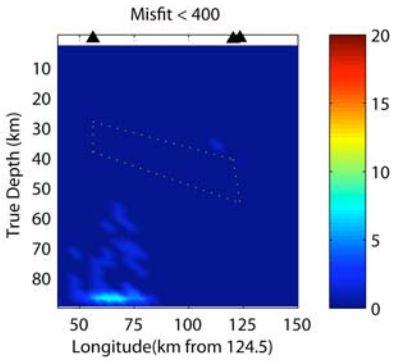
Misfit < 400
True Depth (km)
Longitude(km from 124.5)

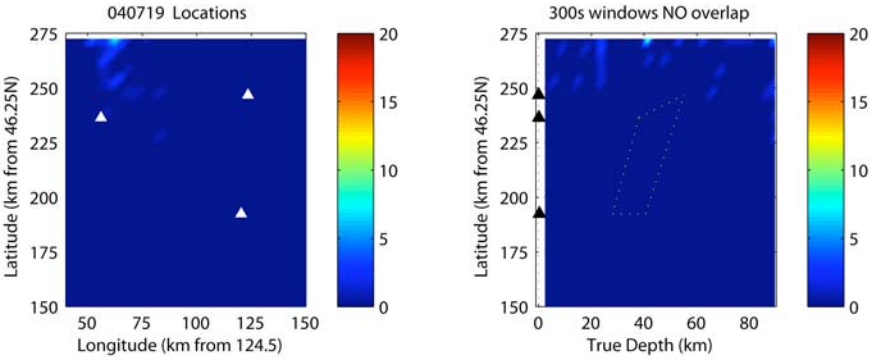
040719 Locations
Latitude (km from 46.25N)
Longitude (km from 124.5)
300s windows NO overlap
Latitude (km from 46.25N)
True Depth (km)

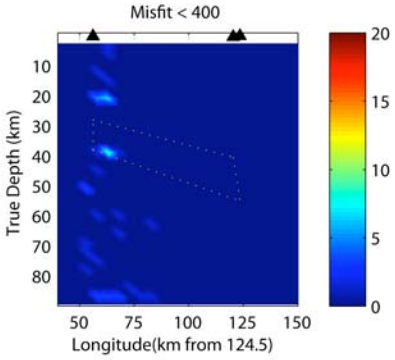
Misfit < 400
True Depth (km)
Longitude(km from 124.5)

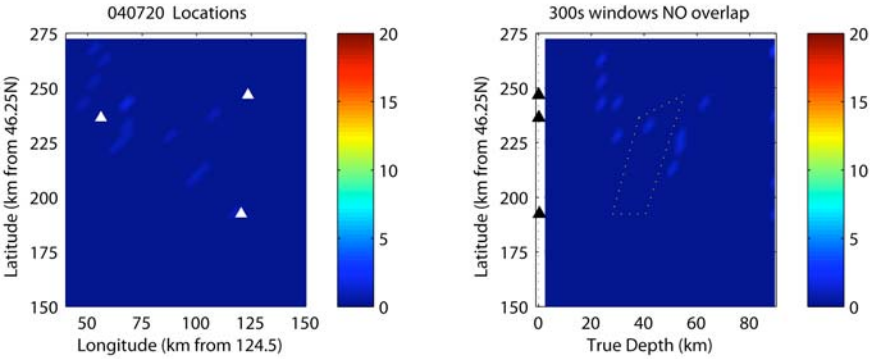
040720 Locations
Latitude (km from 46.25N)
Longitude (km from 124.5)
300s windows NO overlap
Latitude (km from 46.25N)
True Depth (km)

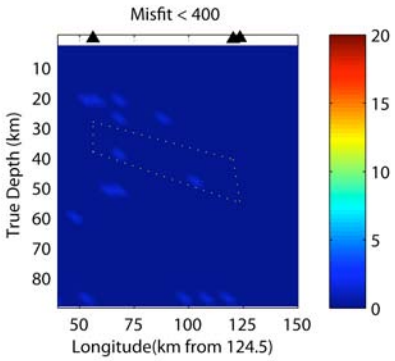
Misfit < 400
True Depth (km)
Longitude(km from 124.5)

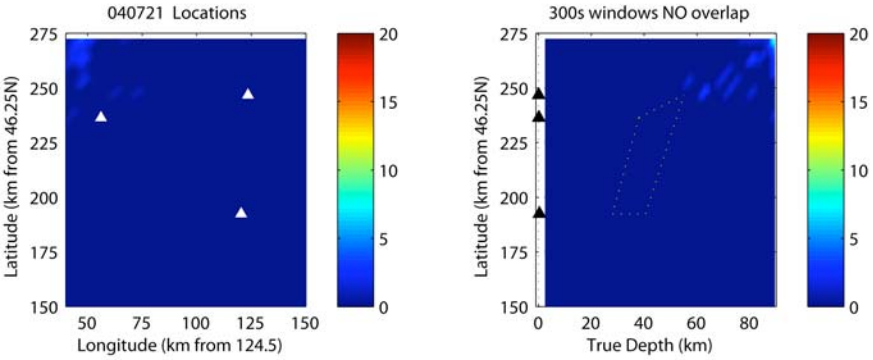
040721 Locations
Latitude (km from 46.25N)
Longitude (km from 124.5)
300s windows NO overlap
Latitude (km from 46.25N)
True Depth (km)

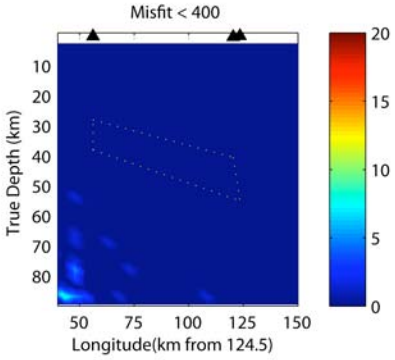
Misfit < 400
True Depth (km)
Longitude(km from 124.5)

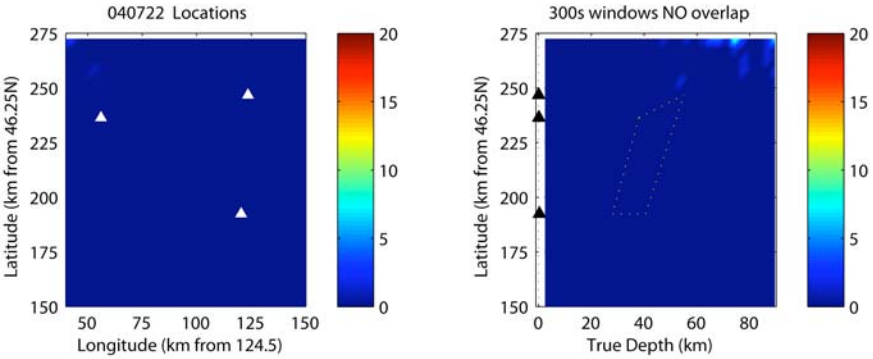
040722 Locations
Latitude (km from 46.25N)
Longitude (km from 124.5)
300s windows NO overlap
Latitude (km from 46.25N)
True Depth (km)

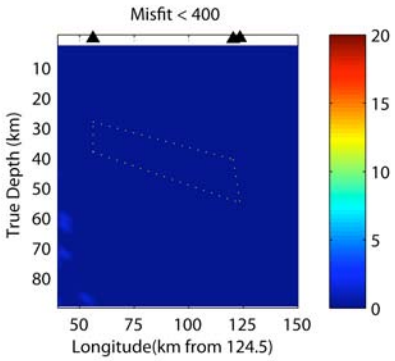
Misfit < 400
True Depth (km)
Longitude(km from 124.5)

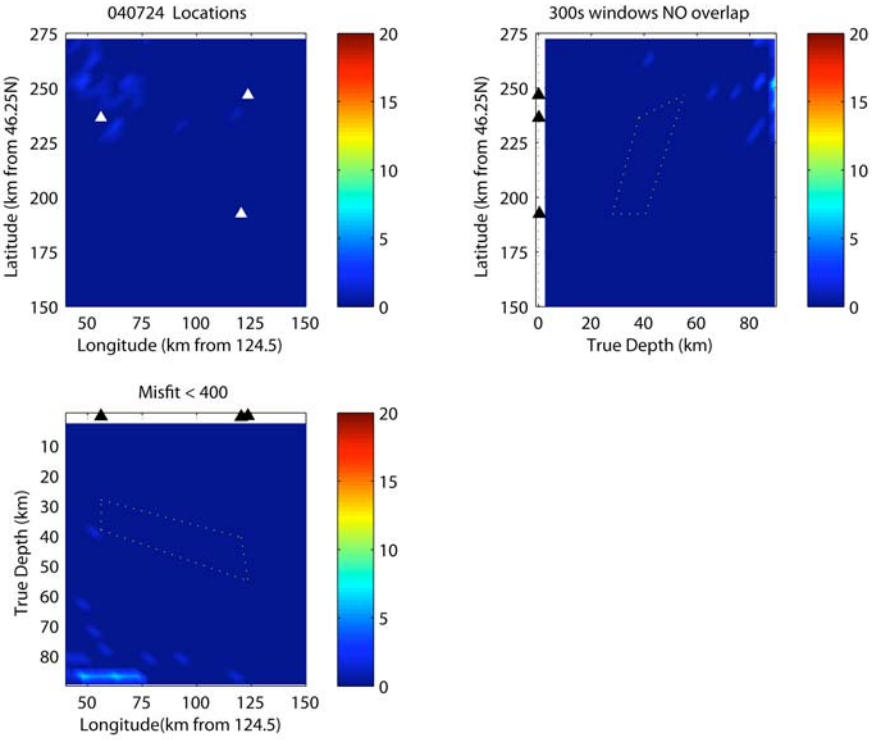
040724 Locations
Latitude (km from 46.25N)
Longitude (km from 124.5)
300s windows NO overlap
Latitude (km from 46.25N)
True Depth (km)
Misfit < 400
True Depth (km)
Longitude(km from 124.5)

APPENDIX 2

Array Analysis Time Series Data by Day .The mean of the maximum cross-correlation coefficient, slowness (from east and north components), back-azimuth (from east and north components), wave incidence angle (inverse sine of the ratio of the average velocity in the surface layer to the apparent velocity), polarity azimuth, degree of planarity (1 is purely planar), and degree of rectilinearity (1 is purely rectilinear) are plotted from top to bottom for five-minute time window data for each day between July 6 – 22, 2004 for each array (Sooke, Sequim, Lopez). Values were plotted when the travel time errors were less than 20 milliseconds and when the slowness was less than 0.35 s/km. Black values are quantities that are calculated using both components (E and N), therefore when the values are not plotted they either do not meet the plotting criterion, or only one of the components (N or E) does not meet the criterion. For slowness and back-azimuth blue represents values calculated on the north components and red represents values calculated on the east components of data, the red values are plotted last and therefore plot on top of the blue. July 9 represents the second half of the day, not first half as suggested by the time axis.

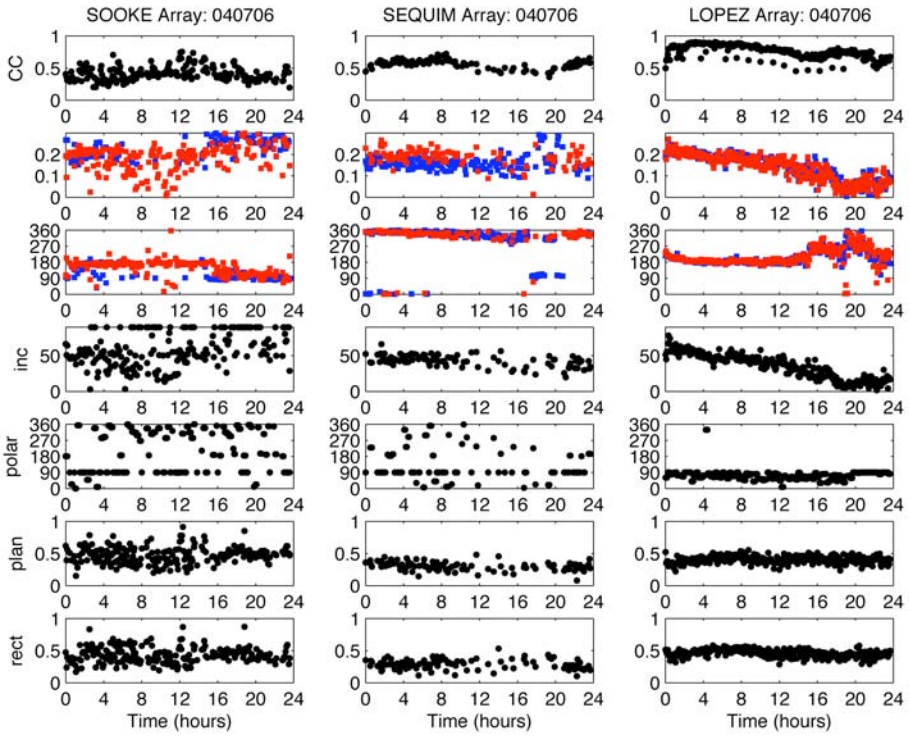

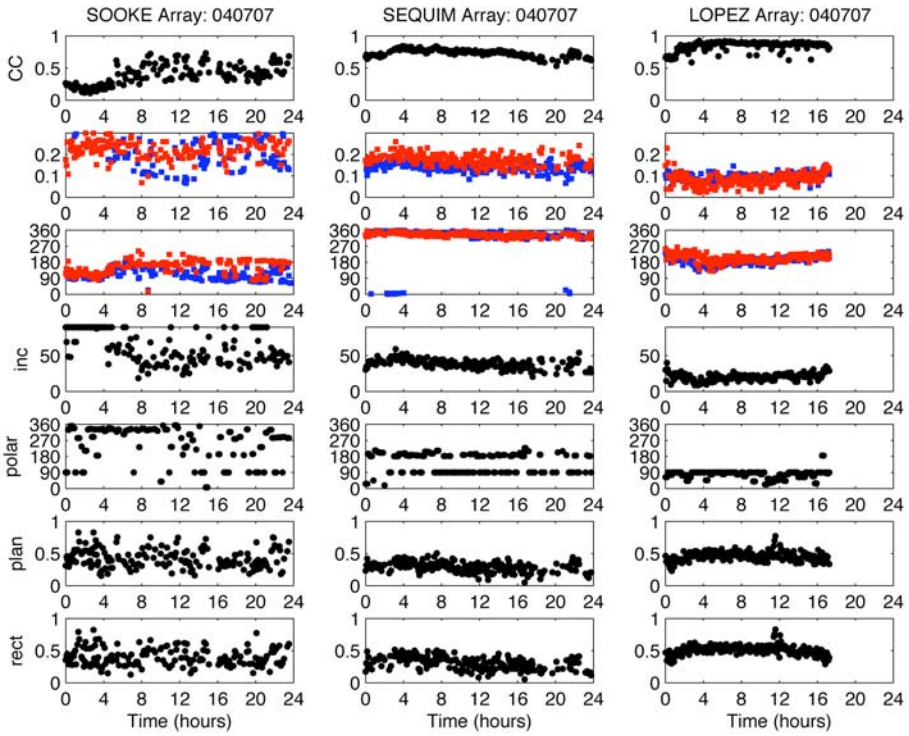
SOOKE Array: 040707
SEQUIM Array: 040707
LOPEZ Array: 040707
CC
inc
polar
plan
rect
Time (hours)

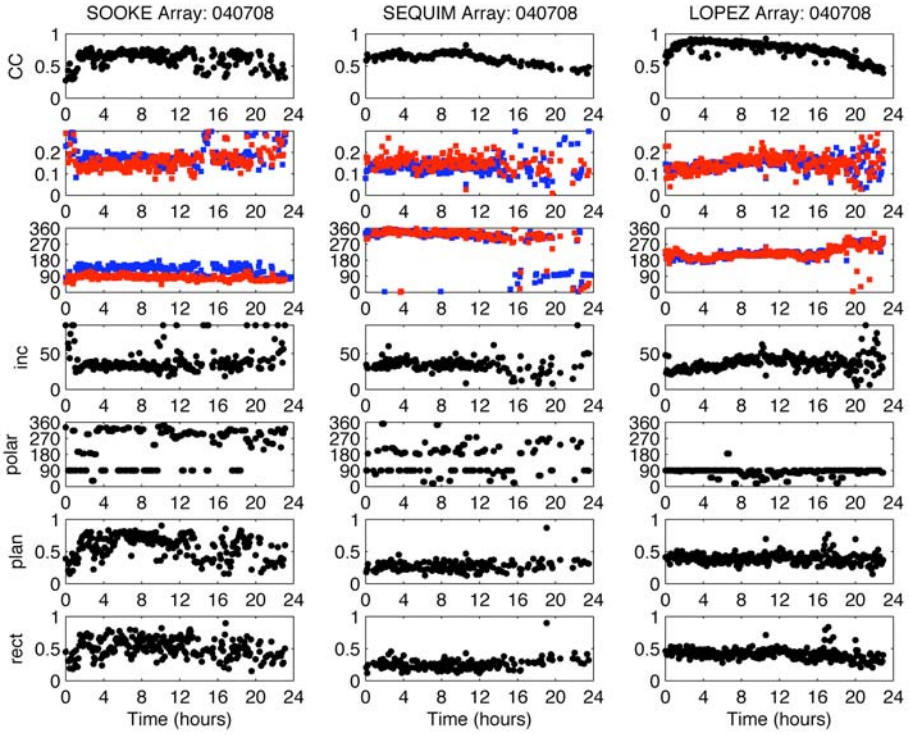
SOOKE Array: 040708
SEQUIM Array: 040708
LOPEZ Array: 040708
CC
inc
polar
plan
rect
Time (hours)

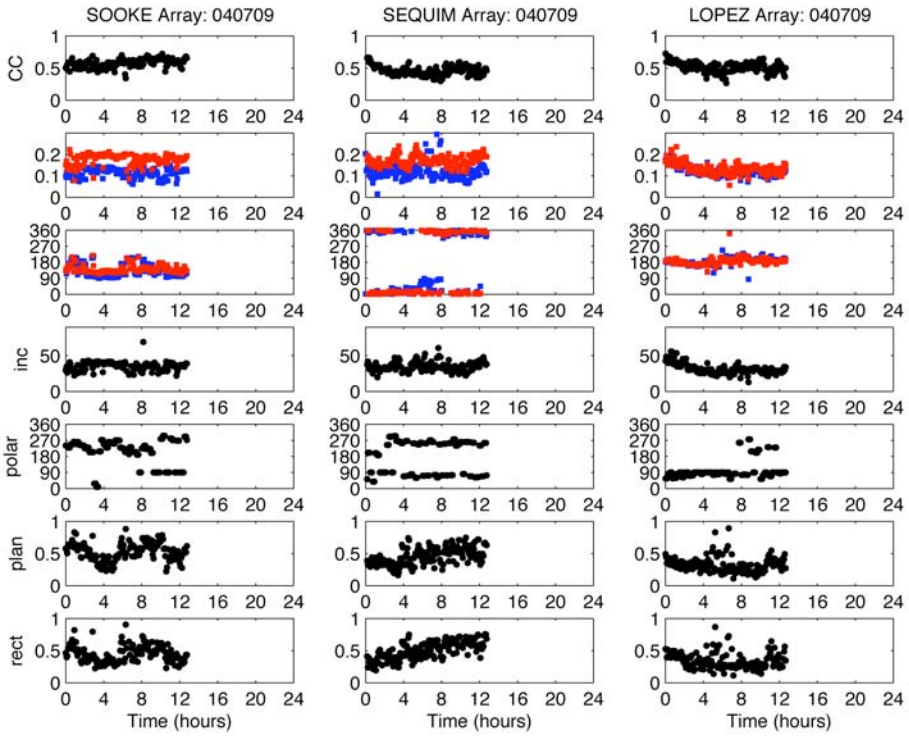
SOOKE Array: 040709
SEQUIM Array: 040709
LOPEZ Array: 040709
CC
inc
polar
plan
rect
Time (hours)

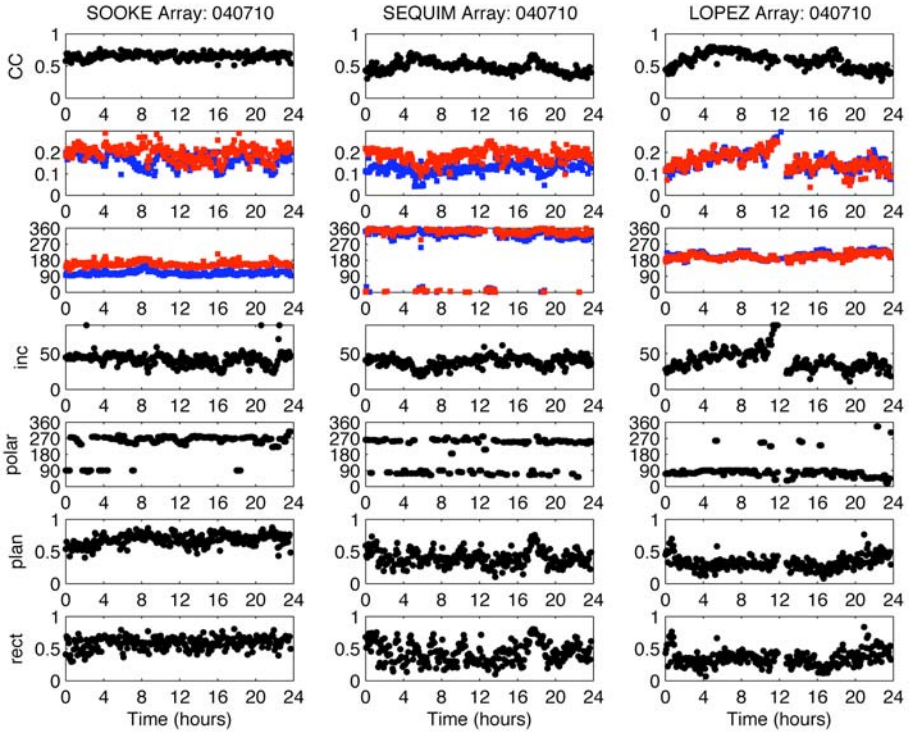
SOOKE Array: 040710
SEQUIM Array: 040710
LOPEZ Array: 040710
CC
inc
polar
plan
rect
Time (hours)

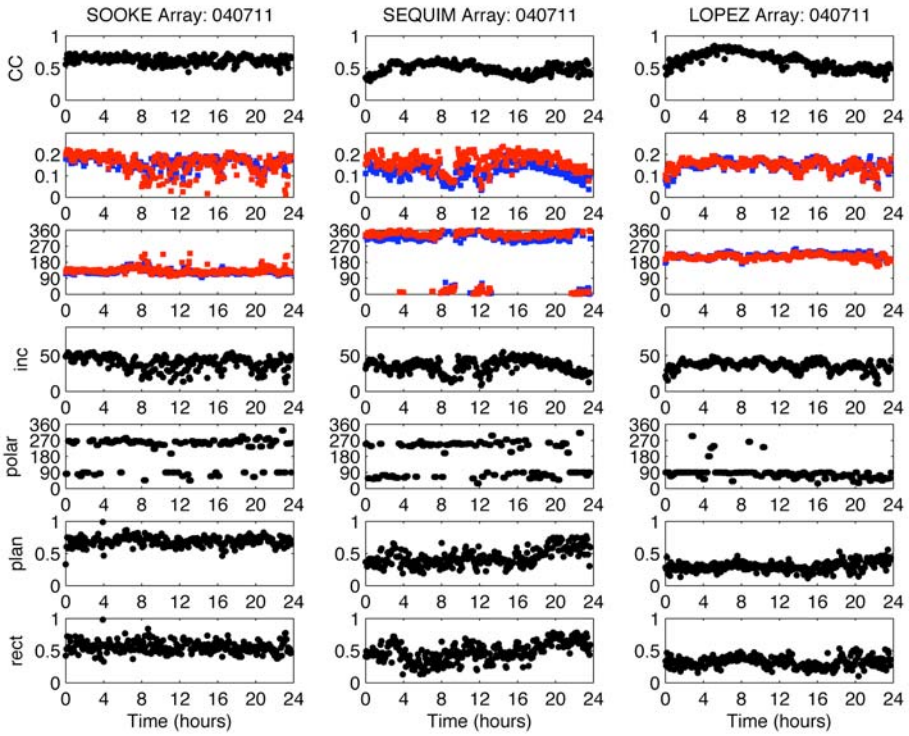
SOOKE Array: 040711
SEQUIM Array: 040711
LOPEZ Array: 040711
CC
inc
polar
plan
rect
Time (hours)

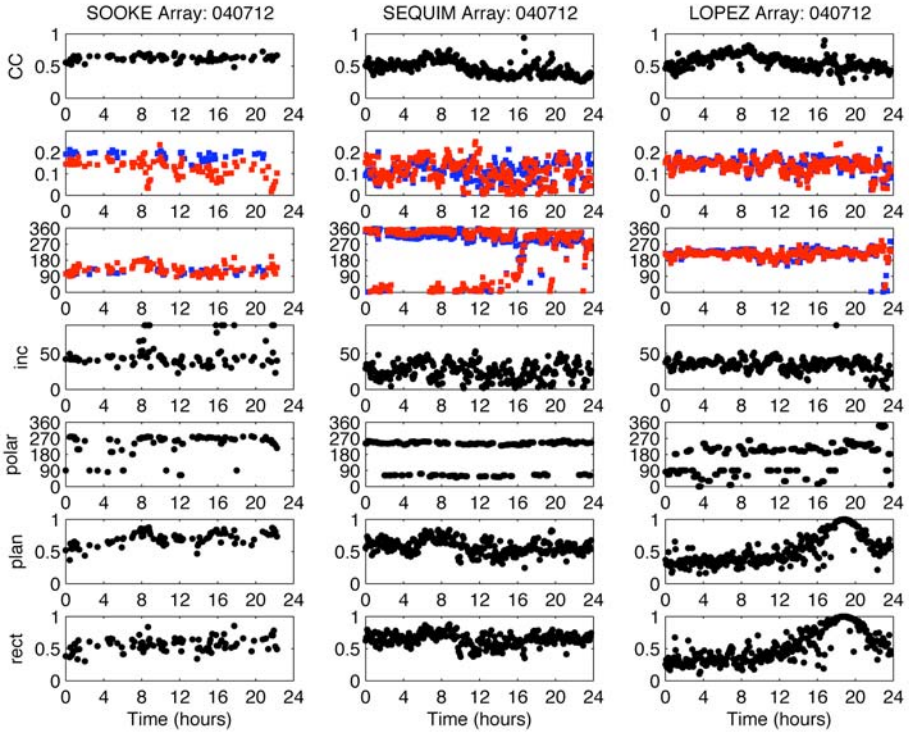
SOOKE Array: 040712
SEQUIM Array: 040712
LOPEZ Array: 040712
CC
inc
polar
plan
rect
Time (hours)

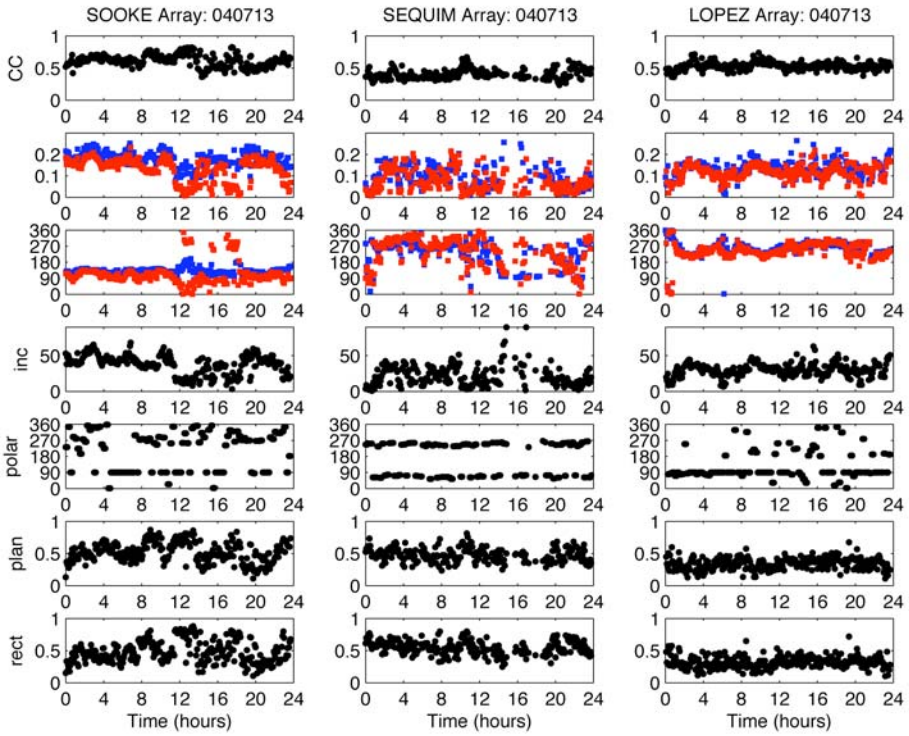
SOOKE Array: 040713
SEQUIM Array: 040713
LOPEZ Array: 040713
CC
inc
polar
plan
rect
Time (hours)

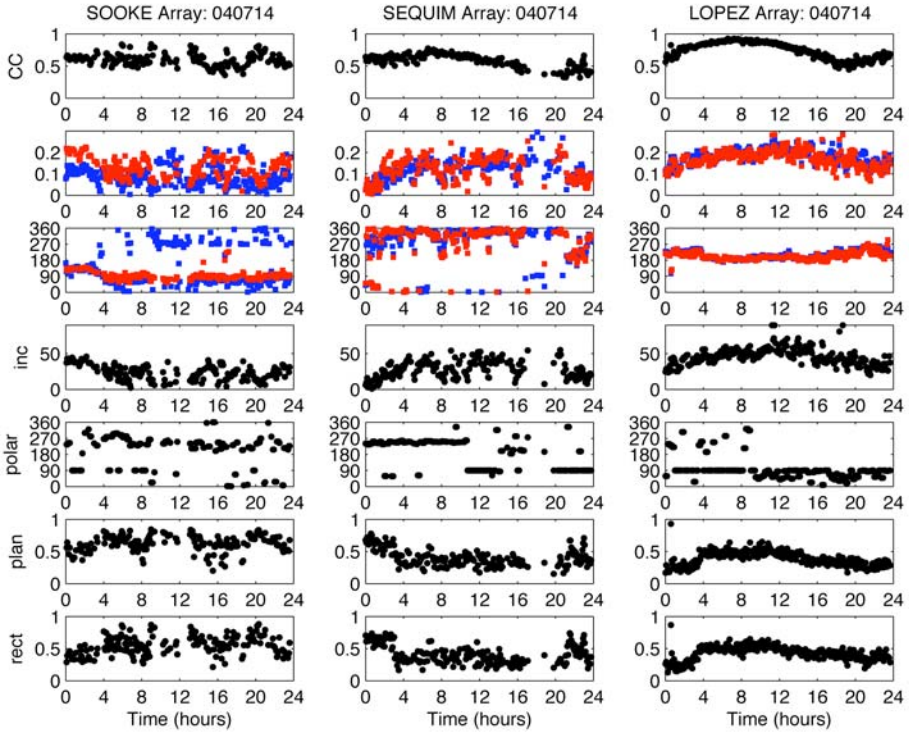
SOOKE Array: 040714
SEQUIM Array: 040714
LOPEZ Array: 040714
CC
inc
polar
plan
rect
Time (hours)

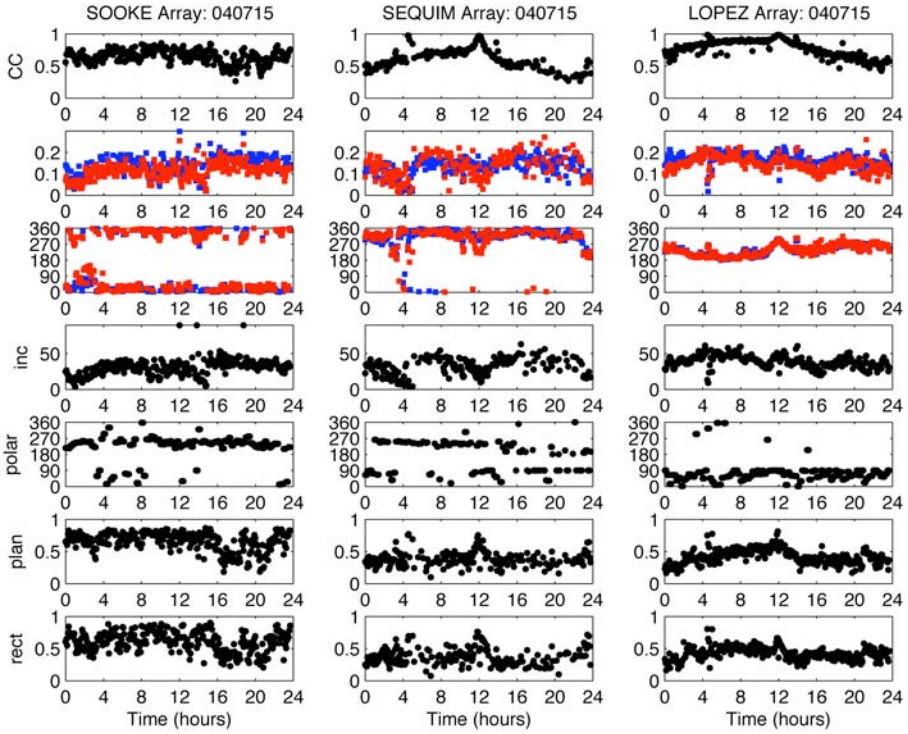
SOOKE Array: 040715
SEQUIM Array: 040715
LOPEZ Array: 040715
CC
inc
polar
plan
rect
Time (hours)

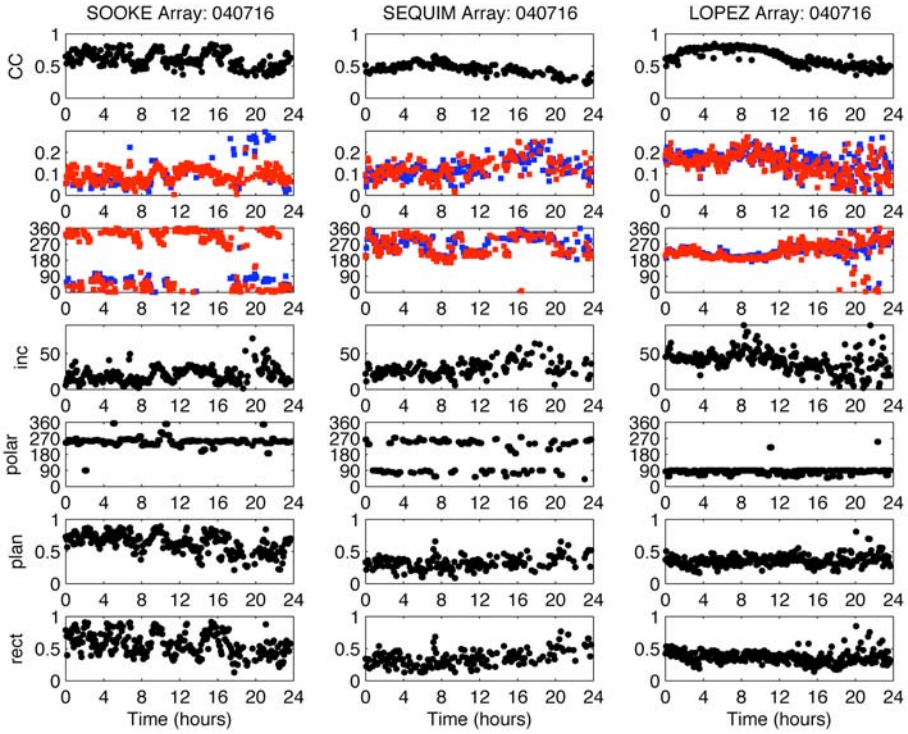
SOOKE Array: 040716
SEQUIM Array: 040716
LOPEZ Array: 040716
CC
inc
polar
plan
rect
Time (hours)

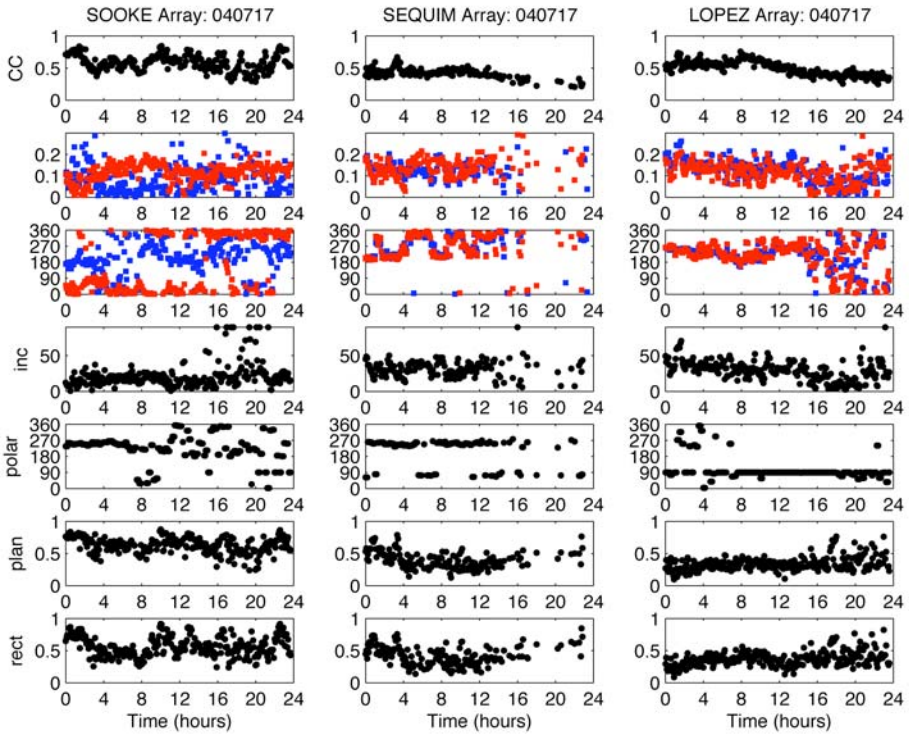
SOOKE Array: 040717
SEQUIM Array: 040717
LOPEZ Array: 040717
CC
inc
polar
plan
rect
Time (hours)

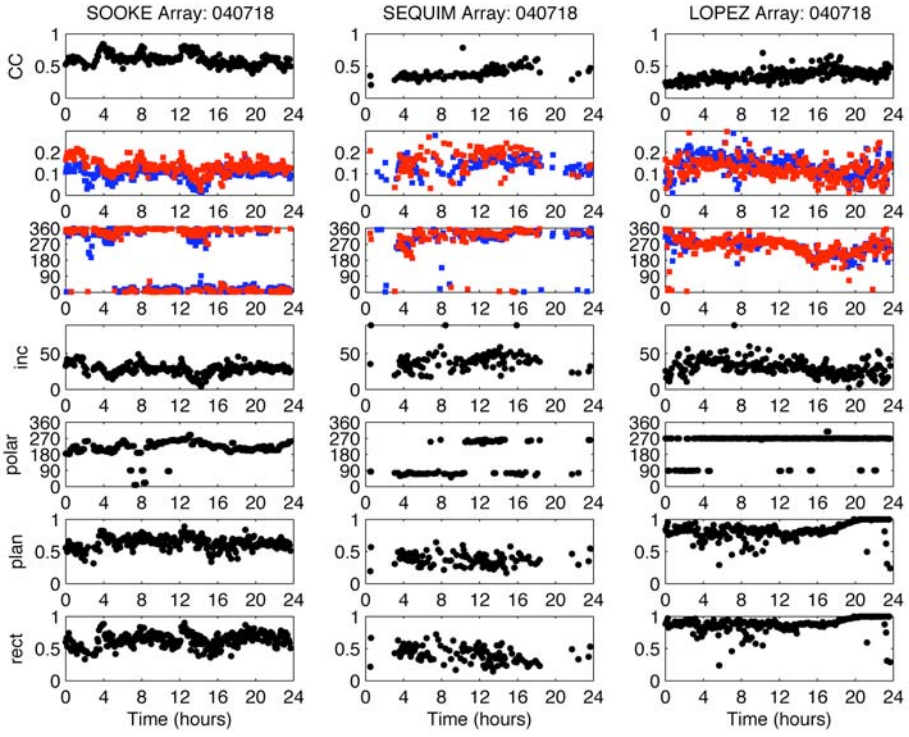
SOOKE Array: 040718
SEQUIM Array: 040718
LOPEZ Array: 040718
CC
inc
polar
plan
rect
Time (hours)

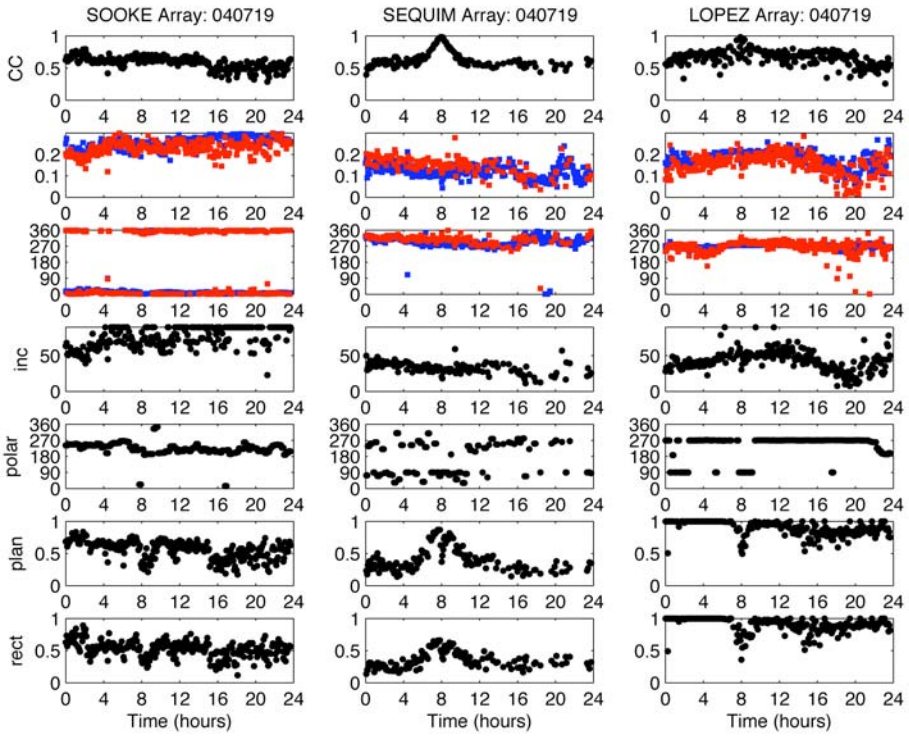
SOOKE Array: 040719
SEQUIM Array: 040719
LOPEZ Array: 040719
CC
inc
polar
plan
rect
Time (hours)
Time (hours)
Time (hours)

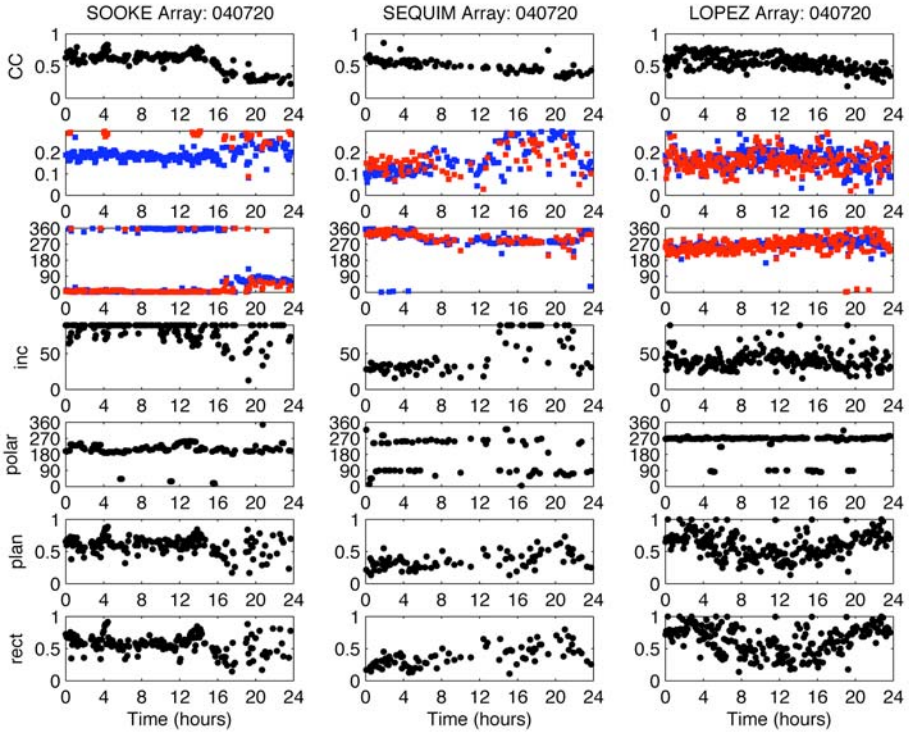
SOOKE Array: 040720
SEQUIM Array: 040720
LOPEZ Array: 040720
CC
inc
polar
plan
rect
Time (hours)
Time (hours)
Time (hours)

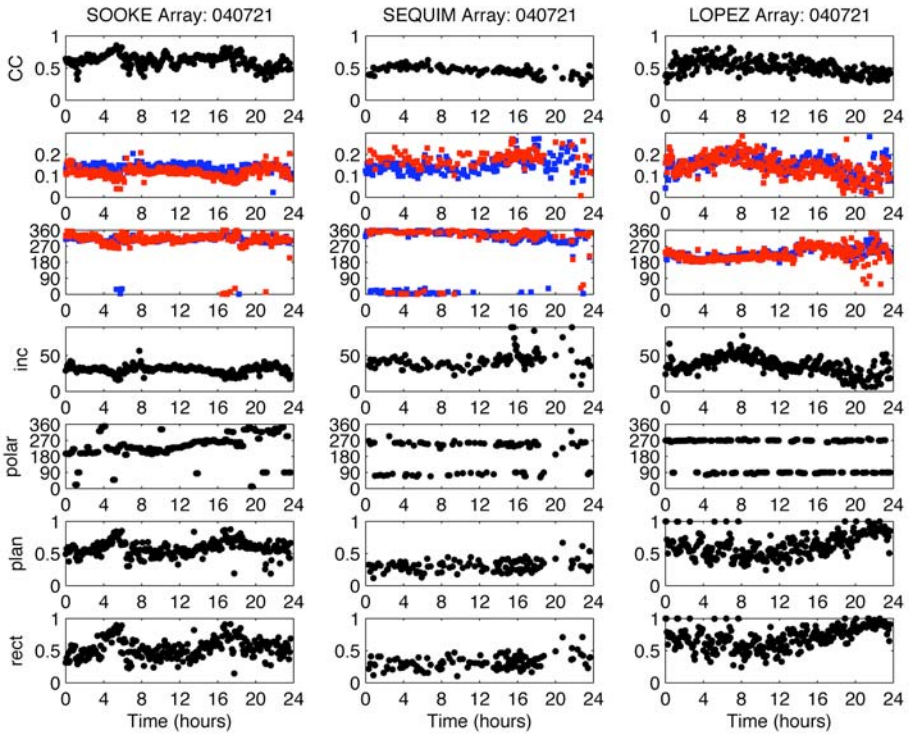
SOOKE Array: 040721
SEQUIM Array: 040721
LOPEZ Array: 040721
CC
inc
polar
plan
rect
Time (hours)

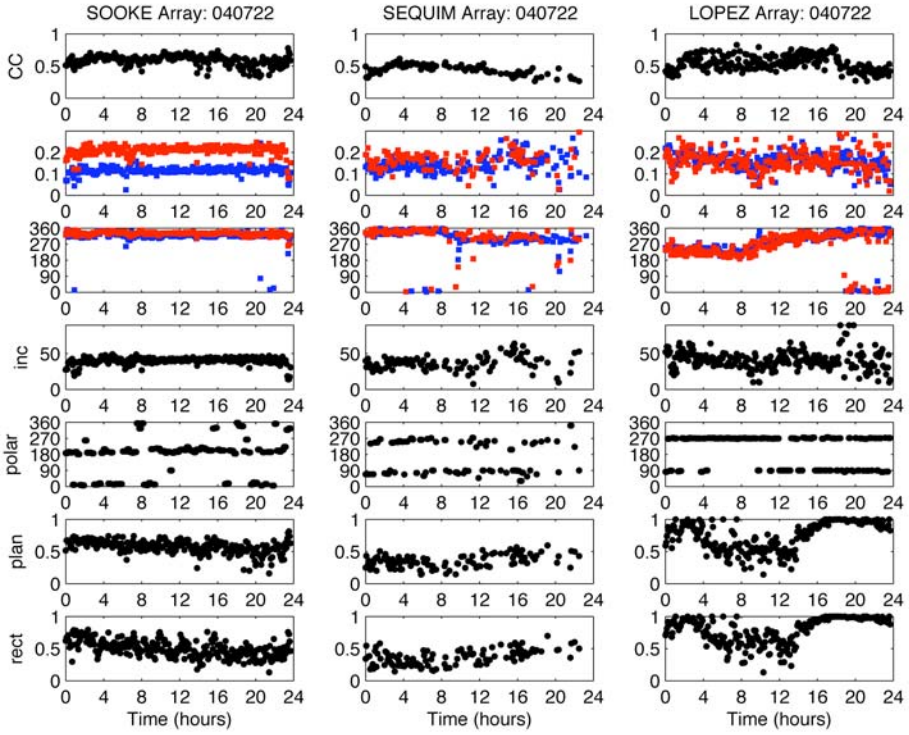
SOOKE Array: 040722
SEQUIM Array: 040722
LOPEZ Array: 040722
CC
inc
polar
plan
rect
Time (hours)

APPENDIX 3

Hour by Hour Locations for Five-Minute Time Windows. Hour-by-hour histograms of locations for 300s time windows from hour 15:00 on July 11 to hour 1:00 on July 12, 2004. Locations are for misfits less than 300, location errors for the entire time window are 7.6 ± 2.1 km in x, 6.5 ±1.9 km in y, and 11.0 ± 3.1 km in z. Locations jump from one region to another, particularly between 22:00 and 23:00 on July 11. Yellow trapezoids are the projection of the top of the subducting slab (Preston et al., 2003; Medema, 2006). Projections were taking along east-west profiles at the latitude of the Sooke and Sequim arrays, and along north-south profiles at the longitude of Sooke and Lopez arrays.

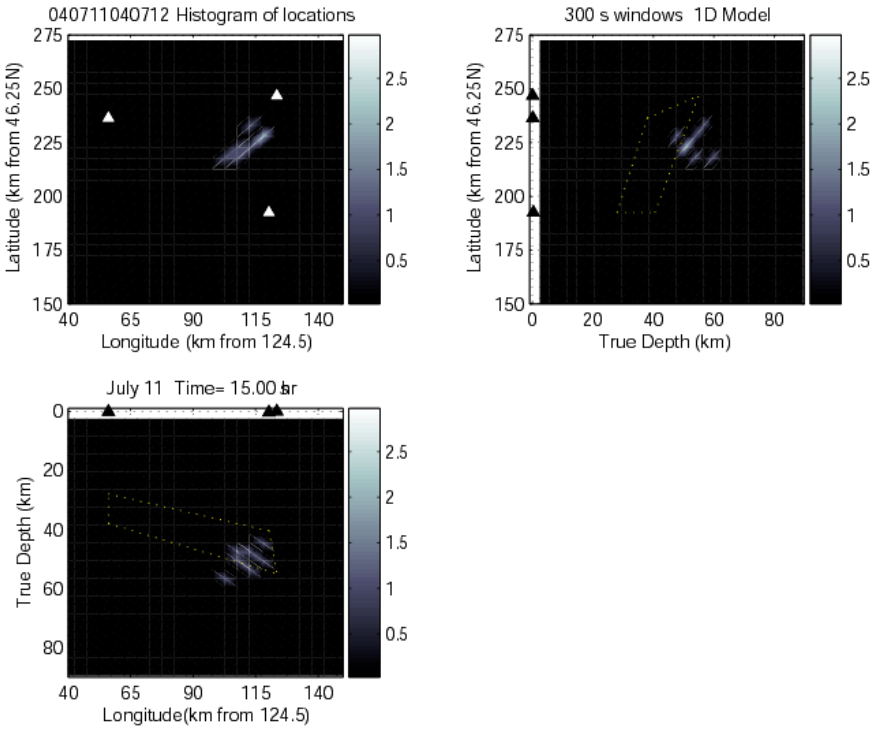

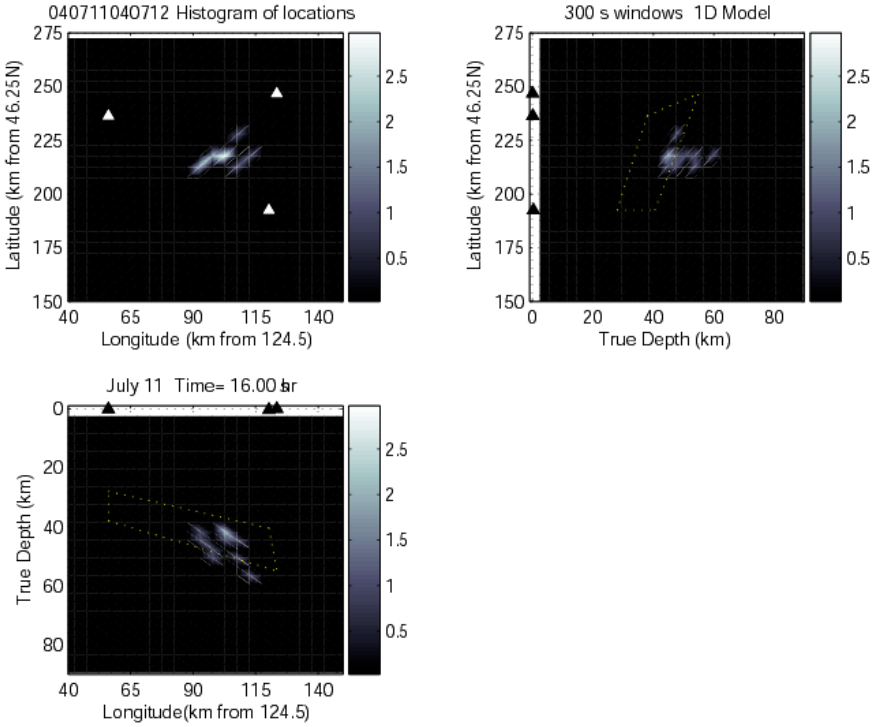
040711040712 Histogram of locations
Latitude (km from 46.25N)
Longitude (km from 124.5)
300 s windows 1D Model
Latitude (km from 46.25N)
True Depth (km)
July 11 Time= 16.00 hr
True Depth (km)
Longitude(km from 124.5)

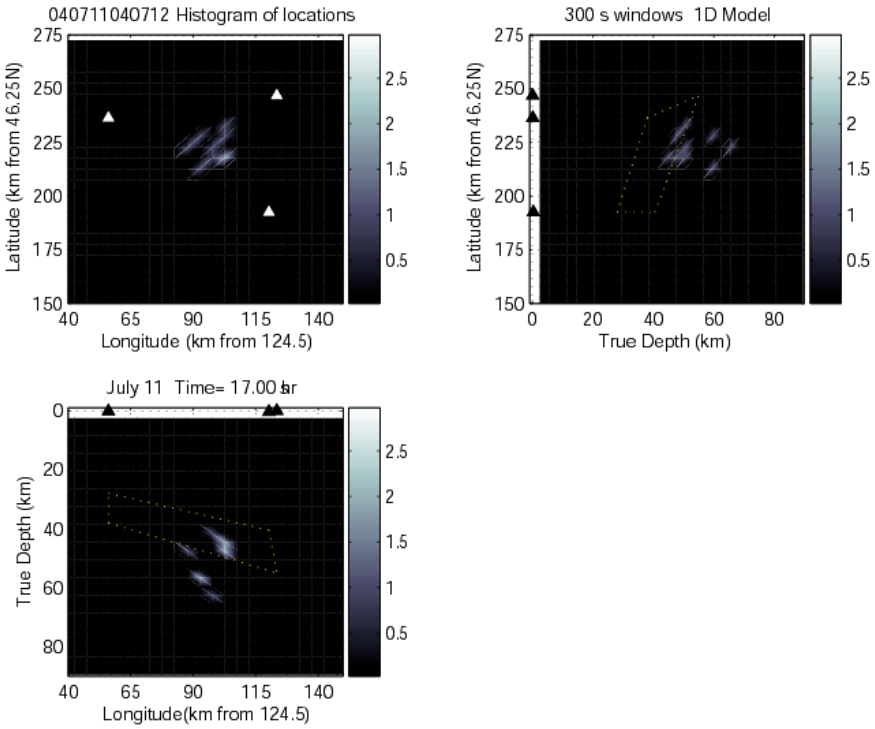
040711040712 Histogram of locations
Latitude (km from 46.25N)
Longitude (km from 124.5)
300 s windows 1D Model
Latitude (km from 46.25N)
True Depth (km)
July 11 Time= 17.00 hr
True Depth (km)
Longitude(km from 124.5)

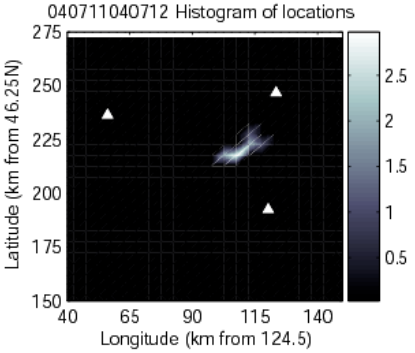
040711040712 Histogram of locations
Latitude (km from 46.25N)
Longitude (km from 124.5)

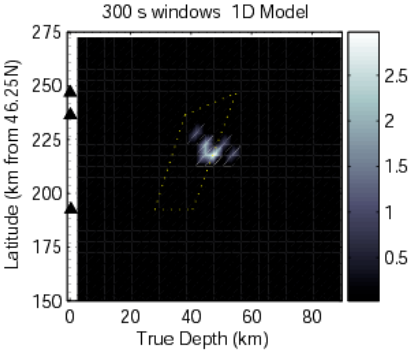
300 s windows 1D Model
Latitude (km from 46.25N)
True Depth (km)

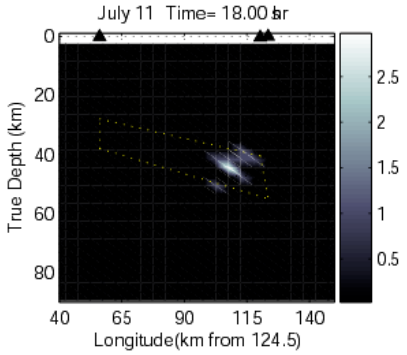
July 11 Time= 18.00 hr
True Depth (km)
Longitude(km from 124.5)

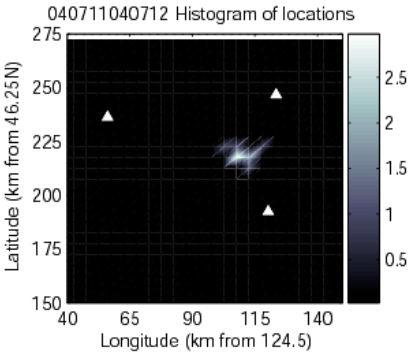
040711040712 Histogram of locations
Latitude (km from 46.25N)
Longitude (km from 124.5)

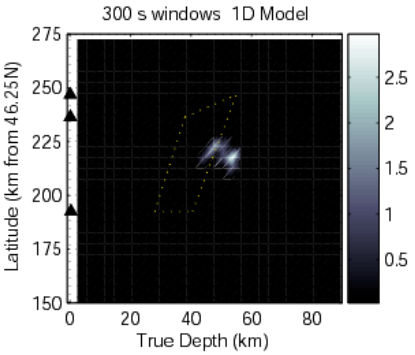
300 s windows 1D Model
Latitude (km from 46.25N)
True Depth (km)

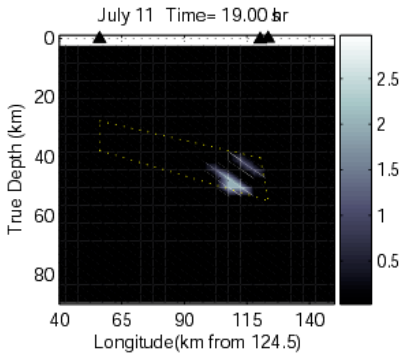
July 11 Time= 19.00 hr
True Depth (km)
Longitude(km from 124.5)

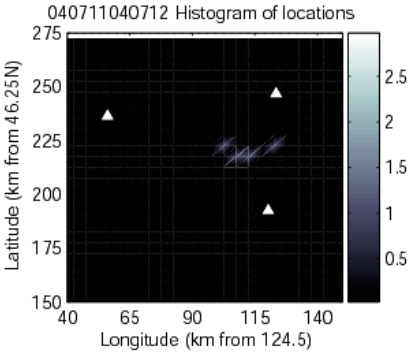
040711040712 Histogram of locations
Latitude (km from 46.25N)
Longitude (km from 124.5)
275
250
225
200
175
150
40
65
90
115
140
2.5
2
1.5
1
0.5

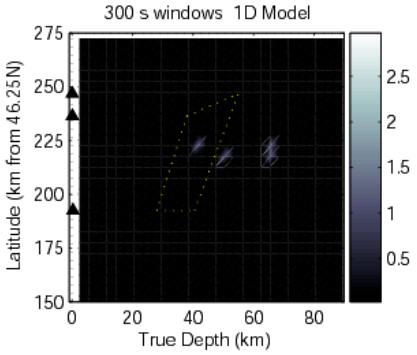
300 s windows 1D Model
Latitude (km from 46.25N)
True Depth (km)
275
250
225
200
175
150
0
20
40
60
80
2.5
2
1.5
1
0.5

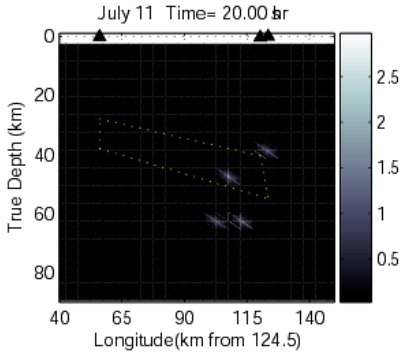
July 11 Time= 20.00 hr
True Depth (km)
Longitude(km from 124.5)
0
20
40
60
80
40
65
90
115
140
2.5
2
1.5
1
0.5

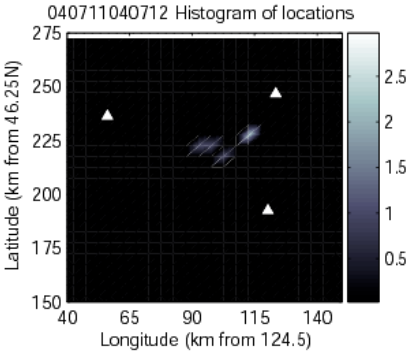
040711040712 Histogram of locations
Latitude (km from 46.25N)
Longitude (km from 124.5)
275
250
225
200
175
150
40
65
90
115
140
2.5
2
1.5
1
0.5

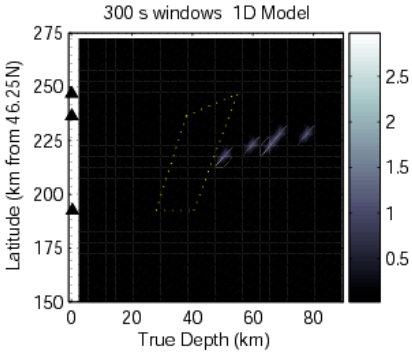
300 s windows 1D Model
Latitude (km from 46.25N)
True Depth (km)
275
250
225
200
175
150
0
20
40
60
80
2.5
2
1.5
1
0.5

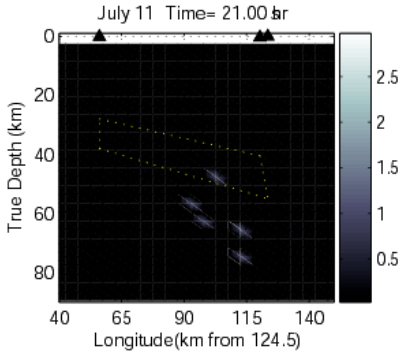
July 11 Time= 21.00 hr
True Depth (km)
Longitude(km from 124.5)
0
20
40
60
80
40
65
90
115
140
2.5
2
1.5
1
0.5

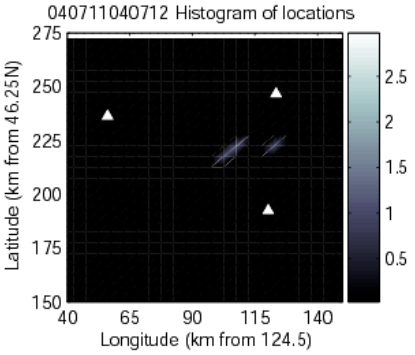
040711040712 Histogram of locations
Latitude (km from 46.25N)
Longitude (km from 124.5)

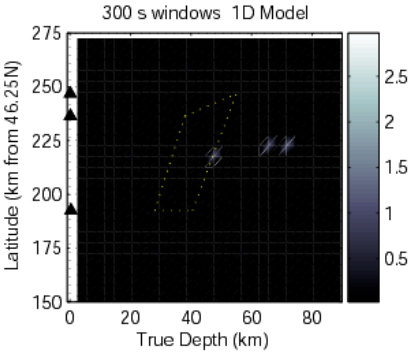
300 s windows 1D Model
Latitude (km from 46.25N)
True Depth (km)

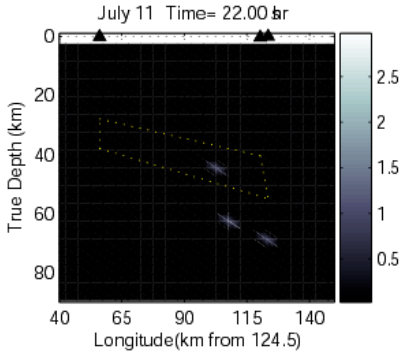
July 11 Time= 22.00 hr
True Depth (km)
Longitude(km from 124.5)

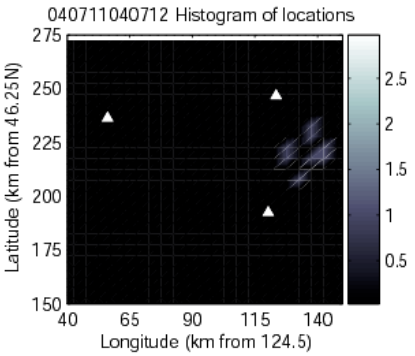
040711040712 Histogram of locations
Latitude (km from 46.25N)
Longitude (km from 124.5)

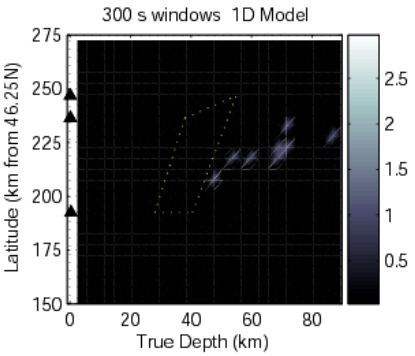
300 s windows 1D Model
Latitude (km from 46.25N)
True Depth (km)

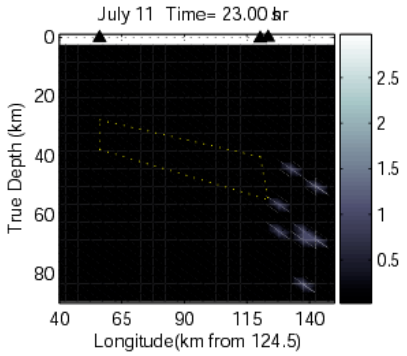
July 11 Time= 23.00 hr
True Depth (km)
Longitude(km from 124.5)

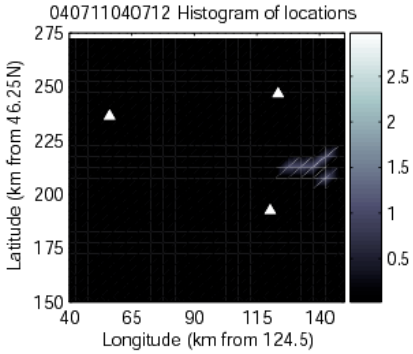
040711040712 Histogram of locations
Latitude (km from 46.25N)
Longitude (km from 124.5)

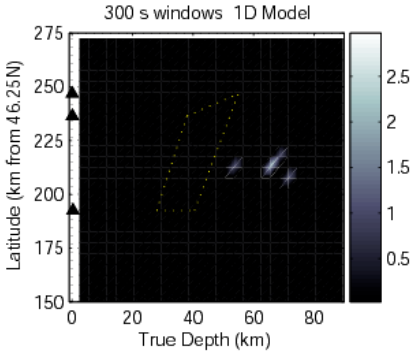
300 s windows 1D Model
Latitude (km from 46.25N)
True Depth (km)

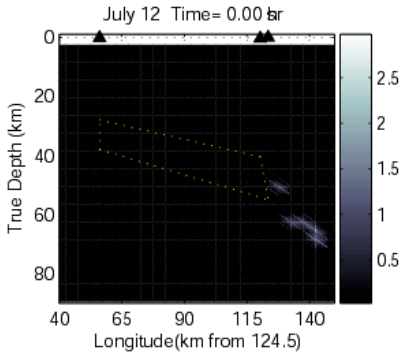
July 12 Time= 0.00 hr
True Depth (km)
Longitude(km from 124.5)

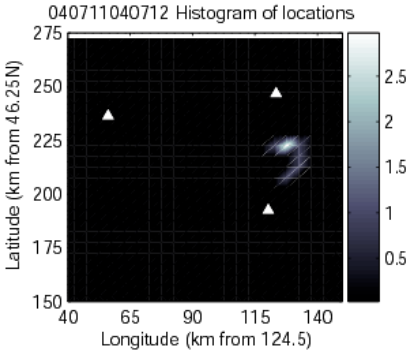
040711040712 Histogram of locations
Latitude (km from 46.25N)
Longitude (km from 124.5)

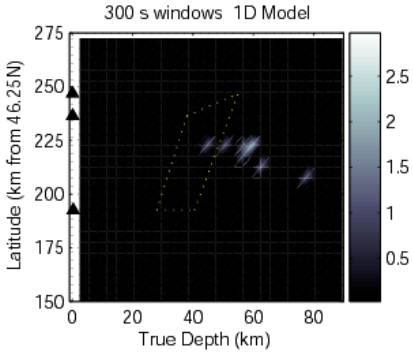
300 s windows 1D Model
Latitude (km from 46.25N)
True Depth (km)

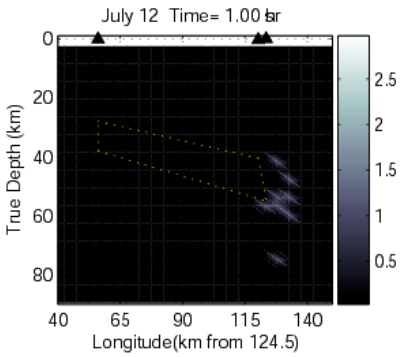
July 12 Time= 1.00 hr
True Depth (km)
Longitude(km from 124.5)

APPENDIX 4

Filmstrip of 30-s Locations July 11, 2004.Filmstrip representation of locations (misfit < 300) in successive 5-minute windows for the 30-second time window analysis between 21:00 and 22:00 hours on July 11, 2004. First column shows the locations in the X-Y plane, next column is the Z-Y plane, and the last column is the X-Z plane. The longitude axis (X) is kilometers measured from W124.5, and axis values range from 50 to 150 kilometers. The latitude axis (Y) is kilometers measured from N46.25, and axis values range from 150 to 275 kilometers. The depth axis (Z) is kilometers measured from sea level, and axis values range from 0 to 90 kilometers. Each frame represents the locations within a 5-minute time window. The figures show how the tremor locations migrate from one source region (between the three arrays) to another source region (east of Lopez and Sequim arrays). Figure can be compared to results in Appendix 3, where the five-minute time window data are plotted by hour. At that time scale the change in location is not obvious until between the hours 22:00 and 23:00.

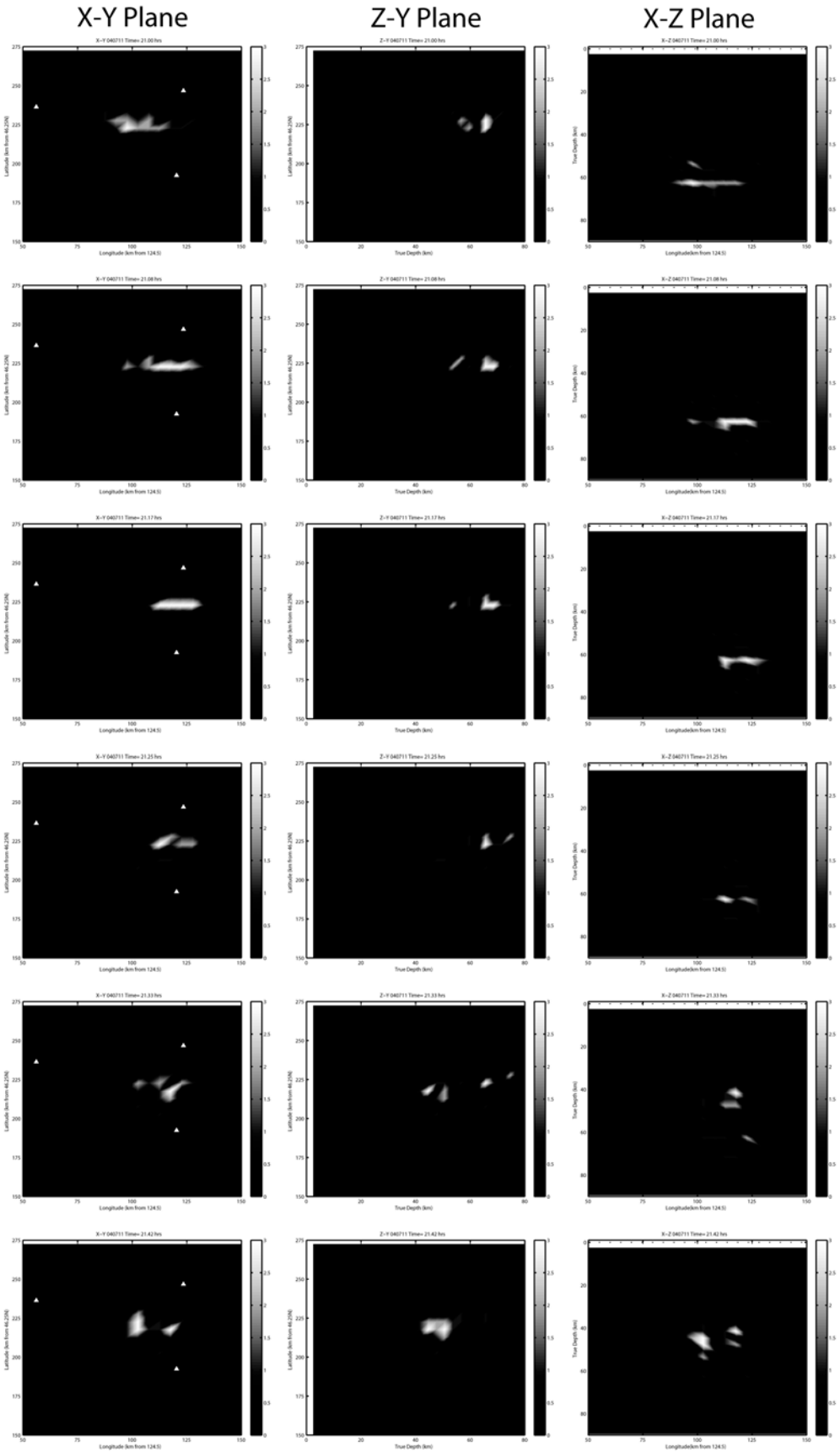
X-Y Plane
Z-Y Plane
X-Z Plane

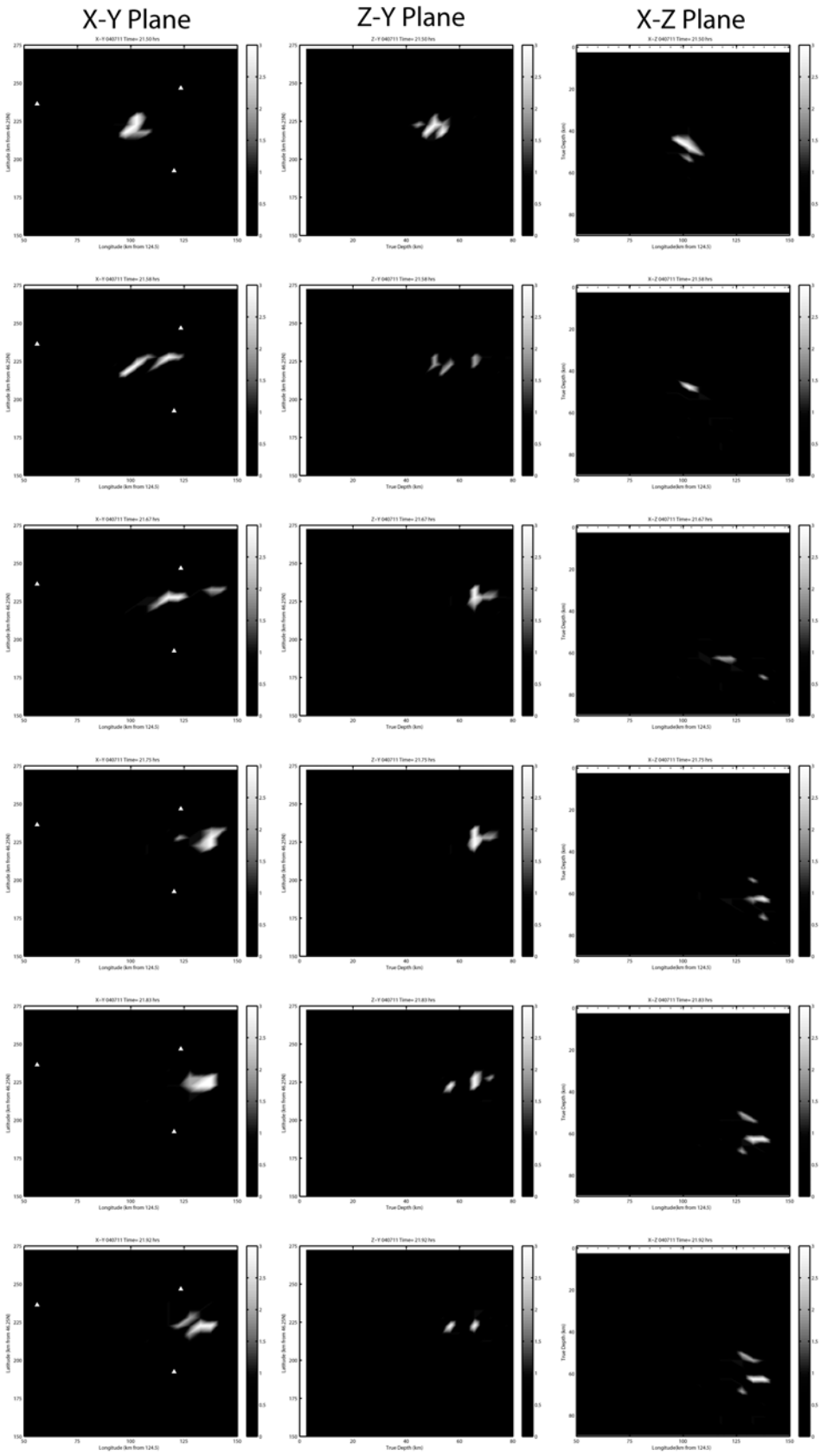
X-Y Plane
Z-Y Plane
X-Z Plane

VITA

Wendy McCausland was born in Buffalo, New York. She has lived in many places throughout the United States and the world. Currently she calls Seattle, Washington her home. At Carnegie Mellon University she earned a Bachelor of Science degree in Physics. She spent 11 months doing work with the Institute for International Cooperation and Development in La Estrella, Nicaragua. At Duke University she earned a Master of Science in Geology. In the summer of 2002 she spent a summer in Japan with the National Science Foundation's East Asia and Pacific Summer Institutes for U.S. Graduate Students. In 2006 she earned a Doctor of Philosophy at the University of Washington in Seismology.